MULTISTEP PROCESSES IN THE (d,t) AND (d, ^{3}He) REACTIONS ON ^{30}Si AND THE STRUCTURE OF MASS 29 NUCLEI

by

Robert Alexander Hilko

Department of Physics
Duke University

Date: 7 May 1974

Approved:

N. Russell Roberson, Supervisor

E. G. Bilpuch

Richard Smith

A dissertation submitted in partial fulfillment of the requirements for the degree of Doctor of Philosophy in the Department of Physics in the Graduate School of Arts and Sciences of Duke University

1974

ABSTRACT

(Physics)

MULTISTEP PROCESSES IN THE (d, t) AND (d, ^{3}He)

REACTIONS ON ^{30}Si AND THE STRUCTURE

OF MASS 29 NUCLEI

by

Robert Alexander Hilko

Department of Physics
Duke University

Date: _____

Approved:

_____
N. Russell Roberson, Supervisor

_____

_____

_____

_____

An abstract of a dissertation submitted in partial fulfillment of the requirements for the degree of Doctor of Philosophy in the Department of Physics in the Graduate School of Arts and Sciences of Duke University

1974

MULTISTEP PROCESSES IN THE (d,t) AND (d, ^{3}He) REACTIONS ON ^{30}Si AND THE STRUCTURE OF MASS 29 NUCLEI

by

Robert Alexander Hilko

Sixteen states with excitation energies < 6.2 MeV and the 8.34 MeV $5/2^{+}$ $t = 3/2$ state were studied in ^{29}Si. The first eight levels in ^{29}Al with excitation energies < 3.5 MeV were studied. The coupled-channel Born approximation (CCBA) was used to test two nuclear models, the rotational model with bandmixing and the shell model. The study of the inelastic effects in the scattering from the target nucleus was done for each level, but due to current limitations the study of the inelastic effects in the residual nucleus could only be done properly for the ground state rotational band of ^{29}Si. The need for multistep processes was found in the majority of levels.

With the use of the rotational model with bandmixing electromagnetic transition rates, lifetimes and branching ratios were determined. This calculation supported the CCBA results in favoring this model over the shell model. A complete calculation in a deformed Woods-Saxon potential was performed to determine energy levels and wave functions for various orbits. The results are very similar to the work of Nilsson who used a harmonic oscillator basis.

ACKNOWLEDGEMENTS

I wish to express my gratitude to my advisor, Dr. N. R. Roberson, for his interest, support and patience during my graduate career. I also wish to thank Dr. R. O. Nelson for his assistance in data collection and aid in the analysis. I also wish to thank Dr. C. R. Gould for his assistance in data collection. I wish to extend my appreciation to Dr. M. Divadeenam and to Dr. R. Y. Cusson for many helpful discussions.

My appreciation is extended to Dr. T. Tamura for many helpful conversations and correspondence. Also, I wish to extend my appreciation to Dr. T. Udagawa for several helpful conversations and correspondence. I wish to thank Dr. W. J. Thompson for his assistance in understanding several computer codes and reaction theory. I wish to thank S. Edwards. R. Rummel, M. Smith, and others for their assistance with the accelerator and electronic systems. I am grateful to Dr. H. W. Newson and Dr. E. G. Bilpuch for providing me with a research assistantship. Thanks to Al Rade for photographing the figures and to Ann Davis for typing this dissertation. Special thanks to D. Michele(Mike) Bailey for her preparation of figures and encouragement. I also wish to thank my parents for their support and encouragement.

This work was supported in part by the U. S. Atomic Energy Commission.

R. A. H.

CONTENTS

LIST OF FIGURES

LIST OF TABLES

MULTISTEP PROCESSES IN THE (d,t) AND (d,^{3}He) REACTIONS ON ^{30}Si AND THE STRUCTURE OF MASS 29 NUCLEI

Chapter I

INTRODUCTION

The collective model[1, 2] proposed to describe the nuclei between closed shells has enjoyed phenomenological successes. Nuclear levels have been interpreted as rotational bands in the 2s - 1d nuclei and more dramatically in heavy deformed nuclei. The collective model predicted the observed large enhancement of E2 gamma-ray transitions within a rotational band. The model has been most successful when the nucleus is prolate with fewer cases known for oblate nuclei. Within the 2s - 1d region the nuclei ^{29}Al and ^{29}Si have been the subject of much experimental[3-16] and theoretical work[17-22]. Studies of these nuclei by various transfer reactions and particle-gamma angular correlations have yielded energy spectra which can be reasonably described as rotational bands built upon deformed single particle states. The spectroscopic factors and gamma decay properties of low-lying states in these nuclei were in general agreement with the collective model.

The work of Beck et. al.[10] and Jones et. al.[3] has extended the knowledge of ^{29}Al to include lifetime measurements for low lying states. In Jones et. al. it was shown that the energy spectrum of ^{29}Al was consistent with a prolate shape. Unfortunately a bandmixing calculation (also known as rotational particle coupling) was not made even though reasonable occupation probabilities for the single particle bandheads were extracted. The results of Pilt et. al.[13] have recently identified several high spin states in ^{29}Si below 6.4

MeV. A bandmixing calculation was made with an oblate deformation which agreed with the structure of ^{29}Si. In addition, Wildenthal and McGrory [21] recently calculated using the modified surface delta interaction (MSDI) and Oak Ridge-Rochester shell model code energy spectra and single nucleon transfer strengths in the mass region 27-29. Gamma-ray transitions and lifetimes have also been calculated with the MSDI method by DeVoigt et. al. [20].

The ^{30}Si(d, ^{3}He) ^{29}Al and the ^{30}Si (d, t) ^{29}Si reactions were chosen for this study since the data on these nuclei could be accumulated simultaneously. The two nuclei are not mirrors but the ^{29}Al wave function can be tested in the ^{30}Si(d, t) ^{29}Si reaction for the 8.34 MeV state with t = 3/2. In both nuclei there are low-lying high spin states that exhibit anomalously large differential cross-sections. Also, angular distribution measurements have revealed large differences in the shapes between some of the established $\ell = 2$ transitions. An analysis by the distorted wave Born approximation (DWBA) has failed so far to predict these anamolies. These results suggested that a multistep process might be important in the particle transfer mechanism [23, 24, 25]. Such behavior may be enhanced due to the collective nature of this mass region. To include inelastic effects in the incident or exit channel the coupled-channel Born approximation (CCBA) of Penny and Satchler [26] coded by T. Tamura [27] was used to predict the particle angular distributions. The CCBA method needs the spectroscopic amplitudes for direct and indirect transfers. From nuclear model calculations this information can be procured and employed to predict angular distributions. More parts of the wave function can be tested in this way than just the direct part as in DWBA.

This work has yielded solid evidence for the importance of including strongly excited states in the incident channel and in the exit channel.

Chapter II

EXPERIMENTAL APPARATUS AND PROCEDURE

A. Ion Beams

The deuteron beams used for the differential cross-section measurements were extracted from the Triangle Universities Nuclear Laboratory Clyclo-Graaff accelerator and were analyzed with the 90^{o}- 90^{o} high resolution magnet system. The $^{30}Si(d,d)$, $^{30}Si(d,t)$, $^{30}Si(d,^{3}He)$, $^{28}Si(d,t)$, and $^{28}Si(d,^{3}He)$ reaction measurements were made with a beam energy of 23.0 MeV. The cyclotron produce 8 MeV D^{-} ions which were subsequently accelerated by a FN tandem to the required energy. Following the switching magnets, the beam was colliminated with adjustable vertical and horizontal slits. This was done to minimize the beam impinging on the chamber slits which causes slit scattering and degrades the energy spread of the beam on target. The current on the slits was monitored in the control room and kept at a minimum. The quality of the beam from the high resolution magnet system was excellent and improved the resolution of the energy spectra by about 25 per cent. There exists in an isochronous cyclotron the problem of extracting the final turn cleanly. By forcing very tight momentum constraints through the high resolution magnet system, the beam can be adjusted from the cyclotron to produce predominantly single turn extraction. It should be noted that the difference in energy of adjacent turns is about 38 keV.

Negative helium beams were obtained with the standard lithium exchange

source. A high energy beam was used for ^{3}He elastic and inelastic scattering by ^{29}Si. A low energy beam was used for target thickness determinations.

B. Target Chamber

Angular distributions were measured in a 60 cm chamber fabricated in the Duke and UNC instrument shops[28]. Inside the chamber are rotating plates having tracks for detector mounts. The tracks and mounts can be cooled by a Freon refrigeration system. Each rotating plate has an angular scale read by a vernier accurate to $\pm 0.05^{\circ}$. Five targets can be mounted in a target ladder that slides into the chamber through a vacuum lock. In this way the chamber can be let up to atmosphere quickly without damaging the targets that remain in the vacuum lock. It is also possible to remove the target ladder leaving the chamber evacuated. Beam collimination was adjusted so that vertical slits were 0.16 in. and the horizontal slits 0.12 in.

The beam current was collected and integrated in an electrically insulated Faraday cup that was located four meters behind the chamber. The insulating delrin rings were lightly sanded and cleaned with distilled water followed by medical grade alcohol. These precautions are very necessary to insure low leakage and accurate charge integration.

C. Targets

The ^{28}Si, ^{29}Si, and ^{30}Si targets were prepared from enriched isotope purchased from the Isotopes Division of the Oak Ridge National Laboratory. The targets were self-supporting silicon monoxide films. The method for making these targets is explained in detail in Appendix A. The enrichments

for the ^{28}Si, ^{29}Si, and ^{30}Si were 99.38%, 92.0%, and 95.55% respectively. The thicknesses of the targets were determined by assuming the forward angle measurements for both 4.5 MeV alpha beams or 2.8 MeV proton beams were purely Rutherford. The measured thicknesses for the above targets were respectively 131.0, 22.4, and 94.1 $\mu g/cm^2$.

D. Particle Detectors

The charged particles were detected by silicon surface barrier detectors. Except for target thickness determinations with the low energy beams, a method of particle identification was used throughout. A counter telescope consists of a thin totally depleted detector that measures the energy loss but not the total energy of the particle. The next component is a thick totally depleted detector that stops the most energetic particles of interest. The thin detector is noted as ΔE, and the thick second detector as E. The selected E detectors varied in thickness from 1000 μm to 2000 μm. In selecting ΔE detectors, the experiment dictates the optimum thickness. For an experiment where tritons and ^3He are measured simultaneously they must be thick enough for a reasonable signal from the tritons passing through, yet thin enough not to stop the ^3He particles. In this experiment, the ΔE detectors ranged from 38.6 μm to 61.7 μm in thickness for the four telescopes used, with the thickest at the most forward angles. In the elastic and inelastic scattering experiments the ΔE detectors were changed to ones whose thicknesses varied from 200 μm to 400 μm. For the (d,t), (d,He), and (d,d) experiments the counter telescopes were Freon cooled to reduce the thermal noise of the electrons in the silicon detectors and thereby improve the energy

resolution. In the ^{3}He scattering experiments, three uncooled counter telescopes were employed with $17\mu_m$ to $23\mu_m$ thick ΔE detectors and $300\mu_m$ E detectors.

E. Electronics

The block diagram of the electronic apparatus is shown in fig. 1. Each counter telescope has the configuration shown in part (a) of this figure. Signals from the two totally depleted transmission type detectors pass through charge sensitive preamplifiers and through separate linear amplifiers. The prompt bipolar outputs from the linear amplifier triggers a timing single channel analyzer which produced a gate pulse for a slow coincidence with the linear gated stretcher. Also, a routing pulse was generated by the output of the TSCA to denote which telescipe produced the ΔE_N and $E_N + \Delta E_N$ signals. Since the ΔE signals are, in general rather small, the gain of each ΔE amplifier had to be boosted in order to trigger reliably the timing single channel analyzers (TSCA).

Fig. 1 (b) shows how the ΔE, E and routing signals were processed. Since the ΔE signals had more gain, an attenuator was placed after the ΔE summing circuits to match the gain of the E summing circuit. These two linear signals were added to yield the full-energy $E + \Delta E$ pulses.

The ΔE and full energy signals are then sent to an analog to digital converter (ADC). The routing pulses are each processed by a router which generated a gate to enable the ADC's to digitize the proper pair of signals. A digitized event consisting of the energy loss ΔE signal (10 bits), full energy

Figure 1. Block diagram of the particle identification electronic set up. Part (a) indicates electronic apparatus for each counter telescope. For every coincident event energy pulses ΔE_n and E_n, with a routing pulse, R_n are sent to a summing circuit (b). This circuit forms a ΔE_n and E_n sum and stores in the computer a binary number representing an event. An event consists of a E, $\Delta E + E$ and R information which the computer is programmed to identify and store. The monitor system is also shown at the bottom.

(a)

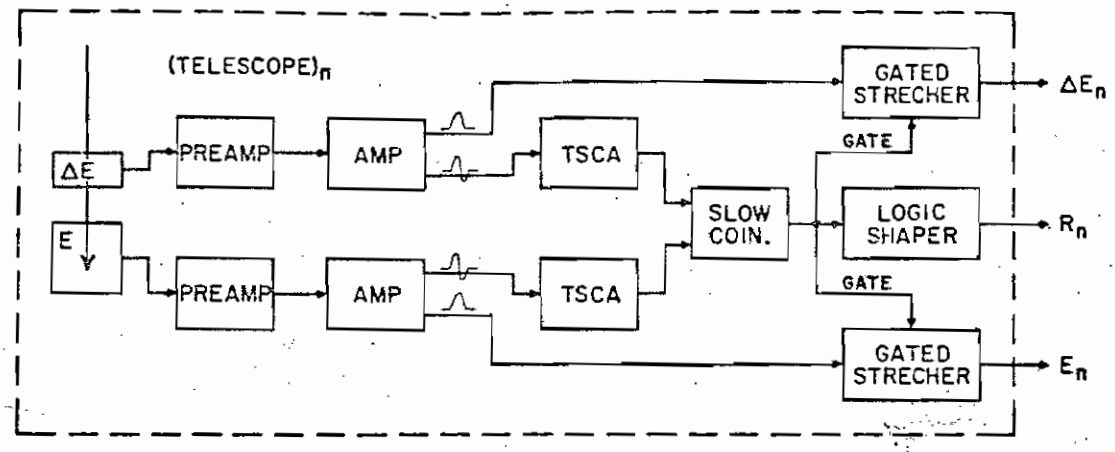
(TELESCOPE)n
ΔE
E
PREAMP
PREAMP
AMP
AMP
TSCA
TSCA
SLOW COIN.
GATED STRECHER
GATE
LOGIC SHAPER
GATE
GATED STRECHER
ΔEn
Rn
En

(b)

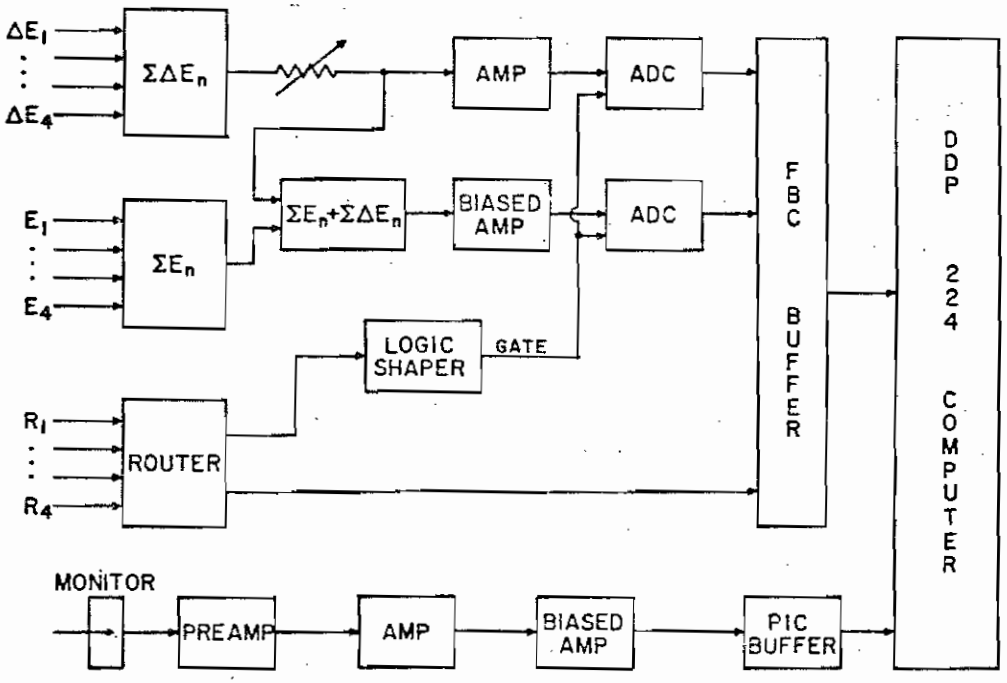
ΔE1
ΔE4
ΣΔEn
AMP
ADC
E1
E4
ΣEn
ΣEn+ΣΔEn
BIASED AMP
ADC
LOGIC SHAPER
GATE
R1
R4
ROUTER
FBC BUFFER
DDP 224 COMPUTER
MONITOR
PREAMP
AMP
BIASED AMP
PIC BUFFER

(E + ΔE), signal (12 bits) and telescope number (R) (2 bits) is transferred into a 24 bit buffer that inserts it into the computer through the interface. A fully buffered channel (FBC) is used to collect many events before the analysis of them begins. A particle identification program [23, 29] for the on-line computer (DDP-224) takes this buffered information and stores singles spectra from either ADC, mass identification spectra, or energy spectra of selected mass groups. Buffered tape storage [23] was used since complete energy spectra could not be simultaneously stored in the memory of the computer with as great a dispersion as needed. The experiment is analyzed at a later time by reaccumulating complete energy spectra from the events stored on magnetic tape with an off-line computer program. Events of interest were stored on magnetic tape with the original digital conversion. On-line display was limited to 512 channel for each mass group. Four telescopes each accumulating triton and ^{3}He spectra necessitated this method due to limited storage capability.

F. Procedure

1. General

The targets and detectors were placed in the scattering chamber and the chamber was evacuated to about 5×10^{-5} mm of Hg. The Freon refrigerator was then started to cool the detectors. When cooled, the detectors were biased and leakage current checked to make sure that the current is less than when the detector is warm.

Once cooled, the final testing of each telescope begins with a pulser test system which sends a test pulse to the ΔE and E preamplifiers. The timing

single channel analyzer's were adjusted to minimize time jitter for different input amplitudes. The delays were set to produce a $\Delta E - E$ coincidence. Since d - c coupling is used, it is imperative that the d - c levels be zero, otherwise a voltage level will interfere with the other telescopes when the sums are produced. In the pulse stretchers the gate period initiated by the coincidence signal was set at $2\mu s$ and was checked to verify that it preceded the peak of the linear input. The width and delay of the stretchers were adjusted to produce a $\Delta E - E$ overlap.

With the beam on target, the pole-zero adjustments on each amplifier is made, and coincident timing is rechecked. The sum of ΔE and E signals are checked for any needed adjustments of delay or pulse width. It is possible to make preliminary pole-zero adjustments with a pulser, but it is best to readjust it with the actual random events.

A counter telescope requires that the ΔE and E signal amplification systems have matched gains. A gain mismatch will yield degraded mass identified spectrum[30]. A test pulse was applied to each preamplifier with the same charge terminator. The gain of each linear amplifier was adjusted to store the test pulse in the same channel through the $E + \Delta E$ spectrum. This feature eliminates the need of matching E and ΔE amplifiers through different ADC's. The biased amplifier for the total energy signal was adjusted to select the energy range of interest. The biased amplifier and ADC for the ΔE signals were adjusted to give ΔE spectrum of equal gain and zero intercept. Before the mass spectra are accumulated the $E + \Delta E$ intercept is measured and entered into the computer by typewriter command. Gain matching is done

with no beam on target.

Mass spectra can now be accumulated and a typical spectrum is shown in fig. 2. Mass windows can be set for the mass groups to be displayed, and mass reject windows for the raw data events not to be stored on on-line magnetic tape storage. The energy spectra stored on-line were written on magnetic tape for later off-line analysis.

The beam was integrated by an electronic current integrator and indicator which generated a pulse for each unit of charge. These pulses were counted with three scalers. One scaler was gated off when the FBC was busy, another when the parallel input channel was busy (used for the monitor counter), and another not gated to record live charge. A spectra could be corrected for dead time counting losses with the appropriate ratios of scaler counts. If dead time losses were high enough a check of this method was made by sending a pulser signal into a telescope and counting the number stored in a spectrum to the number recorded with an ungated scaler. The pulser method was used for the 15° points as an added check. Dead time losses were usually reduced by limiting the beam intensity to an acceptable value. The scalers were read into the computer at the end of a run and recorded on the on-line typewriter and magnetic tape.

2. $^{30}Si(d,t)$ ^{29}Si and $^{30}Si(d,{}^{3}He)$ ^{29}Al Spectra

The differential cross-sections for the $^{30}Si(d,t)$ and $^{30}Si(d,{}^{3}He)$ reactions were measured in 5° increments for angles from 15° to 95° relative to the beam direction. A ^{30}Si target was selected that was thick enough to produce a suitable yield while not too thick to degrade the needed resolution

Figure 2. Typical mass spectrum taken with an enriched ^{28}Si 0 target.

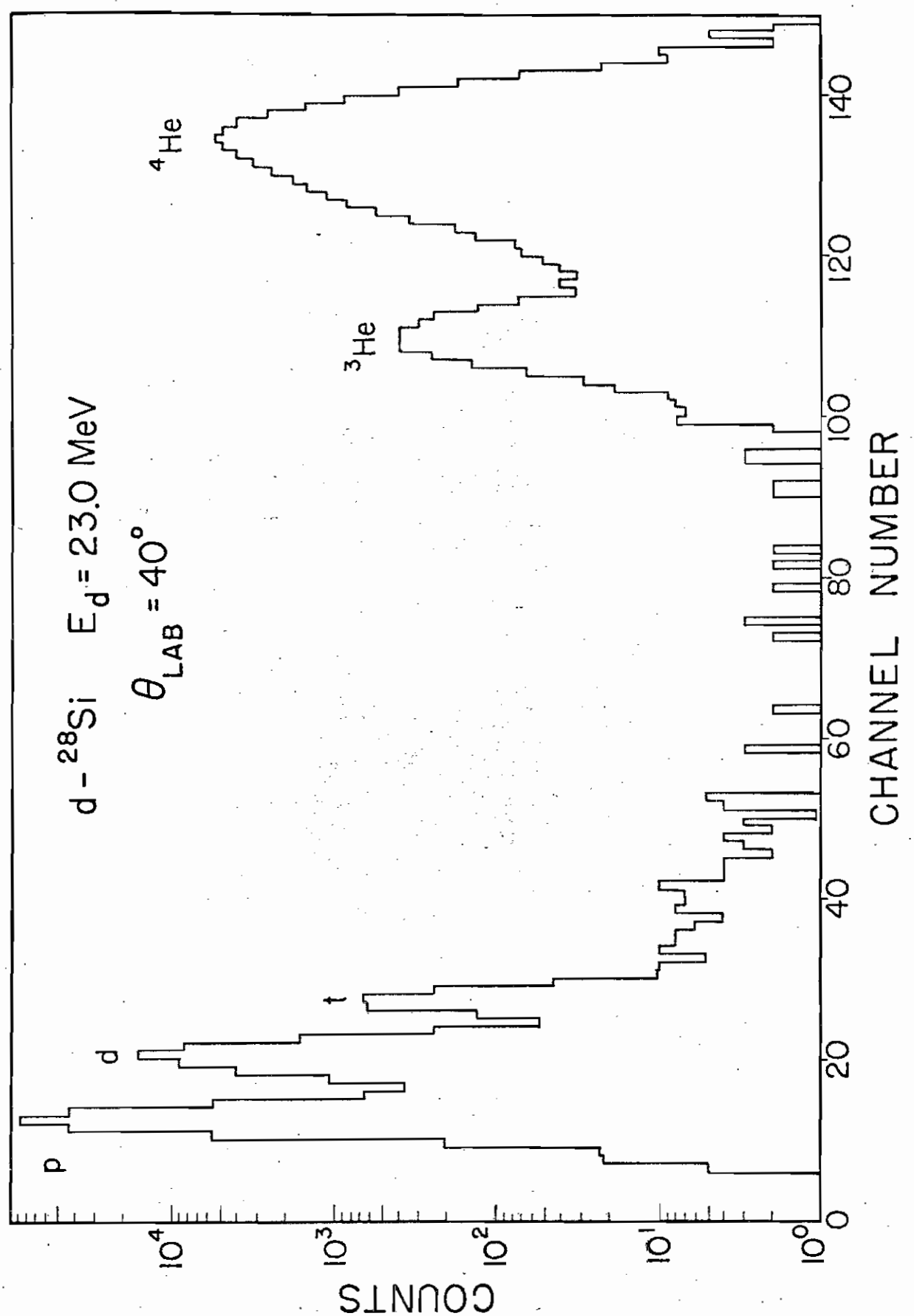
d - 28Si E_d = 23.0 MeV
θ_LAB = 40°
p
d
t
3He
4He
COUNTS
CHANNEL NUMBER
10^0
10^1
10^2
10^3
10^4
0
20
40
60
80
100
120
140

for the ^{3}He spectra. The four counter telescopes were arranged twenty degrees apart. The first two subtended a solid angle of 0.257×10^{-3} steradians each, and the next two 0.489×10^{-3} steradians. This was done to minimize count rate differences between the four telescopes. Spectra for the $^{30}Si(d,t)\,^{29}Si$ and $^{30}Si(d,\,^{3}He)\,^{29}Al$ reactions are illustrated in figures 2 and 3. The overall resolution for the triton spectra varied from 33 to 50 keV, and for the ^{3}He spectra the resolution varied from 55 to 90 keV. The $^{30}Si(d,t)\,^{29}Si$ spectrum does not have many contaminants obscuring the states in ^{29}Si due to the high Q-value of the reaction as compared to those of ^{12}C and ^{16}O. Unfortunately, this was not the case for the $^{30}Si(d,\,^{3}He)^{29}Al$ spectra as in illustrated in fig. 4. The $^{28}Si(d,\,^{3}He)\,^{27}Al$ contaminant happens to have a few strong peaks that are very near and cross under weakly populated peaks in ^{29}Al. This could have been unfruitful, but similar data with an enriched ^{28}Si target was measured with the same detector arrangements and electronic apparatus. The ^{28}Si target chosen was approximately the same thickness, and the energy resolution was very close to the $^{30}Si(d,\,^{3}He)^{29}Al$ spectrum. A program[31] which is designed to subtract contaminants from one spectrum by comparing to another was used. The program subtracted a spectrum of the same energy scale except for minor energy shifts. Strong, easily identified peaks were used as references. In this study states from the $^{16}O(d,\,^{3}He)\,^{15}N$ and $^{12}C(d,\,^{3}He)^{11}B$ reactions served as the reference peaks usually, by which the spectra could be aligned for subtraction. Subtraction was done in increments, till the states in ^{27}Al(0.00 MeV, 0.843 MeV, and 1.013 MeV) were reduced to a background level as in the bottom spectrum

Figure 3. Sample energy spectrum for the $^{30}Si(d,t)^{29}Si$ reaction. Peaks are identified by excitation values (MeV). Contaminants are identified by isotope and excitation energy.

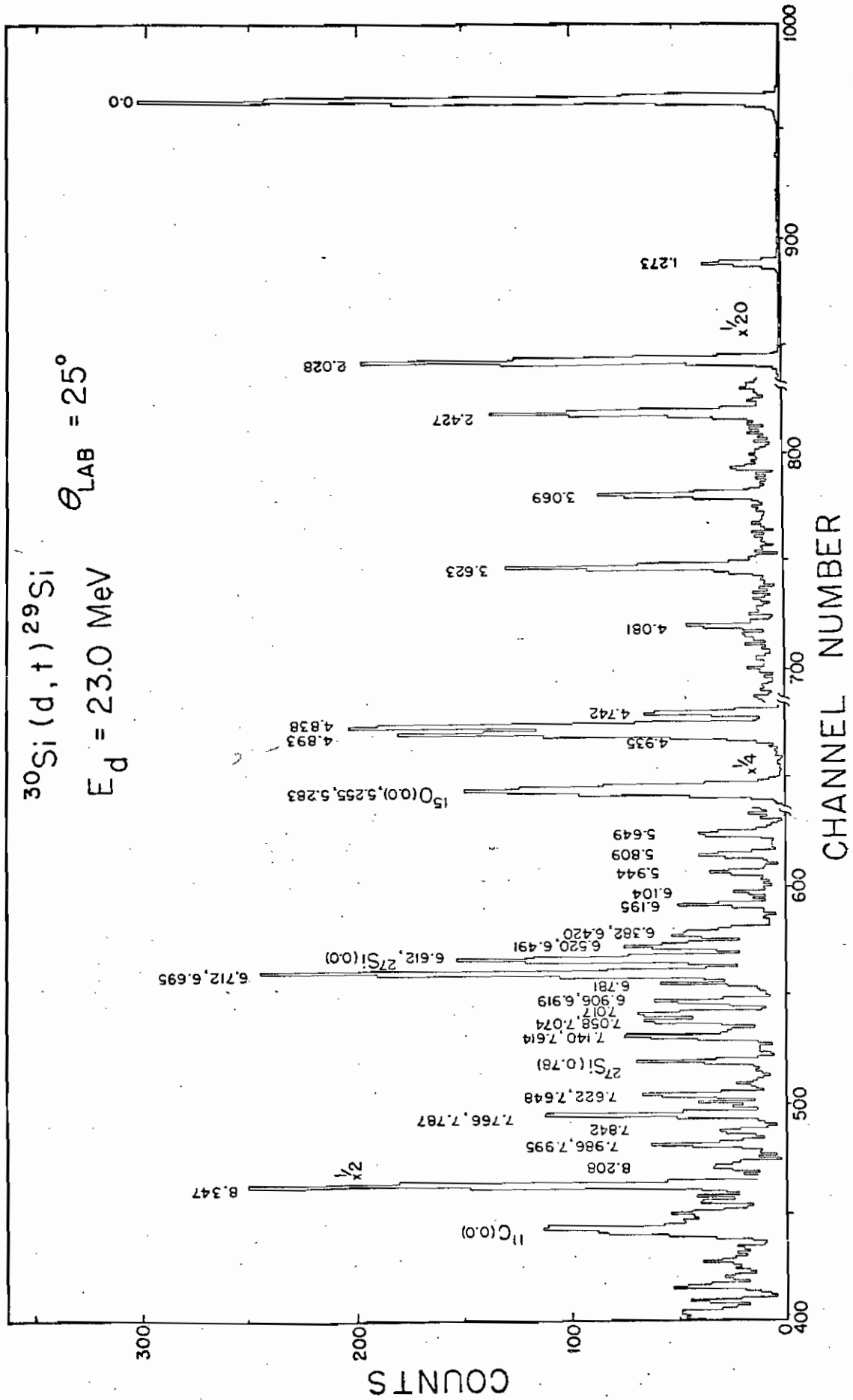
^{30}Si (d, t) ^{29}Si
E_d = 23.0 MeV
θ_{LAB} = 25°
COUNTS
CHANNEL NUMBER
0
100
200
300
400
500
600
700
800
900
1000
0.0
1.273
1/20 x
2.028
2.427
3.069
3.623
4.081
4.742
4.838
4.893
4.935
1/4 x
^{15}O(0.0), 5.255, 5.283
5.649
5.809
5.944
6.104
6.195
6.382, 6.420
6.520, 6.491
6.612, ^{27}Si(0.0)
6.712, 6.695
6.781
6.906, 6.919
7.017
7.058, 7.074
7.140, 7.614
^{27}Si(0.78)
7.622, 7.648
7.766, 7.787
7.842
7.986, 7.995
8.208
1/2 x
8.347
^{11}C(0.0)

Figure 4. Sample energy spectra for the $^{30}Si(d, ^{3}He)\ ^{29}Al$ reaction. Peaks are identified by excitation value (MeV) and contaminants isotope. Below the normally collected spectrum is the resulting subtracted spectrum where the $^{29}Si(d, ^{3}He)^{27}Al$ contaminants have been subtracted. Note the improvement for the weak 3.19 and 2.73 MeV levels in ^{29}Al.

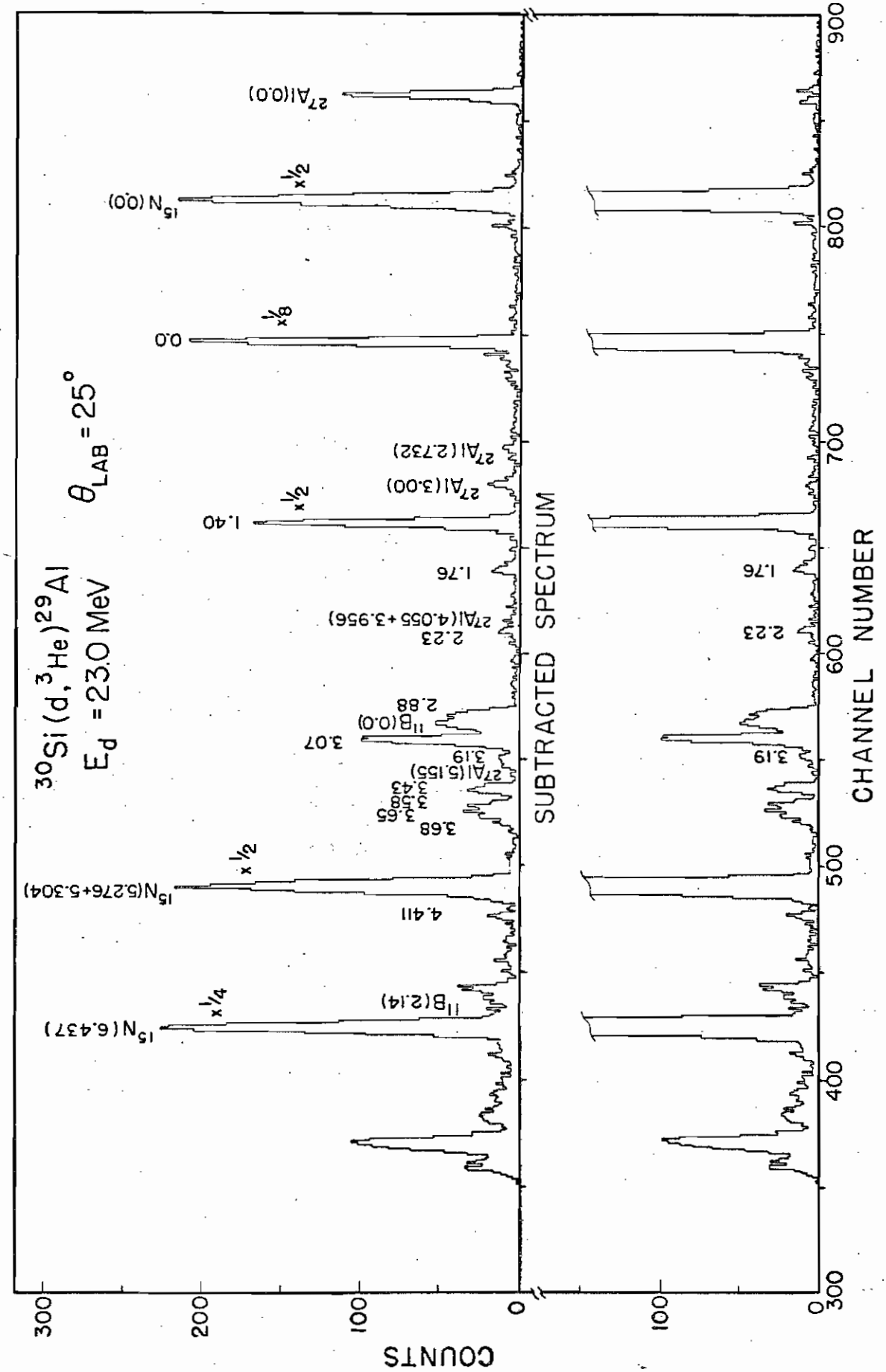
$^{30}Si(d,^3He)^{29}Al$
E_d = 23.0 MeV
θ_{LAB} = 25°
COUNTS
CHANNEL NUMBER
SUBTRACTED SPECTRUM
^{15}N(6.437)
^{11}B(2.14)
4.41
^{15}N(5.276+5.304)
3.68
3.65
3.59
3.43
^{27}Al(5.155)
3.19
3.07
^{11}B(0.0)
2.88
^{27}Al(4.055+3.956)
2.23
1.76
1.40
^{27}Al(3.00)
^{27}Al(2.732)
0.0
^{15}N(0.0)
^{27}Al(0.0)
1/4
1/2
1/2
1/8
1/2

of fig. 3. Subtracted spectra were analyzed for the states which were interfered with and the errors were doubled to take into account the uncertainties. The angular distributions for the 2.23 MeV and 3.19 MeV levels in ^{29}Al were obtained this way.

3. ^{30}Si(d, d) and ^{30}Si(d, d') spectra

Elastic and inelastic scattering cross-sections were measured for 23.0 MeV deuterons incident on ^{30}Si at laboratory angles from 20° to 160° in steps of five degrees. Angular distributions for the ground-state and first excited 2^+ state were measured. Fig. 5 illustrates a typical spectrum; the energy resolution of the inelastic data was 30 keV which is very good for counter telescopes. The 2.23 MeV excited state exhibits a cross-section that is strong but does not dominate over the ground-state.

4. ^{29}Si(^{3}He, ^{3}He) and ^{29}Si(^{3}He, ^{3}He') spectra

Elastic and inelastic ^{3}He scattering cross-sections were measured at 19.0 and 15.0 MeV with ^{29}Si target that was an enriched isotope deposited on a 20 μg/cm^2 carbon backing. The data in the laboratory was taken from 25° to 140° in five degree steps at both energies. These energies were chosen to correspond to the outgoing triton or ^{3}He energies of the ^{30}Si(d, t) and ^{30}Si(d, ^{3}He) reactions, in order that optical model parameters could be determined for the exit channels. Inelastic angular distributions for the 19.0 MeV beam energy were measured for the exited states in ^{29}Si at 1.273, 2.028, and 2.426 MeV respectively. This was done to extract a coupling scheme in the exit channel to be used by the coupled-channel methods. Each telescope

Figure 5. $^{30}Si(d, d')^{30}Si$ energy spectrum for scattering of 23.0 MeV deuterons at $\theta_{Lab} = 55^{o}$. Peaks are identified by excitation energy (MeV). Note that the energy resolution is very good and is about 30 keV. The first 4^{+} state at 5.274 MeV is weak. The dominant peaks are the groundstate and first excited state (2^{+}) at 2.23 MeV.

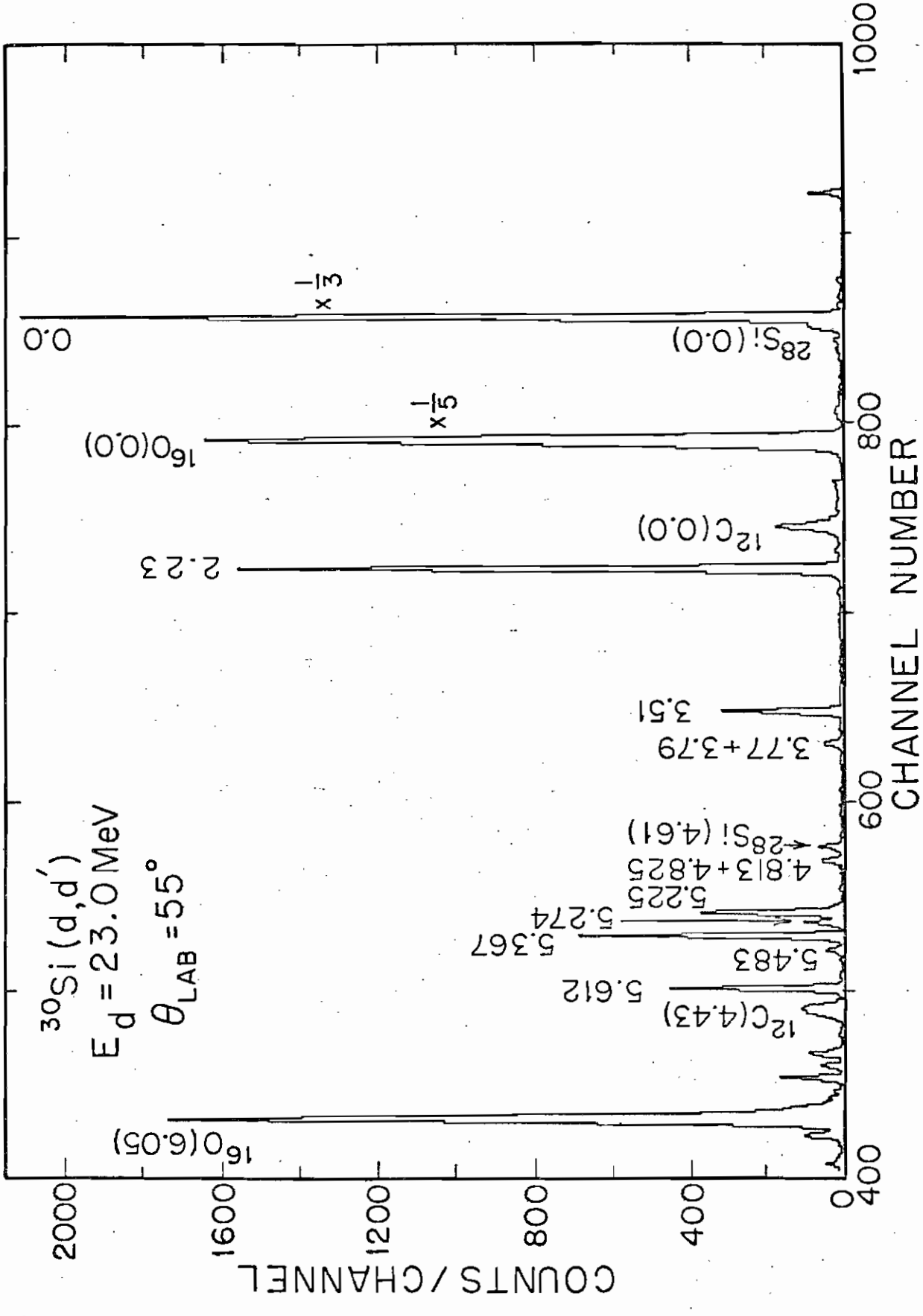
$^{30}Si\,(d,d')$
$E_d = 23.0$ MeV
$\theta_{LAB} = 55°$
COUNTS / CHANNEL
CHANNEL NUMBER
0
400
800
1200
1600
2000
400
600
800
1000
$^{16}O(6.05)$
$^{12}C(4.43)$
5.612
5.483
5.367
5.274
5.225
4.813 + 4.825
$^{28}Si\,(4.61)$
3.77 + 3.79
3.51
2.23
$^{12}C(0.0)$
$^{16}O(0.0)$
$\times\frac{1}{5}$
$^{28}Si\,(0.0)$
$\times\frac{1}{3}$
0.0

subtended a solid angle of 0.32×10^{-3} steradians. Only the ground state was measured for the 15.0 MeV spectra. The spectrum in fig. 6 shows an energy spectrum obtained at 19.0 MeV beam energy.

Figure 6. Sample energy spectrum for $^{29}Si(\,^{3}He, ^{3}He')^{29}Si$ reactions. The dominant peaks are the ground state and the 2.028 MeV state. Peaks are identified by excitation energy (MeV).

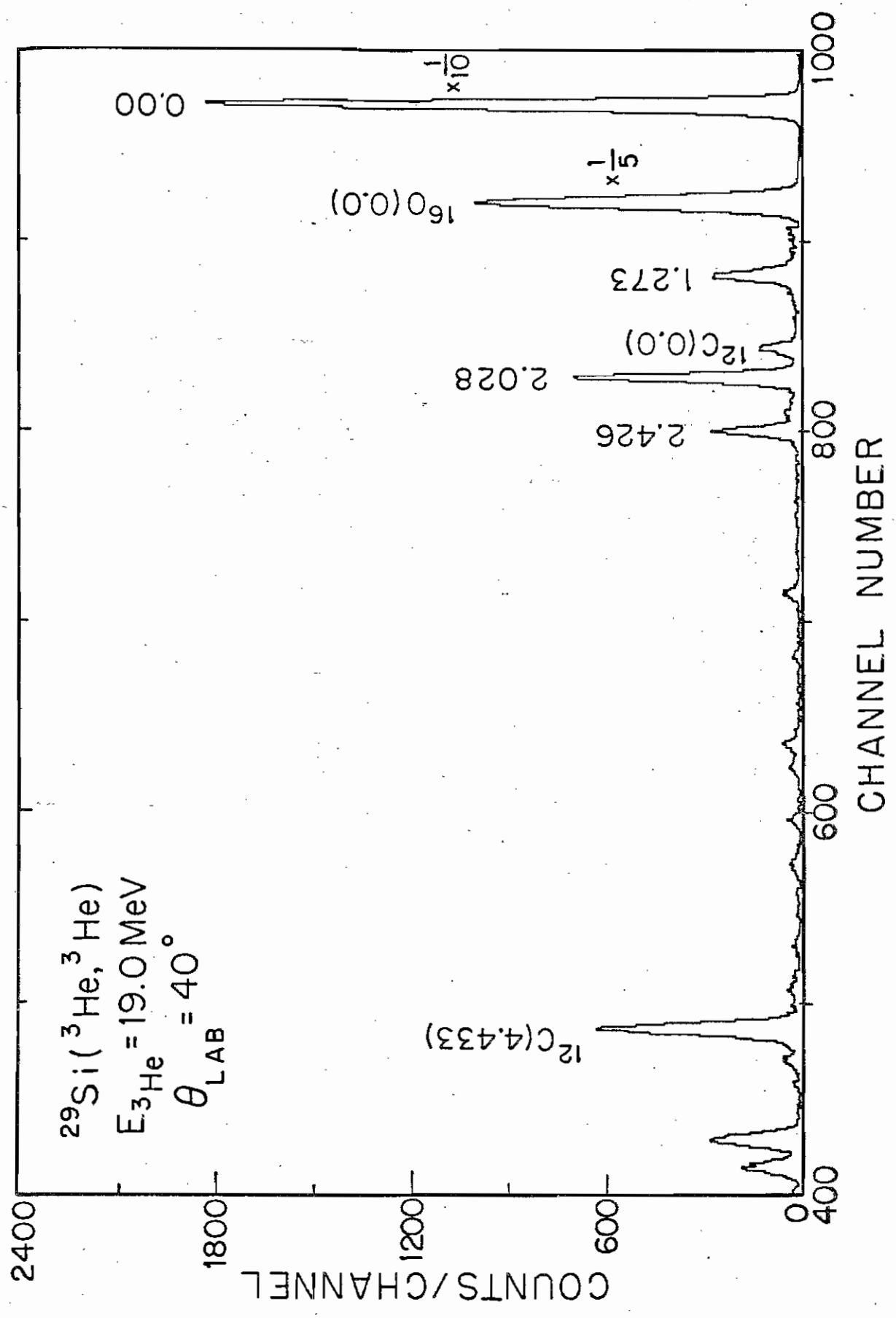
$^{29}Si(^3He,^3He)$
$E_{^3He} = 19.0$ MeV
$\theta_{LAB} = 40°$
$^{12}C(4.433)$
$^{12}C(0.0)$
2.028
2.426
1.273
$^{16}O(0.0)$
0.00
$\times\frac{1}{10}$
$\times\frac{1}{5}$
COUNTS/CHANNEL
CHANNEL NUMBER
0
400
600
800
1000
600
1200
1800
2400

Chapter III

COUPLED-CHANNEL CALCULATIONS

A. Coupled-Channel Optical Model

1. Optical Model

The optical model is a successful approximation for describing the elastic scattering of nuclear particles on a target nucleus. In the usual form, the optical model potential is split into a real and an imaginary part, with a Woods-Saxon form factor to describe the nuclear density of the target nuclear and is given by

$$U(r) = -V\, f(r, r_o, a_o) - i W f(r, r_w, a_w)$$

$$+ 4 i a_d W_d \frac{d}{dr_d} f(r, r_d, a_d) + V_{so} \frac{\vec{\ell}\cdot\vec{s}}{r_{so}} \frac{d}{dr_{so}} f(r, r_{so}, a_{so}) + V_c \quad (1)$$

where

$$V_c = (z Z e^2 / 2 R_c)\,[3 - (r/R_c)^2] \quad \text{for} \quad r \leq R_c$$

$$= (z Z e^2 / r) \quad \text{for} \quad r \geq R_c \quad \text{with} \quad R_c = r_c A^{1/3}$$

and

$$f(r, r_o, a_o) = (1 + \exp((r - r_o A^{1/3})/a))^{-1} \quad (2)$$

The parameters of the potential are V the real volume strength, W the imaginary volume strength, W_d the imaginary surface strength, V_{so} the spin-orbit strength and the Woods-Saxon form factor geometrical parameters. While this form has many parameters, the need for the potential to represent

the nucleus restricts the range of values that are acceptable. The potential is a simple one body force. The time-reversed-phase convention is normally used since it is easier in this manner to compute the scattered wave functions which are a sum of incoming and outgoing waves.

The imaginary potential is used to describe the absorption of flux from the incident beam into non-elastic channels. This approximation is quite good if a statistical approach can be applied. In such a case no one reaction channel is dominant, but a myriad of channels each take a small amount of flux. If there exists a single channel that is strong enough to account for a sizable component of the imaginary strength, a parameter can have values which are outside the acceptable physical range. Such a result is seen in deformed nuclei where the inelastic scattering to the first excited state is strong.

2. Coupled-Channel Optical Model

A next approximation to understanding the elastic scattering is to take into account the deformation of the nuclear surface. Within the framework of the collective model, the target nucleus can be described by expanding the radius in terms of spherical harmonics as

$$R = r_o A^{1/3} (1 + \sum_{\lambda\mu} \alpha_{\lambda\mu} Y_{\lambda\mu} (\theta, \phi)). \qquad (3)$$

An explanation of the effect of the first few terms is given by Rowe.[32] The $\lambda = 0$ term contributes a renormalization to the spherical field since Y_{oo} is a constant. The $\lambda = 1$ term yields a center of mass displacement

which yields no vibrations. The $\lambda = 2$, the quadrupole term, is the first to contribute a symmetric addition that corresponds to a vibration or possibly a rotation. For vibrational nuclei the potential was expanded in $\sum_{\lambda\mu} \alpha_{\lambda\mu} Y_{\lambda\mu}$ and for rotational nuclei that were axially symmetric in $\sum_{\lambda} \beta_{\lambda} Y_{\lambda}$. For this latter case, the expansion leads to a Legendre polynomial expansion. This discussion follows the work of T. T. Tamura.[33, 34]

The wave function of the projectile and target are written as

$$\Psi = r^{-1} \sum_{J_n \ell_n j_n} R_{J_n \ell_n j_n}(r) \left(Y_{\ell_n j_n} \otimes \Phi_{I_n} \right)_{JM}$$

$$= r^{-1} \sum_{J_n \ell_n j_n m_j M_n m_{\ell_n} m_s} R_{J_n \ell_n j_n}(r) (j_n I_n m_j M_n | JM)$$

$$x (\ell_n s m_{\ell_n} m_s | j_n m_j) i^{\ell} Y_{\ell_n m_{\ell_n}}(\theta, \phi) X_{s m_s}(\sigma) \Phi_{I_n M_n}(\xi) \quad (4)$$

The $(ABab|Cc)$ are Clebsch-Gordon coefficients for the coupling of two angular momenta $\vec{A}$, $\vec{B}$ to a third $\vec{C}$. Here $\Phi_{I_n M_n}(\xi)$ represents the Nth excited state of the target, $X_{s m_s}$ is the projectile spin wave function, $Y_{\ell_n m_{\ell_n}}$ is the angular momentum part of the projectile, and $R_{J_n \ell_n j_n}(r)$ describes the relative motion between the projectile and target. The angular momentum of the total system Ψ is $\vec{J}$. The Hamiltonian can be separated into the internal motion of the target, H_n; the kinetic energy of the projectile K_p; and interaction between the projectile and target, U as

$$H = H_n + H_p + U \quad (5)$$

with

$$H_n \Phi_{I_n}(\xi) = \epsilon_n \Phi_{I_n}(\xi) \qquad (6)$$

where the energies ϵ_n correspond to the excited states of the target nucleus. In the simple optical model the potential was a function of the projectile spin and distance from a central potential, and not of the target co-ordinates, ξ. The potential U (see sect. A. 1) was diagonal with respect to the set of wave-function $(\psi_{l_n j_n} \otimes \Phi_{I_n})_{JM}$. The potential used in the coupled-channel method has the form of the spherical optical model potential given in equation (1), except that once the expansion is made the diagonal and the coupled part separate as follows

$$V(r, \theta, \phi) = V_{diag}(r) + V_{couple}(r, \theta, \phi) \qquad (7)$$

where

$$V_{couple} = \sum_{\lambda\mu(\lambda\neq 0)} \mathcal{V}_{cp}^{(\lambda)}(r) D^{\lambda}_{\mu o} Y_{\lambda\mu}(\theta, \phi) \qquad (8)$$

and V_{diag} is given by eq. (1).

For a rotational axially symmetric nucleus the coefficients of the V_{couple} expansion become

$$\mathcal{V}_{cp}^{(\lambda)}(r) = 4\pi \int_0^1 \left\{ -V\left(1+\exp\left(\left(r - r_o A^{1/3}\left(1+\sum_{\lambda'} \beta_{\lambda'} Y_{\lambda' o}\right)\right)/a\right)\right)^{-1} \right.$$

$$- i W\left(1+\exp\left(\left(r - r_w A^{1/3}\left(1+\sum_{\lambda'} \beta_{\lambda'} Y_{\lambda' o}\right)\right)/a_w\right)\right)^{-1}$$

$$\left. -4 i W_d \frac{\exp\left(\left(r - r_d A^{1/3}\left(1+\sum_{\lambda'} \beta_{\lambda'} Y_{\lambda' o}\right)\right)/a_d\right)}{\left(1+\exp\left(\left(r - r_d A^{1/3}\left(1+\sum_{\lambda'} \beta_{\lambda'} Y_{\lambda' o}\right)\right)/a_d\right)^2} \right\} Y_{\lambda o}(\theta') d(\cos\theta') \qquad (9)$$

The Schrodinger equation of the total system is

$$(H - E)\,\Psi = 0 \tag{10}$$

Equations (4) and (7) are substituted into eq. (10), and multiplied on the left by $(\mathcal{Y}_{\ell_n j_n} \otimes \Phi_{I_n})_{JM}$, then it is integrated over target internal coordinates to form a set of coupled equations

$$\left(\frac{h^2}{2m}\frac{d^2}{dr^2} - \frac{\ell_n(\ell_n+1)}{r^2} - V_{diag} + E_n\right) R_{J_n \ell_n j_n}(r)$$

$$= \sum_{n'\ell_{n'}j_{n'}} \langle (\mathcal{Y}_{\ell_n j_n} \otimes \Phi_{I_n})_{JM} | V_{couple} | (\mathcal{Y}_{\ell_{n'} j_{n'}} \otimes \Phi_{I_{n'}}) \rangle R_{J_{n'}\ell_{n'}j_{n'}} \tag{11}$$

The nuclear structure is contained in the matrix element in eq. (11). A complete description of their evaluation for various collective models is given by T. Tamura.[33] To complete the evaluation of the differential cross-section the coupled equations need to be solved. The asymtotic wave functions are written in a partial wave expansion in a Coulomb field about the set of wave function $(\mathcal{Y}_{\ell_j} \otimes \Phi_I)_{JM}$. When this is done the two wave functions are matched at a radius sufficiently large for the projectile to be considered free of the nuclear field. A set of phase shifts are found and used to compute the elastic and inelastic cross-sections. For excited states only outgoing waves are needed since they are taking flux out of the beam with a different energy and character.

In even mass rotational nuclei the inclusion of the first low-lying strongly excited 2^+ state reduces the imaginary strength by approximately half. This

effect is most noticeable for proton and deuteron scattering. For higher z projectiles, the effect on the imaginary strength is smaller. If it were possible to describe all the incident channels analytically, the imaginary term would, of course, be reduced to zero. The addition of the quadrupole term, even if small, has the effect of producing a more realistic radial wave function than that of the simple optical model.

B. Coupled-Channel Born Approximation

The coupled-channel Born approximation (CCBA) that is used in this study is basically an extension of the distorted wave Born approximation (DWBA). The incident and exit wave functions are not simple optical model wave functions but are coupled-channel wave functions generated by the method outlined in the previous section. This generalization was formulated by Penny and Satchler,[23] and reformulated more concisely by T. Tamura.[35] The source term method expounded by Glendenning,[24, 25, 36] Ascuitto,[24, 25] and Mackintosh[36] predicted similar results and in ref. 36 it has been shown analytically these other methods are the same as the Penny and Satchler formulation. The amplitude for a transfer reaction A(a, b) B with $a = b + x$ is schematically written as[22]

$$T = \langle \psi_b^{(-)} (r_B, r_{bx}, r_b) \,|\, V(r, r_{bx}) \,|\, \psi^{(+)} (r_A, r_{ax}, r_a) \rangle \qquad (12)$$

where the projectile is not excited by its own scattering, and the internal structure of b and x remain unchanged.

The following discussion is based on the unpublished thesis by R. O. Nelson.[23] The formulation of stripping is used for the final state. The

Hamiltonian is written for the bB system and the Schrodinger equation is

$$(H_B + T_{bB} + V_{bB} - E) \mid \psi > = 0 \tag{13}$$

where H_B is the Hamiltonian for the final nucleus B, and T_{bB} and V_{bB} are the kinetic and potential energy operators respectively. The interaction potential U_{bB} is introduced as a generalized coupled-channel optical model potential describing elastic and higher order scattering in the bB system. Eq. (13) can be rewritten as

$$(H_B + T_{bB} + U_{bB} - E) \mid \psi > = - (V_{bB} - U_{bB}) \mid \psi > \tag{14}$$

Similarly for the aA system a wave function, $\mid \psi^{\circ}_{aA} >$, is defined to describe the elastic and higher-order scattering as

$$(H_A + T_{aA} + U_{aA} - E) \mid \psi_{aA}^{\circ} > = 0 \tag{15}$$

where H_A, T_{aA} and U_{aA} are analogous to H_B, T_{bB} and U_{bB}. The wave function $\mid \psi^{\circ}_{aA} >$ is expanded as

$$\mid \psi_{aA}^{\circ} > = \phi_a \sum_i \phi_i^{\circ} \mid i > \tag{16}$$

where ϕ_a is the incident projectile wave function. The ϕ_i denotes the relative motion and the wave function $\mid i >$ describes the internal structure of A with the condition

$$H_A \mid i > = E_i^{*} \mid i > \tag{17}$$

The eigenenergy E_i is the energy of the ith level in nucleus A. The wave

function ϕ_i° must satisfy the set of coupled equations introduced previously.

$$(T_{aA}-E_i)\,\phi_i^\circ + \sum_i \langle i \mid U_{aA} \mid i' \rangle \phi_{i'}^\circ = 0 \qquad (18)$$

where $E_i = E - E_i^*$. The Born approximation is made with

$$\mid \Psi \rangle \simeq \mid \Psi_{aA}^\circ \rangle \qquad (19)$$

Within the projectile a and target A system, the cases considered are mainly the elastic scattering and a few channels in the inelastic scattering. Once approximated eq. (14) is rewritten as

$$(H_B + T_{bB} + U_{bB} - E) \mid \Psi \rangle = (U_{bB} - V_{bB}) \mid \Psi_{aA}^\circ \rangle \qquad (20)$$

The wave function $|\Psi\rangle$ is similarly expanded as

$$\mid \Psi \rangle = \phi_b \, \phi_x \sum_{f'} \phi_{f'} \mid f \rangle \qquad (21)$$

where the ground state of the incident projectile b is ϕ_b and wave function of the transferred nucleon is ϕ_x. As before $\phi_{f'}$, represents the relative motion and $|f\rangle$ describes the internal structure of B. The wave function satisfies a similar requirement as in eq. (17). Now eq. (21) is used in eq. (20), and $\langle\Psi|$ is multiplied to the left of both sides of the equation and integrated to get

$$(T_{bB} - E_f)\,\phi_f + \sum_{f'} \langle f \mid U_{bB} \mid f' \rangle \phi_{f'}$$

$$= -\sum \langle \phi_b \, \phi_x \phi_f \; f \mid V_{bB} - U_{bB} \mid i \; \phi_a \, \phi_i^\circ \rangle \qquad (22)$$

The additional assumption, $V_{bB} \simeq U_{bB}$, is made and then the right hand side

of eq. (22) is zero. The relative motion wave function ϕ_f is changed to ϕ_f° a solution of the coupled set of equations on the left-hand side. Eq. (14) becomes

$$(H_B + T_{bB} + U_{bB} - E) \mid \psi_{bB}^\circ > = 0 \tag{23}$$

The transition amplitude from the aA system to the fth final state of B is given by Wu and Ohmura[37] as

$$T_f = < f \psi_{bB}^\circ \mid (V_{bB} - U_{bB} \mid \psi > \tag{24}$$

The potential $(V_{bB} - U_{bB})$ is approximately equal to V_{bx} the potential between the transferred particle and exit projectile. With this done the CCBA transition amplitude becomes

$$\begin{aligned} T_f &= \sum_i < \phi_f^\circ \phi_b \phi_x f \mid V_{bx} \mid i \phi_a \phi_i^\circ > \\ &= \sum_i \int \phi_f^{\circ *} < f \mid i > < \phi_b \phi_x \mid V_{bx} \mid \phi_a > \phi_i^\circ \, d\vec{r}_{Ax} \, d\vec{r}_{bx} \end{aligned} \tag{25}$$

This approximation has had reasonable success in describing experimental data.

The zero range approximation is made with

$$< \phi_b \phi_x \mid V_{bx} \mid \phi_a > = N_o \, \delta (\vec{r}_{bx}) \tag{26}$$

This approximation eliminates the integration over $\vec{r}_{bx}$ yield

$$T_f = N_o \sum_i \int \phi_f^{\circ *} \left(\frac{m_A}{m_B} \vec{r}_{Ax} \right) < f \mid i > \phi_i^\circ (\vec{r}_{Ax}) \, d\vec{r}_{Ax} \tag{27}$$

The constant N_o is

$$N_o = \frac{D_o \nu e^2}{2_s + 1} \tag{28}$$

where c is an isospin factor, s is the spin of the transferred particle, ν is the number of particles in a, and D_o is a constant describing the overlap in eq. (26).

The cross-section for an unpolarized system can be written as

$$\frac{d\sigma}{d\Omega} = \frac{M_{Aa} M_{Bb}}{(2\pi\hbar)^2} \frac{K_{Bb}}{K_{Aa}} \frac{1}{(2J_A+1)(2s_a+1)} \sum_f T_f^2 \tag{29}$$

The nuclear structure information is in the overlap $\langle f | i \rangle$. The states $| i \rangle$ and $| f \rangle$ are expanded in states of good angular momentum. Then the overlap can be calculated in order to factor out the spectroscopic amplitudes.

Chapter IV

NUCLEAR MODELS

A. Collective Model Formalism

The strong coupling model for deformed nuclei has for many cases described successfully level systematics for a given nucleus. The model consists of a nucleon coupled to an even-even core. A stably deformed potential is used that is proportional to the shape of core. The discussion below follows that of Davidson[38], Nilsson[2], Webb[39] and Nelson.[23]

1. Basic Concepts

The angular momentum of the core is $\vec{L}$ and is coupled to the extra-core nucleon with angular momentum $\vec{j}$ to form the total nuclear angular momentum $\vec{I}$ as

$$\vec{I} = \vec{L} + \vec{j}$$

The angular momentum $\vec{j}$ consists of an orbital part $\vec{\ell}$ and spin $\vec{s}$. The projections of $\vec{I}$ and $\vec{j}$ on the body fixed 3 axis are K and Ω respectively. In the space fixed system the projection of $\vec{I}$ onto z is M. The following diagram represents this coupling.

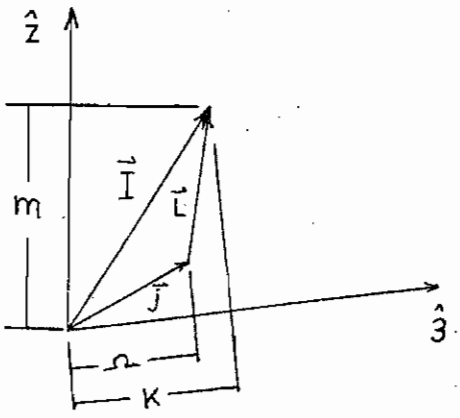

For a general potential the only constant of motion is $\vec{I}$. It is convenient to have axial and reflection symmetry about the body fixed axis. For this, the projection of $\vec{L}$ on the 3 axis is zero and therefore K is equal to Ω. Now, Ω is a constant of motion, but $\vec{j}^2$ is not if there is any nuclear deformation. Axial symmetry also implies that

$$\mathcal{J}_1 = \mathcal{J}_2 = \mathcal{J}_0$$

The Hamiltonian can be written as the sum of three terms

$$H = H_{ROT} + H_{part} + H_{cor} \tag{30}$$

where

$$H_{ROT} = \frac{h^2}{2\mathcal{J}_o} \left(I(I+1) - 2K^2 \right) \tag{31}$$

$$H_{part} = \frac{p^2}{2m} + V(\vec{r}, \vec{\ell}, \vec{s}) + \frac{h^2}{2\mathcal{J}_o} j^2 \tag{32}$$

$$H_{cor} = -\frac{h^2}{\mathcal{J}_o} \left(I_1 j_1 + I_2 j_2 \right) \tag{33}$$

H_{cor} can be rewritten using the raising and lowering operators $0_{\pm} = 0_1 \pm i\, 0_2$ to get

$$H_{cor} = -\frac{h^2}{2\mathcal{J}_o} \left(I_+ j_- + I_- j_+ \right) \tag{34}$$

With Ω a constant of motion, the particle function can be described as with

$$H_{part} | \Omega > = E_{\Omega} | \Omega > \tag{35}$$

The rotational wave function, including $|\Omega\rangle$, is denoted as $|EIMK\rangle$. This

wave function is a solution of the Schrodinger equation

$$H_{ROT} \mid E\ IMK > = \frac{h^2}{2\mathcal{I}_o} (I(I+1)-2K^2) \mid EIMK > \qquad (36)$$

Within the same band other than for $K = \Omega = 1/2$ orbits the coupling term H_{cor} which connects states with $\Delta K = \pm 1$ contributes nothing to the eigenenergy. Therefore the equations become

$$H \mid EIMK = \Omega > = E_{I,K} \mid EIMK = \Omega >$$

$$E_{I,K} = \frac{h^2}{2\mathcal{I}_o} (I(I+1) - 2K^2) + E_{\Omega} \quad \text{for} \quad I \geq K \qquad (37)$$

The particle state function $\mid \Omega \rangle$ is expanded in terms of an isotropic, pseudospherical, functions $\mid j\Omega \rangle$ as

$$\mid \Omega > = \sum_j c_{j\Omega} \mid j\Omega > \qquad (38)$$

The coupling term H_{cor} has a diagonal term only for $K = 1/2$. The matrix element for $K = 1/2$ is

$$< EIM\ 1/2 \mid H_{cor} \mid EIM\ 1/2 > = (-1)^{I+1/2} \frac{h^2}{2\mathcal{I}_o} (I+1/2)\, a \qquad (39)$$

where a the decoupling parameter is

$$a \equiv - \sum_j (-1)^{j+1/2} (j+1/2) \mid c_{j\ 1/2} \mid^2 \qquad (40)$$

Then the properly symmetrized wave function is written as

$$EIMK > = \frac{1}{\sqrt{2}} \sum_j c_{jK} (D^I_{MK}(\phi,\phi) \mid jK > + (-1)^{I-j} D^I_{M-K} \mid j-K >) \qquad (50)$$

2. Nilsson Model Wavefunctions

The solution of the particle part of the Hamiltonian describes the odd nucleon. In this model the potential is an anisotropic harmonic oscillator with axial symmetry. The Hamiltonian for H_{part} can be written as

$$H_{part} = \frac{p^2}{2m} + \frac{m}{2}(\omega_o^2 (x_1^2 + x_2^2) + \omega_3^2 x_3^2) + C\,\vec{l}\cdot\vec{s} + D\,\vec{l}^2 \qquad (51)$$

The constant C represents spin-orbit splitting and D is a strength that depresses high angular momentum states. The oscillator strength $\hbar\omega_o = 41/A^{1/3}$ MeV is introduced with redefinitions $K = C/\hbar\omega_o$ and $\mu = D/(K\hbar\omega_o)$. As in Davidson,[38] the H_{part} can be written in the form of an equation with a spherical harmonic as

$$H_{part} = -\frac{\hbar\omega_o}{2}(\nabla^2 - \rho^2) - \hbar\omega_o \beta \rho^2 Y_{2o} + 2K\vec{l}\cdot\vec{s} + \mu K \vec{l}^2 \qquad (52)$$

where dimensionless co-ordinates ρ are used with

$$q_K = \sqrt{\frac{m\omega_o}{h}}\, x_K \quad \text{and} \quad \rho^2 = \sum_{k=1}^{3} q_K^2$$

As before the wave function for H_{part} is $|\Omega\rangle$ which is expanded in a spherical basis. With the Hamiltonian known the coefficients $C_{j\Omega}$ can be calculated. First H_{part} is rearranged as

$$H_{part} = H_{diag} + H_{couple} \qquad (53)$$

where

$$H_{diag} = -\frac{\hbar\omega_o}{2}(\nabla^2 - \rho^2) \qquad (54)$$

$$H_{couple} = -\hbar\omega_o \beta \rho^2 Y_{20} + 2K\vec{l}\cdot\vec{s} + \mu K \vec{l}^2 \tag{55}$$

The H_{couple} connects states similar to the way developed for the coupled-channel wave functions. With H_{diag} diagonal, E_o^N is defined as

$$H_{diag} \mid j\,\Omega > = E_o^N \mid j\,\Omega > \tag{56}$$

The complete Schrödinger equation is

$$\begin{aligned} &(H_{diag} + H_{couple}) \mid \Omega > = E_o^{\Omega} \mid \Omega > \\ &\sum_j c_{j\Omega} (H_{diag} + H_{couple}) \mid j\Omega > = \sum_j E_o^{\Omega} c_{j\Omega} \mid j\,\Omega > \end{aligned} \tag{57}$$

This equation is multiplied by $\langle j'\Omega \mid$ from the left and eigenvalues of the diagonal part used for

$$\sum_j c_{j\Omega} (E_o^N \delta_{jj'} + \langle j'\Omega \mid H_{couple} \mid j\Omega >) = \sum_j E_o^{\Omega} c_{j\Omega} \delta_{jj'} \tag{58}$$

$$E_o^N \; c_{j'\Omega} + \sum_j c_{j\Omega} \langle j'\Omega \mid H_{couple} \mid j\Omega > = E_o^{\Omega} c_{j'\Omega} \tag{59}$$

and rearranged as

$$\sum_j c_{j\Omega} \langle j'\Omega \mid H_{couple} \mid j\,\Omega > = (E_o^{\Omega} - E_o^N)\, c_{j'\Omega} \tag{60}$$

This is a coupled set of equations which allows the determination of $c_{j\Omega}$ coefficients. These coefficients describe the decomposition of $|\Omega\rangle$ into a basis where the calculation can proceed. The orbits are designated by

(N, n_z, Λ) or a Nilsson orbit number. The N is the major shell number, n_z is a pseudo-projection of N, and Λ is the projection of $\vec{\ell}$ on the body fixed 3 axis.

The Nilsson model based on a harmonic oscillator basis has described the structure of deformed nuclei successfully. Level orderings and band structure can qualitatively be understood as well as transition rates and particle transfer amplitudes.

3. Deformed Woods-Saxon Model Wave Functions

Another approach to the solution of the particle part of the Hamiltonian is to substitute a real Woods-Saxon type potential for $V(\vec{r}, \vec{\ell}, \vec{s})$. The radius is expanded through the quadrupole term, and then the formalism developed for the Nilsson model wave functions will yield another set of eigenvectors and eigenvalues. However in this case values for the real potential strength and spin-orbit strengths can be chosen to be similar to those found necessary for spherical nuclei. Briefly the expansion leads to a diagonal and coupling part for the potential as

$$V(r, \theta) = V_{diag}(r) + V_{couple}(r, \theta). \tag{61}$$

A feature of this potential is that higher angular momentum wave function are found to contribute to $|\Omega\rangle$. As before a set of coupled differential equations can be written for the radial parts of $|\Omega\rangle$, $U_{j\Omega}(r)$. A bound state solution is obtained from the equation

$$\{ -\frac{h^2}{2m}(\nabla_r^2 + \frac{\ell(\ell+1)}{r^2}) - V_{so}\frac{1}{r_{so}}\frac{d}{dr_{so}} f(r, r_{so}, a_{so})\vec{\ell}\cdot\vec{s}$$

$$- V f(r, r_o, a_o) - E_o^{\Omega} \} U_{j\Omega}(r)$$

$$= -\sum_{j'} \langle j\Omega | V_{couple}(r,\theta) | j'\Omega \rangle U_{j'\Omega}(r) \qquad (62)$$

This equation was solved numerically by Rost[40] and by T. Tamura.[41] The coefficient C_j is defined for comparison as

$$c_{j\Omega}^2 = \int_0^{\infty} U_j^2 \ (r)\ dr \qquad (63)$$

where the sign of $C_{j\Omega}$ is determined by the choice of phase convention for the radial wave functions. The program of T. Tamura named NEPTUNE[41] was used extensively to calculate single particle orbitals in a deformed potential (see Appendix B). The radial wave functions that have been calculated in this realistic potential unlike the infinite potential of the hormonic oscillator (Nilsson) are better suited for use as form factors in a particle transfer reaction or use in calculating matrix elements.

4. Bandmixing

Only orbits unperturbed by the existence of other single particle states have been considered in the preceding section, but in fact these unmixed states are rare in nature. Having developed a set of wave functions $|\Omega\rangle$ that describe odd-A rotational bands without mixing, the coupling term H_{cor} can be included to mix orbits with $\Delta K = \pm 1$. The coupling term is also called coriolis coupling. A mixed wave function may be written in terms of unmixed

wave functions as

$$\Phi(\text{mix}) = \sum_{\substack{n \\ \text{orbits}}} \alpha_{IK_N} \left| EIMK_N \right> \tag{64}$$

where the sum is over the active orbits. The Scrödinger equation is written as

$$H\Phi(\text{mix}) = (H_{ROT} + H_{part} + H_{cor})\Phi(\text{mix}) = E\Phi(\text{mix}) \tag{65}$$

As in the derivation for the wave functions a set of equations can be written relating the components of the mixed wave function with

$$\sum_{N'} \left< EIMK_N \right| H_{cor} \left| EIMK_{N'} \right> \alpha_{IK_{N'}} = (E - E_{K_N}) \alpha_{IK_N} \tag{66}$$

The coupling term is non zero for $K = 1/2$ bands and for $K_n - K_{n'} = \pm 1$. The matrix element is given by Davidson[42] as

$$\left< EIMK_N \right| H_{cor} \left| EIMK_N \right> = -\frac{\hbar^2}{2\mathcal{I}} \sum_j c^*_{jK_{N'}} c_{jK_N}$$

$$\{ (\delta_{K_{N'}, K_N - 1} + (-1)^{I-j} \delta_{K_{N'}, -K_N + 1} \} \sqrt{(I+K_N)(I-K_N+1)(j+K_N)(j-K_N+1)}$$

$$+ \sqrt{(I-K_N)(I+K_N+1)(j-K_N)(j+K_N+1)}\, \delta_{K_{N'}, K_N + 1} \tag{67}$$

The effect of mixing deformed orbits is to reorder and change the character of an energy state. A mixed state no longer has good K. Intraband and interband transitions are altered by even small admixtures. Different moments of inertia could be used for each orbit, but this extra parameterization implies that the core is not good. In this work one moment of inertia for all orbits has been used for simplicity.

A more critical problem is the population of the different active orbits. In a simple model a nucleon below the Fermi energy has probability unity and if it is unbound the probability is zero. This can be used, but the Fermi surface is not that sharp. The formalism of pairing as used by S. T. Belyaev,[43] S. Yoshida[44] and B. L. Cohen[45] can be followed. The concept is that an orbit has a probability of it being occupied by a nucleon. An example of such a probability is given by B. L. Cohen[45] for spherical single particle orbits

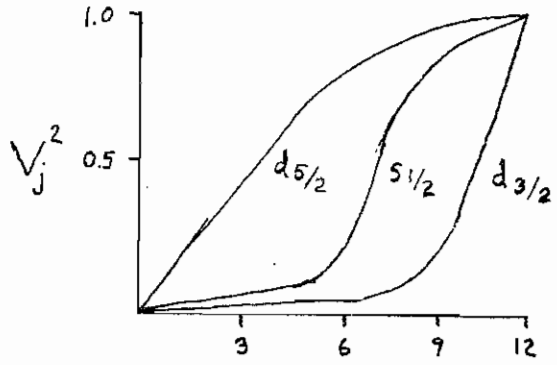

Number of nucleons in the sd shell

The probability of finding nucleons in the orbits d 5/2, s 1/2 and d 3/2 are given roughly by this sketch. In the case of deformed single particle states the d 5/2 splits into three orbits, the s 1/2 does not split, and the d 3/2 splits into two orbits. A similar drawing could be made for a given deformation in which each deformed orbit could have two nucleons.

A set of equations describing the effect of pairing are

$$E_j = \sqrt{(\epsilon_j - \lambda)^2 + \Delta^2}$$

$$V_j^2 = 1/2 \left(1 - \frac{\epsilon_j - \lambda}{E_j}\right)$$

$$N = \sum_j (2j+1) V_j^2$$

$$V_j^2 + U_j^2 = 1 \qquad (68)$$

$$\Delta = G \sum_j U_j V_j$$

where Δ is half the energy gap, G is the pairing force strength, V_j^2 is probability that an orbit is occupied. U_j^2 is probability that an orbit is empty, N is total number of nucleons, λ is the Fermi energy, and E_j is the uncorrected single particle energy of the particle in orbit K. This set of equations provides a method by which the probability amplitudes can be selected in a self-consistent way in reagrd to band-head energies. The uncorrected single particle energies were taken as the intrinsic $\vec{j}^2$ term and the band-head energy, E_{bh}, calculated from fig. 7 or from the tables in appendix B. The starting values for the V_j^2 and E_{bh} were later adjusted. These new values were used with the constraint of satisfying these equations, especially to one which counts the number of particles.

5. Spectroscopic Factor for Nucleon Transfer Reactions

The spectroscopic amplitude A_j measures the overlap of the final state with the initial state coupled to the transferred nucleon. In the work of Satchler[46] a formalism was developed for rotational nuclei in which it is assumed that the deformation of the initial and final rotor states are very similar. Their overlap is then essentially unity. The amplitude derived by Satchler is given by

$$A_j = c_{jk}\, \rho\, (j\ L\ K\ 0 \mid L'\ K) \sqrt{\frac{2L+1}{2L'+1}} \qquad (69)$$

The $(A\ B\ a\ b \mid C\ c)$ is a Clebsch-Gordon coefficient and ρ is $\sqrt{2}$ if $K=0$ and unity otherwise. The angular moments $\vec{L}$ and $\vec{L'}$ are for the initial and final rotors respectively. This result was expanded for mixed wave functions by Nelson.[23] The spectroscopic amplitude for stripping can be written as

$$A_j = \rho \sqrt{\frac{2I_A+1}{2I_B+1}} \sum_{\substack{n \\ \text{orbits}}} \alpha_{I_B K_n}\, c_{j K_n} (I_A\, j\, K_A\, K_B - K_A \mid I_B K_B)\, U_n \qquad (70)$$

where U_n^2 represents the emptiness of orbit K_n. U_n is taken as the positive value. For the inverse reaction the V_n^2 is used to tell how much it is filled and the angular part is reordered.

A method of transferring a stripping amplitude to a pickup is given by T. Udagawa[47] as

$$A_j(\text{pickup}) = \sqrt{\frac{2I_A+1}{2I_B+1}}\ (-1)^{I_B + j - I_A}\ A_j(\text{stripping}) \qquad (71)$$

Instead of a simple ratio of spin states an important phase factor is also needed. In a CCBA analysis both the magnitude of the amplitudes and the way the various amplitudes add coherently is tested.

B. Theoretical Predictions

Single particle calculations were made with NEPTUNE and with the assumption that ^{29}Si is oblate and ^{29}Al is prolate. The experimental separation energy for a neutron or proton from ^{30}Si was used in NEPTUNE to determine a real well strangth for a given deformation β_2 in the ground state for each nucleus. For ^{29}Si the neutron was from the $K^{\pi}=1/2^{+}(211)$ orbit and for ^{29}Al the proton was from the $K^{\pi}= 5/2^{+}(202)$ orbit. From preliminary bandmixing results with the Nilsson model wave functions and with results from NEPTUNE the deformation for ^{29}Si was fixed at $\beta_2 = -0.2$ and for ^{29}Al at $\beta_2 = 0.1$. In fig. 7 are the orbits charted as a function of β_2 in a deformed Woods-Saxon potential for the ^{29}Si system (see Appendix B for a more complete description including tables for wave functions of these orbits). From either the calculated tables in Appendix B or fig. 7 a first approximation to the bandhead energies, E_{bh}, can be made from the difference in energy of the unmixed excited orbits to the ground state orbit. The bandmixing calculations were then performed with the Erskine code BANDMIX, which as been modified to include the intrinsic $\vec{j}^2$ term. The calculations to be discussed below used wave functions obtained with the code NEPTUNE. The occupation probabilities were chosen to improve calculated nucleon transition amplitudes and energy spectrum for each nuclei. The bandhead energies were adjusted as parameters to optimize the calculated energy levels relative to the experimental ones.

The parameters used for ^{29}Si are given in table I with a moment of

Figure 7. Energy of an orbit with $K^{\pi}(Nn_z\Lambda)$ in a deformed Woods-Saxon potential. Parameters for ^{29}Si are real strength V= 54.2 MeV, $r_o = r_{so} = r_c = 1.25$ fm $a_o = a_{so} = 0.65$ fm and $V_{so} = 7.5$ MeV as a function of deformation β_2. The energy is a binding energy defined with zero at top and increasing downward into the potential. See Appendix B for more description and tables for $-0.4 \leq \beta_2 \leq 0.4$ in 0.1 increments. Orbit numbers are also shown on the left side.

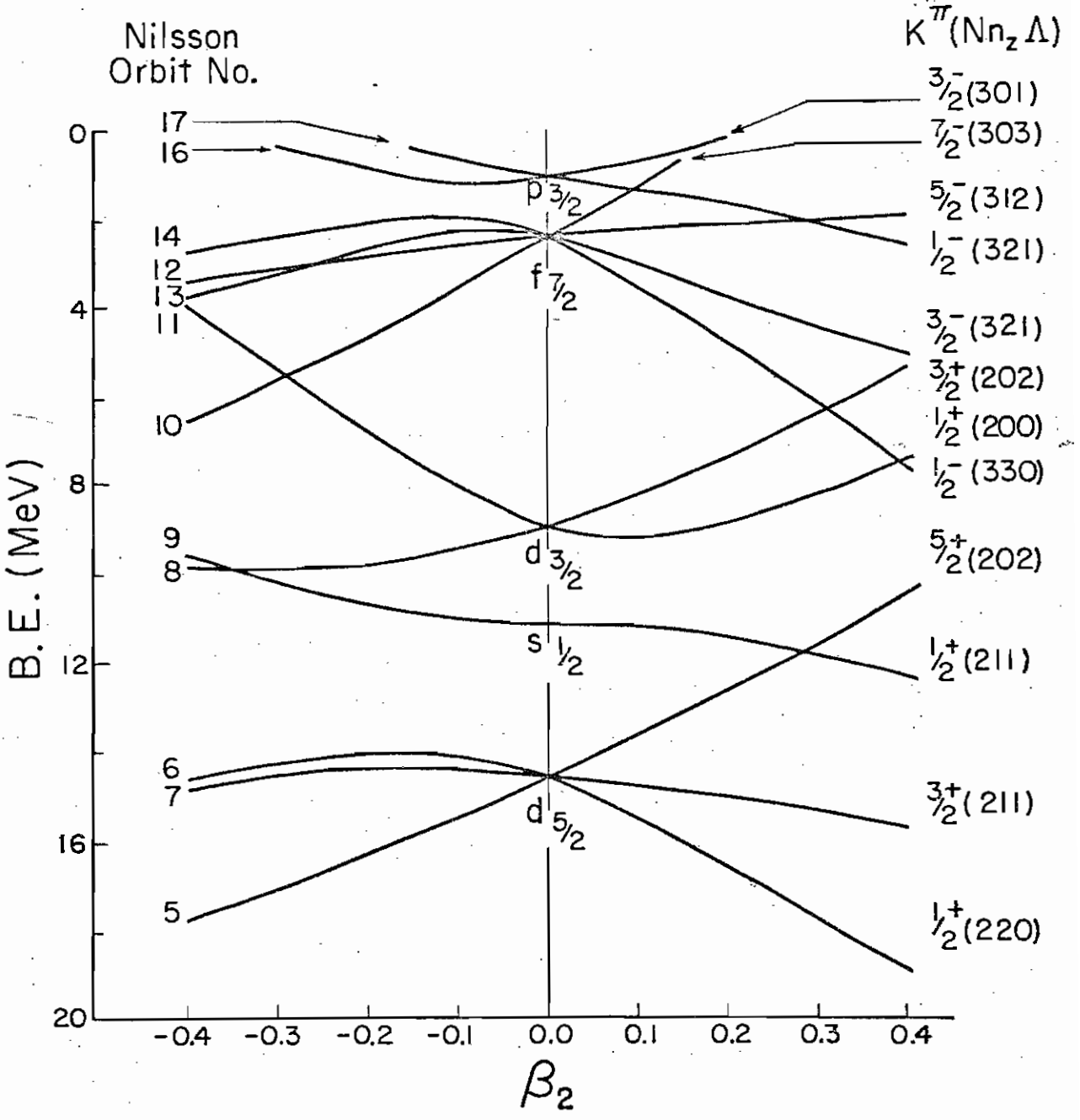
Nilsson
Orbit No.
$K^{\pi}(Nn_z\Lambda)$
17
16
14
12
13
11
10
9
8
6
7
5
$p_{3/2}$
$f_{7/2}$
$d_{3/2}$
$s_{1/2}$
$d_{5/2}$
$3/2^-(301)$
$7/2^-(303)$
$5/2^-(312)$
$1/2^-(321)$
$3/2^-(321)$
$3/2^+(202)$
$1/2^+(200)$
$1/2^-(330)$
$5/2^+(202)$
$1/2^+(211)$
$3/2^+(211)$
$1/2^+(220)$
B.E. (MeV)
0
4
8
12
16
20
-0.4
-0.3
-0.2
-0.1
0.0
0.1
0.2
0.3
0.4
β_2

Table I. Parameters for the bandmixing calculation done for ^{29}Si. V_j^2 is a population for each orbit labeled by number and Nilsson quantum numbers. E_{bh} is the bandhead energy. Deformation is -0.20 and inverse moment of inertia A is 320 keV.

Orbit No.	$K^{\pi}(Nn_z\Lambda)$	V_j^2 [a]	E_{bh}(MeV) [b]
5	$5/2^+$ (202)	1.00	5.20
7	$3/2^+$ (211)	1.00	4.00
6	$1/2^+$ (220)	0.98	3.60
9	$1/2^+$ (211)	0.85	0.00
8	$3/2^+$ (202)	0.14	1.30
11	$1/2^+$ (200)	0.02	6.20
10	$7/2^-$ (303)	0.005	-2.42 [c]
13	$3/2^-$ (312)	0.005	0.72 [c]

[a] Based on E_{bh} values and adjusted.

[b] Taken from table XI and adjusted.

[c] Adjusted to match the 3.623 MeV and 4.935 MeV levels in ^{29}Si respectively.

inertia of 0.32 MeV for each orbit. This nucleus presents a problem in that two low lying bands, orbits 8 and 9, describe the energy spectrum rather well[13], but at the same time fails to predict good spectroscopic information. It was necessary to use six orbits in order to have a reasonable direct amplitude for the important 2.028 MeV level. The negative parity bands present a problem in that the first orbit, no. 10 $7/2^-(303)$, is so low that the bandhead energy must be set to a negative value when the level is matched to the $J^\pi = 7/2^-$ level at 3.623 MeV. The next negative parity state at 4.935 MeV has $J^\pi = 3/2^-$ and a second bandhead must be assumed based on orbit 13 $3/2^-(321)$. Finally a calculation was made which assumed each orbit from the f 7/2 and p 3/2 splitting. Calculated bandheads and equal populations were also assumed. A $7/2^-$ state had the lowest excitation energy but surprisingly it was not from orbit 10 but was from the $K=1/2$ orbit no. 14 which has a large decoupling parameter. The spectroscopic amplitudes were not significantly different from the unmixed calculation, so for simplicity only the single band calculations were used for the negative parity states. Fig. 8 shows a level diagram for ^{29}Si with the experimentally known levels in the middle and rotational model with bandmixing calculation (BM) for a $\beta = -0.2$ on the right. The levels with a predominant amplitude corresponding to a beginning of a band are labeled by Nilsson quantum numbers. In table II are the calculated direct and indirect amplitudes for ^{29}Si. The corresponding levels can be identified easily for comparisons.

In table III the parameters are given for the ^{29}Al calculation with a

Figure 8. ^{29}Si energy level diagram and model predictions. The experimentally known results are in the center with the rotational model with bandmixing (BM) on the right and a shell model prediction[21] on the left. Levels in the BM model that are the bandheads are labeled by the Nilsson quantum numbers ($Nn_z\Lambda$).

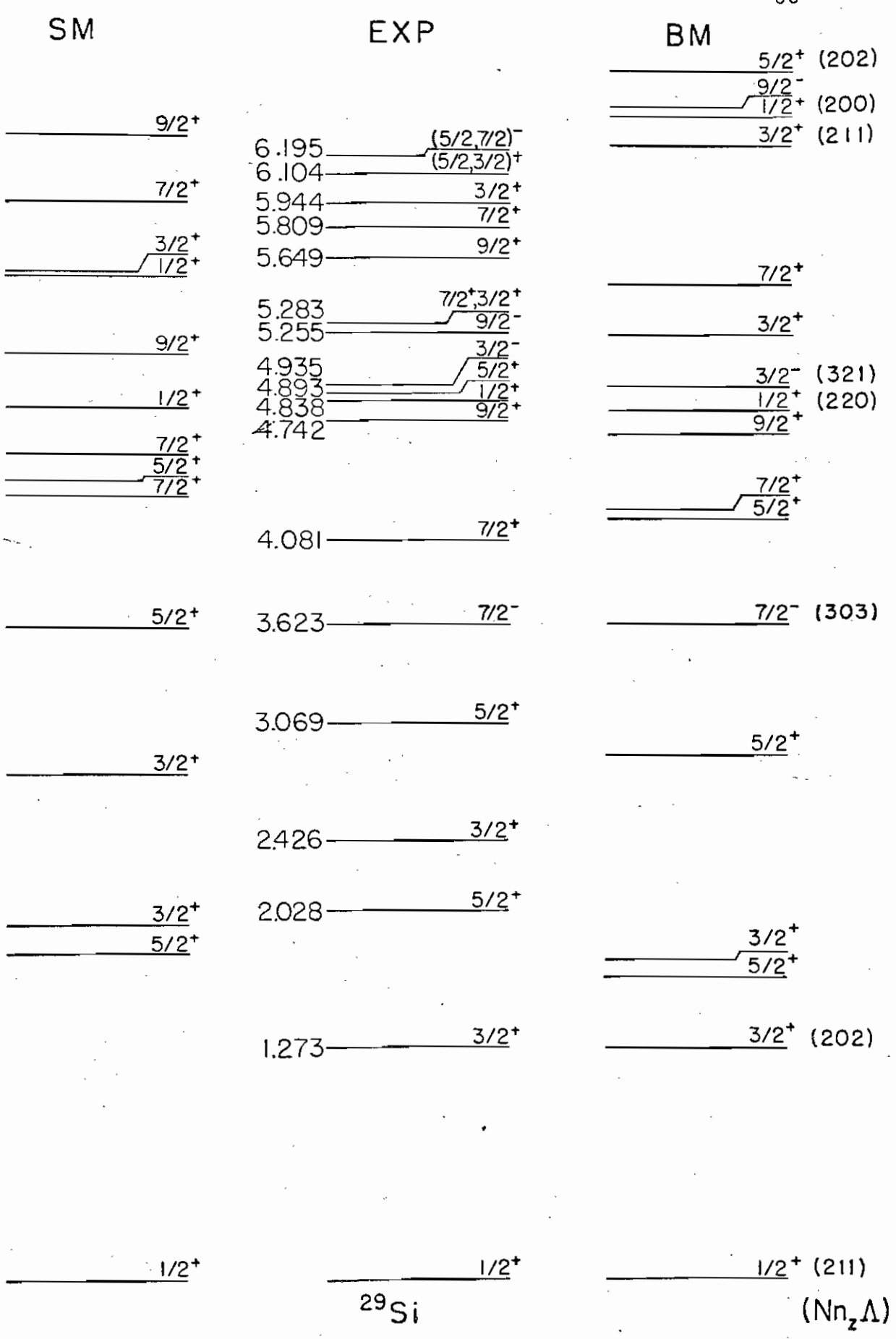
SM
EXP
BM
9/2+
7/2+
3/2+
1/2+
9/2+
1/2+
7/2+
5/2+
7/2+
5/2+
3/2+
3/2+
5/2+
1/2+
6.195
6.104
5.944
5.809
5.649
5.283
5.255
4.935
4.893
4.838
4.742
4.081
3.623
3.069
2.426
2.028
1.273
(5/2,7/2)−
(5/2,3/2)+
3/2+
7/2+
9/2+
7/2+,3/2+
9/2−
3/2−
5/2+
1/2+
9/2+
7/2+
7/2−
5/2+
3/2+
5/2+
1/2+
5/2+ (202)
9/2−
1/2+ (200)
3/2+ (211)
7/2+
3/2+
3/2− (321)
1/2+ (220)
9/2+
7/2+
5/2+
7/2− (303)
5/2+
3/2+
5/2+
3/2+ (202)
1/2+ (211)
29Si
(Nnz Λ)

Table II. The Spectroscopic Amplitudes, A_j, from the rotational model with bandmixing for ^{29}Si. The experimental (calculated) level energies are listed. The amplitudes are from the ground state or the first excited 2^+ state in ^{30}Si. The value of j refers to the type of form factor used, if j = 1/2 and the state is positive parity the transfer is 2s1/2. For a negative parity state with j = 3/2 the transfer would be by a 2p3/2 and so forth. Listed in order of calculated energy.

Energy in ^{29}Si (MeV) Exp(Cal)	Spin and Parity J^π	A_j for $0^+ \rightarrow J^\pi$	A_j for $2^+ \rightarrow J^\pi$			
		j = J^π	j = 1/2	j = 3/2	j = 5/2	j = 7/2
0.000(0.00)	$1/2^+$	-1.095		-0.245	0.202	
1.273(1.28)	$3/2^+$	0.793	-0.470	-0.006	-0.058	
2.028(1.67)	$5/2^+$	1.186	-0.681	0.229	-0.324	
2.426(1.77)	$3/2^+$	0.078	-0.521	-0.316	-0.194	
3.069(2.91)	$5/2^+$	-0.557	-0.092	0.345	0.066	
3.623(3.62)	$7/2^-$	0.099				0.069
4.896(4.21)	$5/2^+$	-1.802	-0.620	-0.138	0.197	
4.081(4.26)	$7/2^+$	0.048		0.465	0.057	
4.742(4.68)	$9/2^+$	0.165			1.219	
4.838(4.79)	$1/2^+$	-0.584		0.013	-0.568	

Table II. Continued

Energy in ^{29}Si (MeV) Exp(Cal)	Spin and Parity J^π	A_j for $0^+ \rightarrow J^\pi$ $j = J^\pi$	$j = 1/2$	A_j for $2^+ \rightarrow J^\pi$ $j = 3/2$	$j = 5/2$	$j = 7/2$
4.935(4.94)	$3/2^-$	-0.078		-0.035	-0.001	-0.024
5.283(5.22)	$3/2^+$	0.259	0.217	0.140	-0.843	
5.809(5.51)	$7/2^+$	0.001		0.232	0.815	
5.944(6.22)	$3/2^+$	-0.024	-0.102	0.123	-0.058	
(6.42)	$1/2^+$	-0.009		0.092	0.024	
5.255(6.50)	$9/2^-$	-0.001				0.065
(6.54)	$5/2^-$	0.002		-0.056	-0.000	0.029
6.104(6.66)	$5/2^+$	0.852	-0.223	0.047	0.973	
(6.90)	$7/2^+$	-0.034		-0.058	0.894	
5.649(7.31)	$9/2^+$	-0.048			-0.368	
(8.09)	$9/2^+$	-0.057			-0.459	

moment of inertia of 0.32 MeV for each orbit. Five positive parity bands were sufficient to calculate a reasonable energy spectrum. A single band calculation with orbit 14, $1/2^-(330)$, was carried out for the possible negative parity state at 3.19 MeV. The bands were chosen as those suggested by Jones et. al.[3] With many levels in ^{29}Al not established, assignments were made to facilitate discussion of calculated results. The 1.76 MeV level was assigned $7/2^+$ and the 2.23 MeV level $3/2^+$. Recent work of Williams et. al.[9] provides evidence for the elimination of the 5/2 spin assignments for these two levels. The rotational model with bandmixing calculation (BM) for a $\beta =$ 0.1 is shown in fig. 9 to the right of the experimentally known energy levels, exhibits a fairly good correspondence and confirms the suggestions of previous workers.[3] As before the dominant bandheads are labeled with the Nilsson quantum numbers. In table IV are the calculated direct and indirect amplitudes for ^{29}Al. The wave function for the ground state of ^{29}Al was used for the t = 3/2 8.34 MeV state in ^{29}Si.

Once the wave functions are known other properties such as electromagnetic transition rates, branching-ratios and lifetimes can be calculated. A code was written to calculate B(E2) and B(M1) transition rates from which other quantities could be calculated (the derivation of the formalism is described in Appendix C). The matrix elements were calculated with the deformed single particle solutions in a Woods-Saxon well as described earlier. The B(E2) and B(M1) transition rates are listed in table V, where the calculated bandmixing results are compared with the experimentally known values. In fig. 10 and fig. 11 are shown the calculated and experimental

Table III. Parameters for bandmixing calculation done for ^{29}Al. Deformation β_2 is 0.10 and inverse moment of inertia A is 320 keV.

Orbit No.	$K^{\pi}(Nn_z\Lambda)$	V_j^2 [a]	E_{bh}(MeV) [a]
6	$1/2^+$ (220)	0.98	3.80
7	$3/2^+$ (211)	0.95	1.80
5	$5/2^+$ (202)	0.90	0.00
9	$1/2^+$ (211)	0.15	3.10
11	$1/2^+$ (200)	0.01	4.15
14	$1/2^-$ (330)	0.01	3.19 [b]

[a] Initial guesses based on table XI for E_{bh} and pairing theory for populations.

[b] Adjusted to match the 3.19 MeV level in ^{29}Al.

Figure 9. ^{29}Al energy level diagram and model predictions. The experimentally known results are shown in the center with the rotational model with bandmixing (BM) on the right and a shell model prediction [20] on the left. The levels in the BM model that are bandheads are labeled by the Nilsson quantum numbers ($Nn_z\Lambda$).

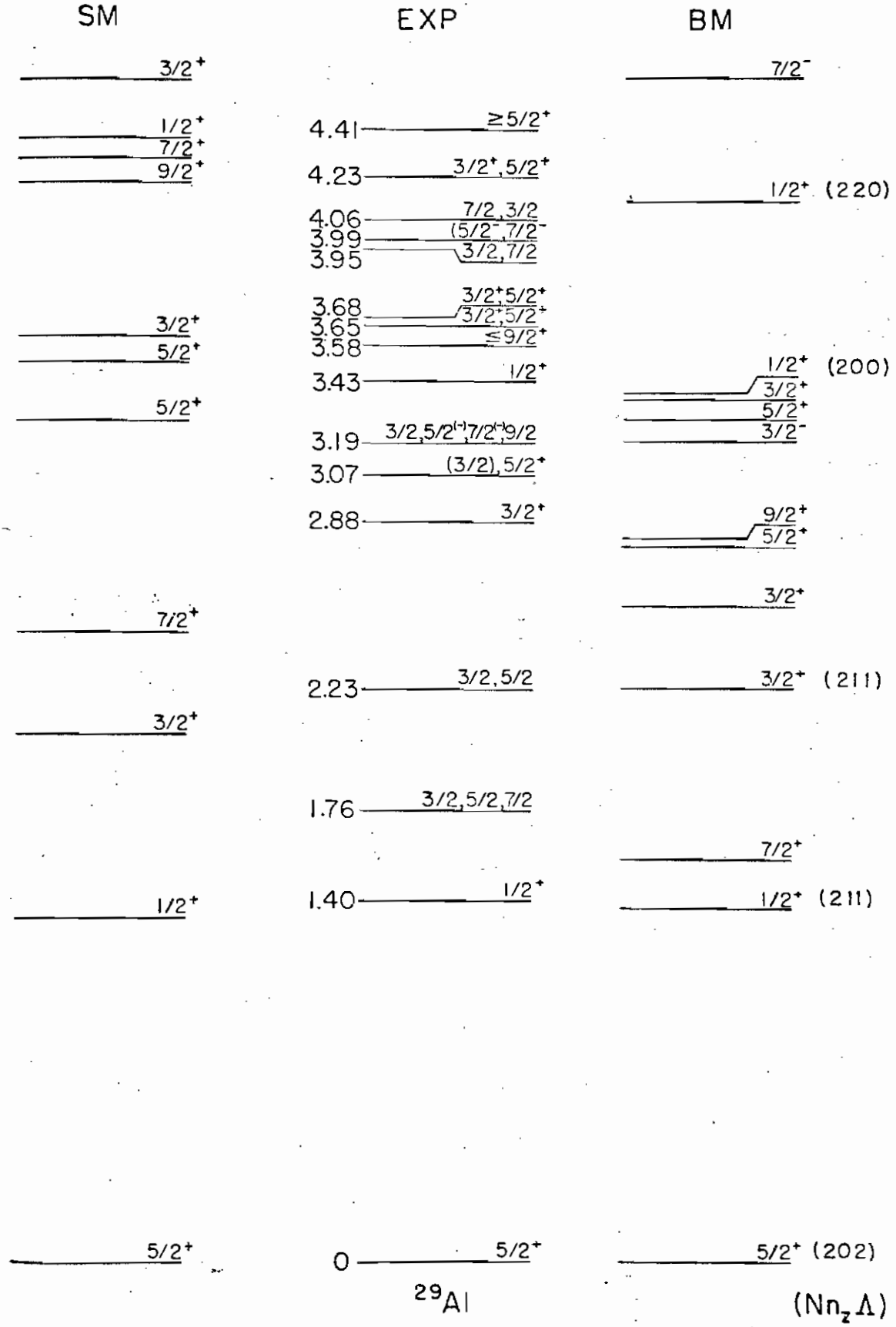
SM
EXP
BM
3/2+
1/2+
7/2+
9/2+
3/2+
5/2+
5/2+
7/2+
3/2+
1/2+
5/2+
4.41
≥5/2+
4.23
3/2+,5/2+
4.06
7/2,3/2
3.99
(5/2-,7/2-
3.95
3/2,7/2
3.68
3/2+5/2+
3.65
3/2+5/2+
3.58
≤9/2+
3.43
1/2+
3.19
3/2,5/2(-),7/2(-),9/2
3.07
(3/2),5/2+
2.88
3/2+
2.23
3/2,5/2
1.76
3/2,5/2,7/2
1.40
1/2+
0
5/2+
29Al
7/2-
1/2+ (220)
1/2+ (200)
3/2+
5/2+
3/2-
9/2+
5/2+
3/2+
3/2+ (211)
7/2+
1/2+ (211)
5/2+ (202)
(Nnz Λ)

Table IV. Pickup Spectroscopic Amplitudes from the rotational model with bandmixing for ^{29}Al. See table II for more complete description.

Energy in ^{29}Al (MeV) Exp(Cal)	Spin and Parity J^π	A_j for $0^+ \rightarrow J^\pi$ $j = J^\pi$	A_j for $2^+ \rightarrow J^\pi$ $j = 1/2$	$j = 3/2$	$j = 5/2$
0.00(0.00)	$5/2^+$	2.077	-0.038	-0.047	0.475
1.40(1.39)	$1/2^+$	-0.472		0.089	-0.015
1.76(1.55)	$7/2^+$	0.023		-0.044	1.198
2.23(2.24)	$3/2^+$	0.136	0.027	0.055	0.857
2.88(2.53)	$3/2^+$	0.269	0.164	-0.119	0.012
(2.75)	$9/2^+$	-0.102			1.293
3.07(2.81)	$5/2^+$	-1.009	0.034	0.054	0.870
3.19(3.19)	$3/2^-$	0.045	-0.004	-0.020	-0.001
(3.34)	$5/2^+$	0.316	-0.388	-0.074	-0.224
(3.35)	$3/2^+$	-0.135	-0.269	0.055	-0.041
3.43(3.49)	$1/2^+$	0.127		-0.098	0.002
(4.52)	$1/2^+$	-0.282		0.033	0.610
(5.16)	$7/2^+$	-0.011		0.177	0.003

Table V. Calculated transition strengths for the rotational model with bandmixing (BM) in comparison to experimentally known values (EXP) for ^{29}Si and ^{29}Al.

$E_i - E_f$ [a] (MeV)	B(E2) W.U. [b] EXP [c]	BM	B(M1) W.U. [b] EXP [c]	BM
^{29}Si				
1.273 - 0.000	5.1	5.6	0.011	0.039
2.028 - 0.000	9.8	10.6		
2.028 - 1.273		1.74	<0.01	0.93×10^{-4}
2.426 - 0.000	9	6.75	0.080	0.033
2.426 - 1.273	<9	11.1	0.13	0.53×10^{-3}
3.069 - 1.273	13	11.0	0.19	0.49×10^{-2}
4.081 - 1.273	10.4	10.6		
4.081 - 2.028	0.40	0.67	0.029	0.020
4.742 - 2.028	21	11.9		
^{29}Al				
1.40 - 0.00	4.4	2.73		

[a] Initial level to final level energies for that transition.

[b] Weisskopf Units (W.U.) as defined in ref. 49.

[c] From refs. 20, 49 and 10.

Figure 10. Branching Ratios and Lifetimes with BM model predictions for ^{29}Si. The BM model predictions are in brackets below the experimentally known values for the levels in ^{29}Si ordered by excitation energy (MeV). The lifetimes are in femtoseconds (fs = 10^{-15} sec). Deformation of -0.40 used.

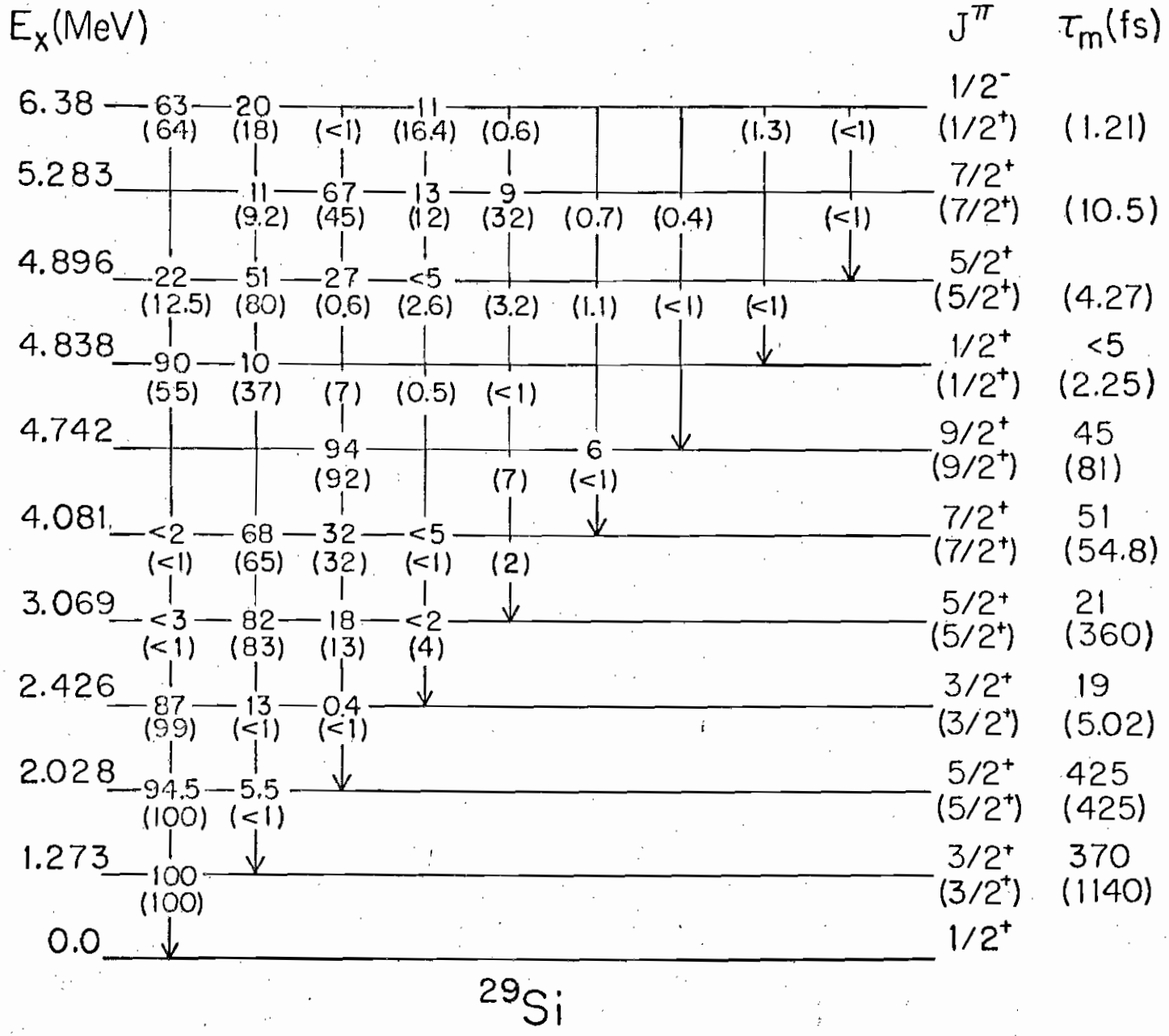
E_x(MeV)
J^π
τ_m(fs)
6.38
63 (64)
20 (18)
<1 (<1)
11 (16.4)
0.6 (0.6)
1.3 (1.3)
<1 (<1)
1/2⁻ (1/2⁺)
(1.21)
5.283
11 (9.2)
67 (45)
13 (12)
9 (32)
0.7 (0.7)
0.4 (0.4)
<1 (<1)
7/2⁺ (7/2⁺)
(10.5)
4.896
22 (12.5)
51 (80)
27 (0.6)
<5 (2.6)
3.2 (3.2)
1.1 (1.1)
<1 (<1)
<1 (<1)
5/2⁺ (5/2⁺)
(4.27)
4.838
90 (55)
10 (37)
7 (7)
0.5 (0.5)
<1 (<1)
1/2⁺ (1/2⁺)
<5
(2.25)
4.742
94 (92)
6 (7)
<1 (<1)
9/2⁺ (9/2⁺)
45
(81)
4.081
<2 (<1)
68 (65)
32 (32)
<5 (<1)
2 (2)
7/2⁺ (7/2⁺)
51
(54.8)
3.069
<3 (<1)
82 (83)
18 (13)
<2 (4)
5/2⁺ (5/2⁺)
21
(360)
2.426
87 (99)
13 (<1)
0.4 (<1)
3/2⁺ (3/2⁺)
19
(5.02)
2.028
94.5 (100)
5.5 (<1)
5/2⁺ (5/2⁺)
425
(425)
1.273
100 (100)
3/2⁺ (3/2⁺)
370
(1140)
0.0
1/2⁺
^{29}Si

Figure 11. Branching Ratios and Lifetimes with BM model predictions for ^{29}Al. The BM model predictions are in brackets below the experimentally known values for the levels in ^{29}Al ordered by excitation energy (MeV). The lifetimes are in femtoseconds (fs = 10^{-15} sec). Deformation of 0.40 used.

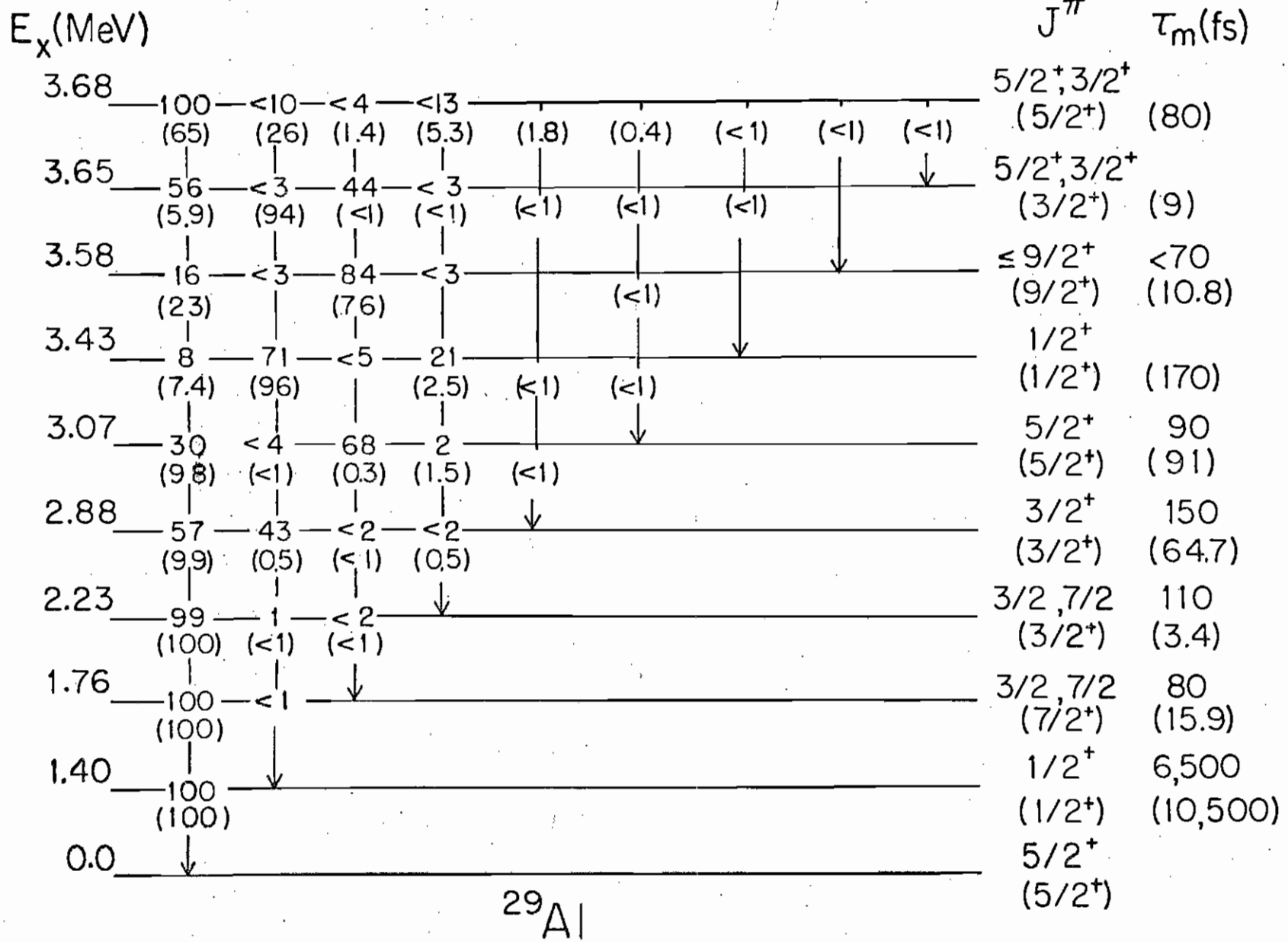
E_x(MeV)
J^π
τ_m(fs)
3.68
100 (65)
<10 (26)
<4 (1.4)
<13 (5.3)
(1.8)
(0.4)
(<1)
(<1)
(<1)
5/2+,3/2+ (5/2+)
(80)
3.65
56 (5.9)
<3 (94)
44 (<1)
<3 (<1)
(<1)
(<1)
(<1)
5/2+,3/2+ (3/2+)
(9)
3.58
16 (23)
<3
84 (76)
<3
(<1)
≤9/2+ (9/2+)
<70 (10.8)
3.43
8 (7.4)
71 (96)
<5
21 (2.5)
(<1)
(<1)
1/2+ (1/2+)
(170)
3.07
30 (9.8)
<4 (<1)
68 (0.3)
2 (1.5)
(<1)
5/2+ (5/2+)
90 (91)
2.88
57 (9.9)
43 (0.5)
<2 (<1)
<2 (0.5)
3/2+ (3/2+)
150 (64.7)
2.23
99 (100)
1 (<1)
<2 (<1)
3/2,7/2 (3/2+)
110 (3.4)
1.76
100 (100)
<1
3/2,7/2 (7/2+)
80 (15.9)
1.40
100 (100)
1/2+ (1/2+)
6,500 (10,500)
0.0
5/2+ (5/2+)
^{29}Al

branching ratios and lifetimes for ^{29}Si and ^{29}Al, respectively. The results for ^{29}Si are rather good, while the comparison for ^{29}Al is incomplete as this nucleus is not well known experimentally. The branching ratios show reasonable agreement in most cases. The most serious problem is that many of the calculated M1 strengths are not correct. This may be due to an inadequacy in describing the magnetic operator in a deformed field or that the bandmixed wave functions are not good. The predicted B(E2) rates are very encouraging. In general this calculation supports the bandmixing calculations made for each of these two nuclei, and gives added confidence to the wave functions.

C. Shell Model

The results of a shell model (SM) calculation by Wildenthal and McGrory[21] are shown on the left hand side of figures 8 and 9 for ^{29}Si and ^{29}Al, respectively. These predictions are quite reasonable for the energy levels and the spectroscopic pickup amplitudes for the modified surface delta interaction (MSDI) calculation were secured. The pickup amplitude for ^{29}Si and ^{29}Al are listed in table VI and VII, respectively. A comparison of the SM to BM amplitude shows that many are similar and that the phasing of prominent amplitudes agreed often. As in the BM case for ^{29}Si the identification of predicted energy levels was straightforward. For ^{29}Al some changes were made to compare with the BM case. The first $3/2^+$ and the first $7/2^+$ levels were assigned to the 2.23 MeV and 1.76 MeV levels corresponding with the assignments made for the bandmixing case. The 3rd instead of the 2nd $5/2^+$

calculated state was used for the 3.07 MeV level since its amplitudes were more appropriate.

Table VI. Pickup Spectroscopic Amplitudes from the shell model(MSDI) for ^{29}Si. See table II for a more complete description.

Energy in ^{29}Si (MeV) Exp(Cal)	Spin and Parity J^π	A_j for $0^+ \rightarrow J^\pi$ $j = J^\pi$	A_j for $2^+ \rightarrow J^\pi$ $j = 1/2$	$j = 3/2$	$j = 5/2$
0.000(0.00)	$1/2^+$	1.109		0.761	-0.253
2.028(1.80)	$5/2^+$	-1.658	0.279	0.047	0.235
1.273(1.96)	$3/2^+$	-0.516	0.755	-0.186	-0.056
2.426(2.82)	$3/2^+$	-0.114	0.141	0.092	0.407
3.069(3.61)	$5/2^+$	-0.041	0.132	0.029	-0.526
4.081(4.37)	$7/2^+$			0.161	0.669
4.896(4.43)	$5/2^+$	-0.746	-0.225	-0.036	-0.039
5.809(4.56)	$7/2^+$			-0.012	0.142
4.838(4.83)	$1/2^+$	0.326		0.076	0.201
4.742(5.11)	$9/2^+$				1.020
5.944(5.55)	$3/2^+$	-0.080	-0.180	0.004	0.378
(5.56)	$1/2^+$	0.171		-0.045	0.158
(5.97)	$7/2^+$			0.124	-0.205
5.649(6.33)	$9/2^+$				0.177

Table VII. Pickup Spectroscopic Amplitudes from the shell model(MSDI) for ^{29}Al. See table II for a more complete description.

Energy in ^{29}Al (MeV) Exp(Cal)	Spin and Parity J^π	A_j for $0^+ \rightarrow J^\pi$ $j = J^\pi$	A_j for $2^+ \rightarrow J^\pi$ $j = 1/2$	$j = 3/2$	$j = 5/2$
0.00(0.00)	$5/2^+$	2.435	0.050	0.023	-0.383
1.40(1.32)	$1/2^+$	-0.500		-0.100	-0.279
2.23(2.04)	$3/2^+$	0.065	-0.249	0.026	0.527
1.76(2.44)	$7/2^+$			-0.096	1.449
(3.28)	$5/2^+$	-0.420	0.302	-0.015	-0.422
3.07(3.50)	$5/2^+$	0.950	0.344	0.110	0.795
2.88(3.59)	$3/2^+$	-0.259	0.071	-0.029	0.867
(4.20)	$9/2^+$				1.170
(4.29)	$7/2^+$			-0.017	0.070
3.43(4.36)	$1/2^+$	0.245		0.032	0.510
(4.59)	$3/2^+$	0.115	0.035	0.036	0.110

Chapter V

EXPERIMENTAL RESULTS AND DATA ANALYSIS

A. $^{30}Si(d,d')^{30}Si$ Angular distributions

The angular distributions for the elastic and inelastic scattering of 23.0 MeV deuterons on ^{30}Si are shown in fig. 12. If the statistical error is not shown it is less than the size of the data point. The curves shown in fig. 12 were obtained from a coupled-channel calculation with the Karlsruhe version[52] of the T. Tamura[53] code JUPITOR. The necessary parameters are listed in table VIII, along with the optical model parameters that were determined first.

The nuclear structure of ^{30}Si appears deceptively simple with the 1d 5/2 shell closed and two neutrons filling the 2s 1/2 orbit. It appears, however, that the competition for filling the 2s 1/2 and 1d 3/2 shells is very complicated.[54] Shape equilibrium calculations using self-consistent methods[55] for mass 30 nuclei led to no sharply defined stable shape. A recent coupled-channel calculation for E_d = 10.0 MeV data for the ground state and first excited state present evidence for a prolate shape for ^{30}Si.[56]

Beginning with parameters for 21.1 MeV deuteron scattering from ^{24}Mg.[23] a search for optical model parameters for the present data was made with SNOOPT2.[57] Once these parameters were found, a search for the best fit for the ground state and first excited state was made with the Karlsruhe version of JUPITOR, this search automatically adjusted parameters to minimize χ^2 defined as

Figure 12. $^{30}Si(d, d')^{30}Si$ angular distributions for elastic scattering and inelastic scattering from the 2^+ state at 2.28 MeV. The solid line represents a coupled-channel optical model fit with parameters listed in table VIII.

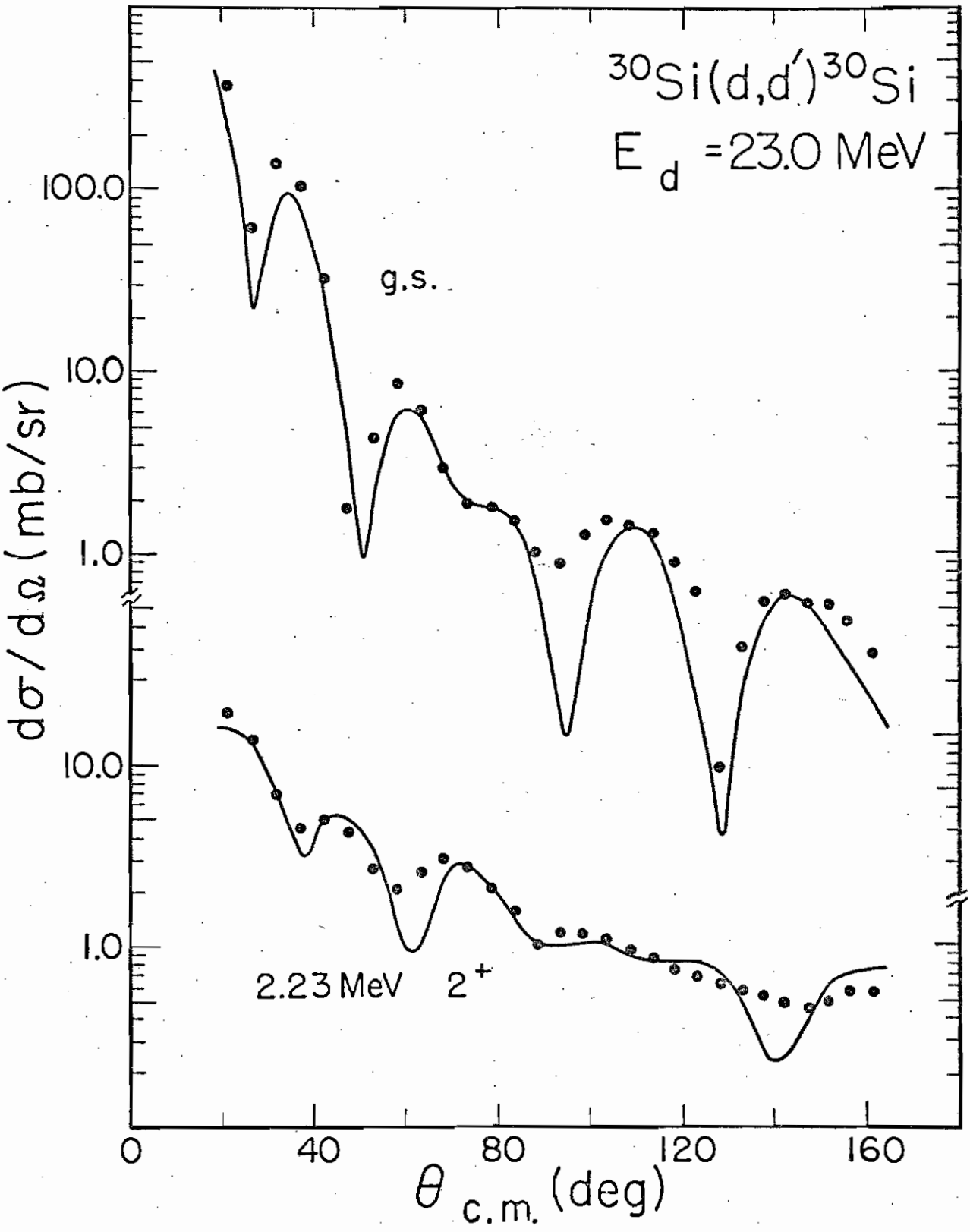
$^{30}Si(d,d')^{30}Si$
E_d = 23.0 MeV
g.s.
2.23 MeV 2+
100.0
10.0
1.0
10.0
1.0
dσ/dΩ (mb/sr)
0
40
80
120
160
θ c.m. (deg)

Table VIII. Optical Model Parameters [a]

Channel	E_{lab} (MeV)	β_2 [b]	V_0 (MeV)	r_0 (fm)	a_0 (fm)	W (MeV)	W_d (MeV)	r_w [c] (fm)	a_w [c] (fm)	r_c (fm)
$^{30}Si + d$	23.0		100.00	1.04	0.916		26.03	1.491	0.465	1.3
$^{30}Si + d$	23.0	0.32	98.74	1.04	0.800		13.00	1.530	0.540	1.3
$^{29}Si + {}^{3}He$ [d]	19.0		145.00	1.32	0.605	25.0		1.463	0.910	1.4
$^{29}Si + {}^{3}He$	19.0	-0.28	145.00	1.32	0.605	22.0		1.463	0.910	1.4

[a] As defined in eq. 1 ch. III.

[b] A non-zero value means the coupled-channel method was employed.

[c] $r_w = r_d$ and $a_w = a_d$ as in eq. 1 for this case.

[d] Same parameters used for the 15.0 MeV ^{3}He on ^{29}Si, except that $V_0 = 161.23$ MeV.

$$\chi^2 = \sum_{n,i} \left(\frac{\sigma_{exp}^{(n)}(\theta_i) - \sigma_{theory}^{(n)}(\theta_i)}{0.1\,\sigma_{exp}^{(n)}(\theta_i)} \right)^2$$

where n labels the nth state and θ_i the angles. Searches for prolate, oblate, and vibrational solutions were found. In fact, the prolate and vibrational solutions gave the lowest χ^2, with the oblate solution having the largest χ^2. To be consistent with a rotational picture the prolate solution was used with a β_2 of 0.32. The final fits were done by changing parameters to optimize the calculated results visually with no search. Proper alignment of the oscillations of the data to the calculated results were found to be important when used in a CCBA calculation. An indication of the importance of coupling this channel into the elastic scattering is shown by the decrease of 50 % of the imaginary surface strength.

The parameter set for the deformed potential was varied along a Vr^n ambiguity to optimize CCBA calculations for the single nucleon pickup reactions. The movement along the ambiguity had its greatest effect on the movement of the oscillations in relation to the center of mass angle for the s 1/2 differential cross sections.

B. $^{29}Si(^3He, ^3He)^{29}Si$ and $^{29}Si(^3He, ^3He')^{29}Si$

Angular Distributions and Analysis

The ^3He elastic and inelastic scattering was measured to determine the exit channel optical model potential. Figure 13 shows the ^3He elastic scattering from ^{29}Si at 15.0 and 19.0 MeV. The energies correspond approximately to the energies of the outgoing light particles in the (d, ^3He) and (d,t)

Figure 13. $^{29}Si(\,^{3}He,\,^{3}He\,)^{29}Si$ angular distributions. The solid lines are optical model fits. For each energy only a change in real well depth was needed and is shown by each curve. The same geometrical parameters were used listed in table VIII.

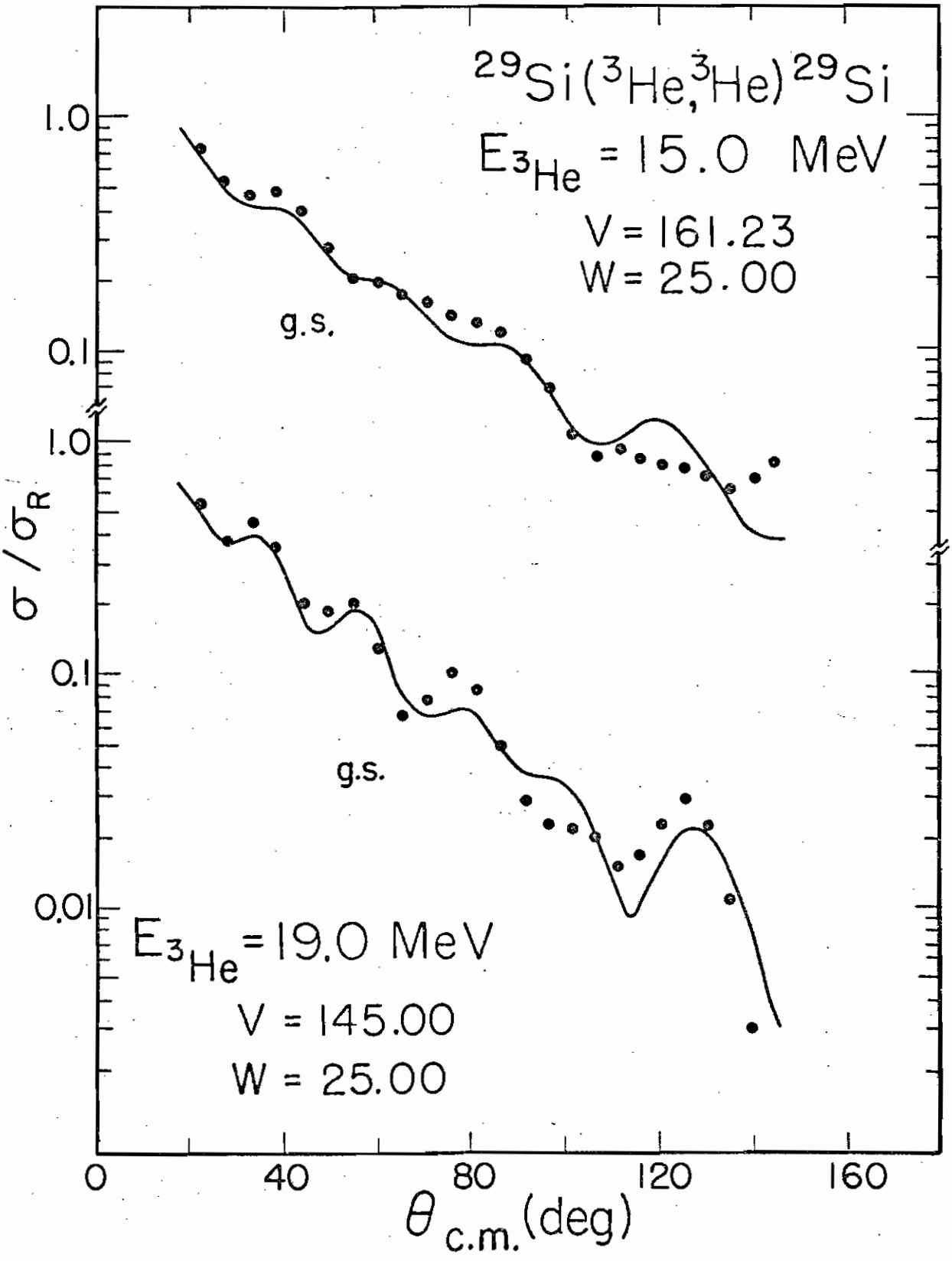
$^{29}Si(^{3}He,^{3}He)^{29}Si$
$E_{^{3}He}$ = 15.0 MeV
V = 161.23
W = 25.00
g.s.
g.s.
$E_{^{3}He}$ = 19.0 MeV
V = 145.00
W = 25.00
σ / σ_R
1.0
0.1
1.0
0.1
0.01
0
40
80
120
160
$\theta_{c.m.}$ (deg)

ground-state transitions, respectively. The statistical error is less than the error indicated by the size of a data point, unless shown.

The curves in fig. 13 represent an optical model fit with the parameters listed in Table VIII for the 19.0 MeV ^{3}He elastic scattering. For the 15.0 MeV ^{3}He data only the real potential strength needed to be changed and is listed in the upper right hand corner of fig. 13. The results were obtained by minimizing χ^2 with the search codes SNOOPT2[57] and JIB3.[58] The higher energy data was studied extensively due to the pronounced structure which is caused by the interference between the nuclear potential and the Coulomb potential. A search was made using the TUNL off-line DDP-224 computer with the code OPTICS.[59] For the latter code, the parameters are changed individually. The fit to the 15.0 MeV ^{3}He elastic scattering was also done this way after the parameters were determined for the higher energy data. The parameters used are similar to those of R. O. Nelson[23] and D. Dehnard et. al.[11] The results of R. W. Zurmuhle et. al.[60] were found to be unsatisfactory in describing the exit channel of the transfer reaction.

Figure 14 shows the ground-state rotational band of ^{29}Si interpreted from the bandmixing calculation Chapter IV and Pilt et. al.[13] and a coupled-channel calculation which is in good agreement. For an odd-A rotational nucleus the code JUPITOR[53] can only describe one rotational band. This is rather unfortunate for ^{29}Si since another band starts with the first excited state. Upon mixing, this state has a substantial admixture from the ground-state band. The ground state members are the ground-state $1/2^+$, the 2.028 MeV $5/2^+$ level and the 2.426 $3/2^+$ level. The data shown in fig. 14

Figure 14. $^{29}Si(\,^{3}He, ^{3}He')^{29}Si$ angular distributions. The ground state rotational band was analyzed for the 19.0 MeV incident ^{3}He beam energy. Solid curves represent the coupled-channel optical model for the ground state, 2.028 MeV state and 2.426 MeV state.

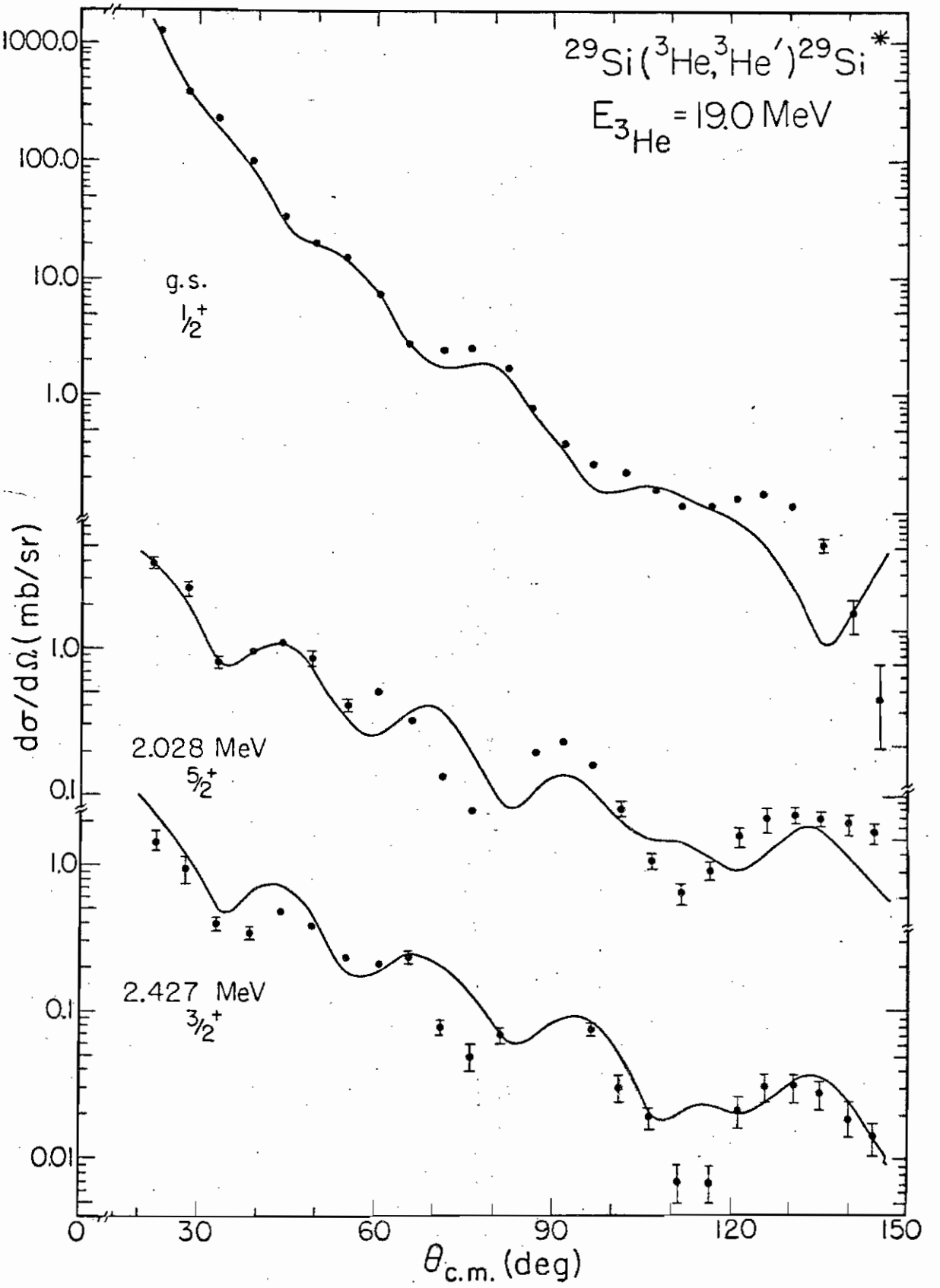
$^{29}Si(^{3}He,^{3}He')^{29}Si^{*}$
$E_{^{3}He}$ = 19.0 MeV
g.s.
1/2+
2.028 MeV
5/2+
2.427 MeV
3/2+
dσ/dΩ (mb/sr)
1000.0
100.0
10.0
1.0
1.0
0.1
1.0
0.1
0.01
0
30
60
90
120
150
θc.m. (deg)

are for these states respectively for a ^{3}He beam energy of 19.0 MeV. The search for a proper deformation parameter was made starting with the spherical optical model parameters. Since the inclusion of a coupling term explicitly removes flux from the beam, the imaginary strength needs to be reduced. A deformation parameter, β_2, between -0.26 and -0.30 was determined to give reasonable differential cross-section magnitudes for the two excited states. For the final fit the reduction of the imaginary volume term to 22.0 MeV and addition of a deformation strength of $\beta_2 = -0.28$ was basically the only change needed from the original spherical parameter set. The spin orbit term was not included due to the recent work of E. J. Ludwig et. al.[61] which showed that the ^{3}He polarization from ^{28}Si at 21 MeV was weak.

The most disturbing problem found in the coupled-channel analysis was that it was very hard to satisfy all the states in regard to the alignment of the diffraction patterns measured. Extensive parameter searches to resolve this were initiated, but in the end the original set was equally good. In doing this it is easier to understand the effect of coupled-channels. An observation to be noted is that the Blair phase rule[62] can be applied to inelastic ^{3}He scattering on an odd-A nucleus, which implies a strong quadrupole term is present even though the strength is split among several states.

Even though this is the wrong projectile on ^{29}Si, it is hoped that ^{3}He being a charge conjugate of a triton will not hamper the analysis. For transfer reactions the optical model wave functions have to describe the elastic scattering as well. For the ^{30}Si(d,t)^{29}Si reaction the 19.0 MeV ^{3}He optical

model parameters were adopted for the t + ^{29}Si outgoing waves and similarly for the ^{30}Si(d, ^{3}He)^{29}Al reaction the 15.0 MeV ^{3}He results were adopted for the ^{3}He + ^{29}Al channel. When a coupled-channel analysis was made for ^{29}Si, a large drop in absorption strength would be anticipated as in the deuteron inelastic analysis in ^{30}Si, but only a reduction of 12% was needed. The coupling for ^{29}Si is used later in discussing exit channel effects.

C. $^{30}Si(d,t)^{29}Si$ and $^{30}Si(d,{}^{3}He)^{29}Al$

Angular Distributions and Analysis

1. Experimental Results.

The results from the $^{30}Si(d,t)^{29}Si$ and $^{30}Si(d,{}^{3}He)^{29}Al$ measurements are shown in figs. 15-20 with calculated CCBA fits. The states which are well resolved have error bars that represent only the statistical error, if the error is less than the size of a data point it is not shown. In the analysis of the ^{29}Al spectra, the errors were doubled for the 2.23 MeV and 3.19 MeV states in figs. 19 and 20, respectively when subtracted spectra were used. In the ^{29}Si spectra near 4.8 MeV excitation energy there are four closely grouped peaks for the 4.742 MeV, 4.838 MeV, 4.896 MeV and 4.935 MeV states in ^{29}Si. The 4.935 MeV state is very weak and appears as a shoulder on the 4.896 MeV and 4.838 MeV doublet as shown in fig. 3. The 4.742 MeV state is close enough to the 4.838 MeV state that a Gaussian peak unfolding technique is necessary to determine the area of the peak in question. From nearby peaks an average width could be determined and a linear background could be fixed. By constraining the backgrounds and widths of the peaks and by fixing the peak separations (determined from kinematics) it was possible to unfold this quadruplet. Only a few points of the 4.935 MeV level could be extracted dependably and the angular distribution was not obtained. The doublet at 5.26 MeV was too weak to permit the use of Gaussian unfolding tecnhique, and only the sum was determined.

Figure 15. $^{30}Si(d,t)^{29}Si$ angular distributions for 0.0 MeV, 1.273 MeV, 2.028 MeV, and 2.426 MeV levels in ^{29}Si. The solid (dashed) curves are CCBA calculations with BM(SM) model amplitudes. Normalizations are to multiplied by 1.5 to get correct value for each model N, [N].

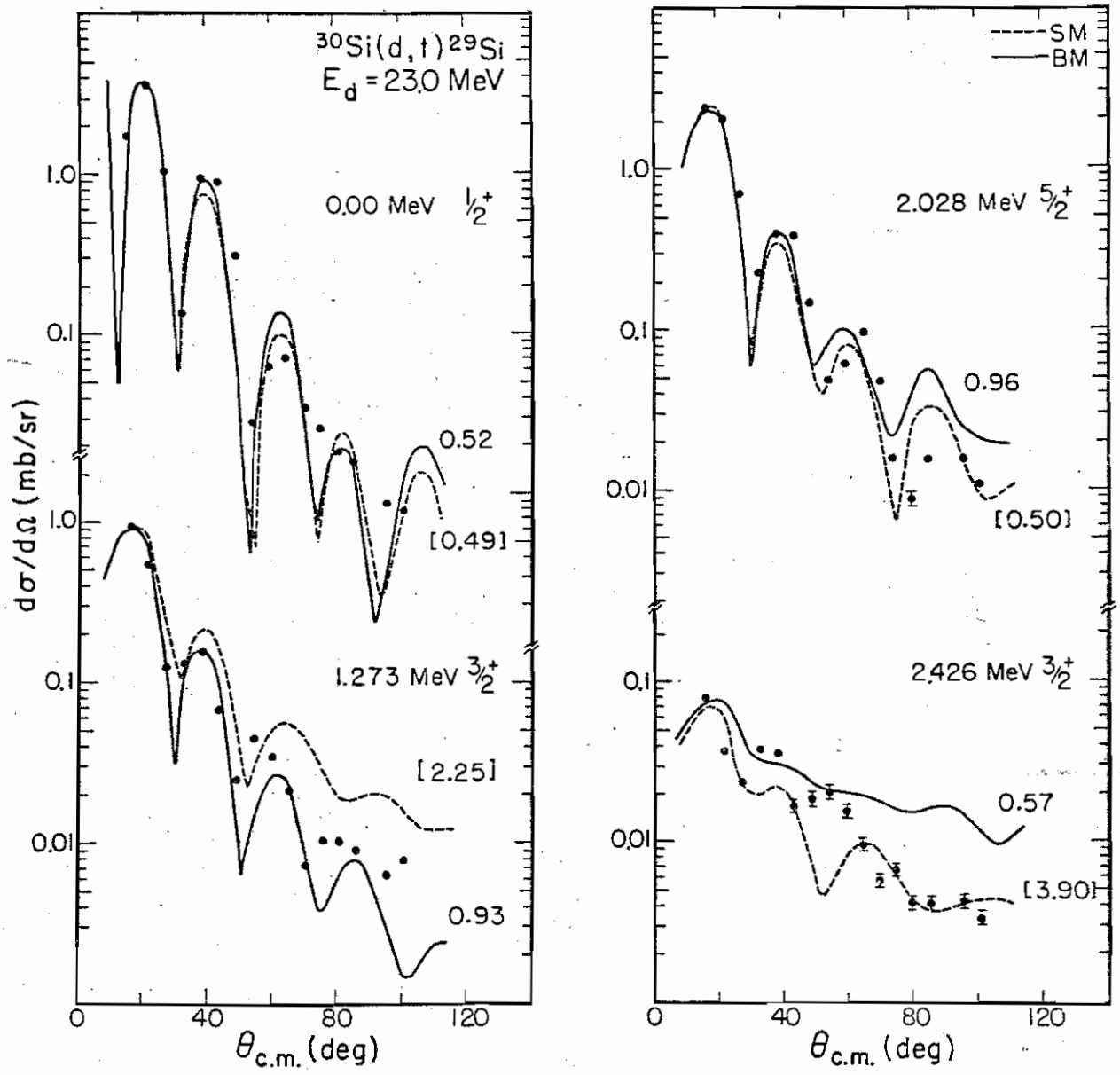
$^{30}Si(d,t)^{29}Si$
$E_d = 23.0$ MeV
0.00 MeV $1/2^+$
0.52
[0.49]
1.273 MeV $3/2^+$
[2.25]
0.93
$d\sigma/d\Omega$ (mb/sr)
$\theta_{c.m.}$ (deg)
SM
BM
2.028 MeV $5/2^+$
0.96
[0.50]
2.426 MeV $3/2^+$
0.57
[3.90]

Figure 16. $^{30}Si(d,t)^{29}Si$ angular distributions for 3.069 MeV, 4.081 MeV, 4.742 MeV, 4.838 MeV, and 4.896 MeV levels. Solid (dashed) curves are CCBA calculations for BM(SM) model with normalization N([N]). Normalization N([N]) for each case needs to be multiplied by 1.5.

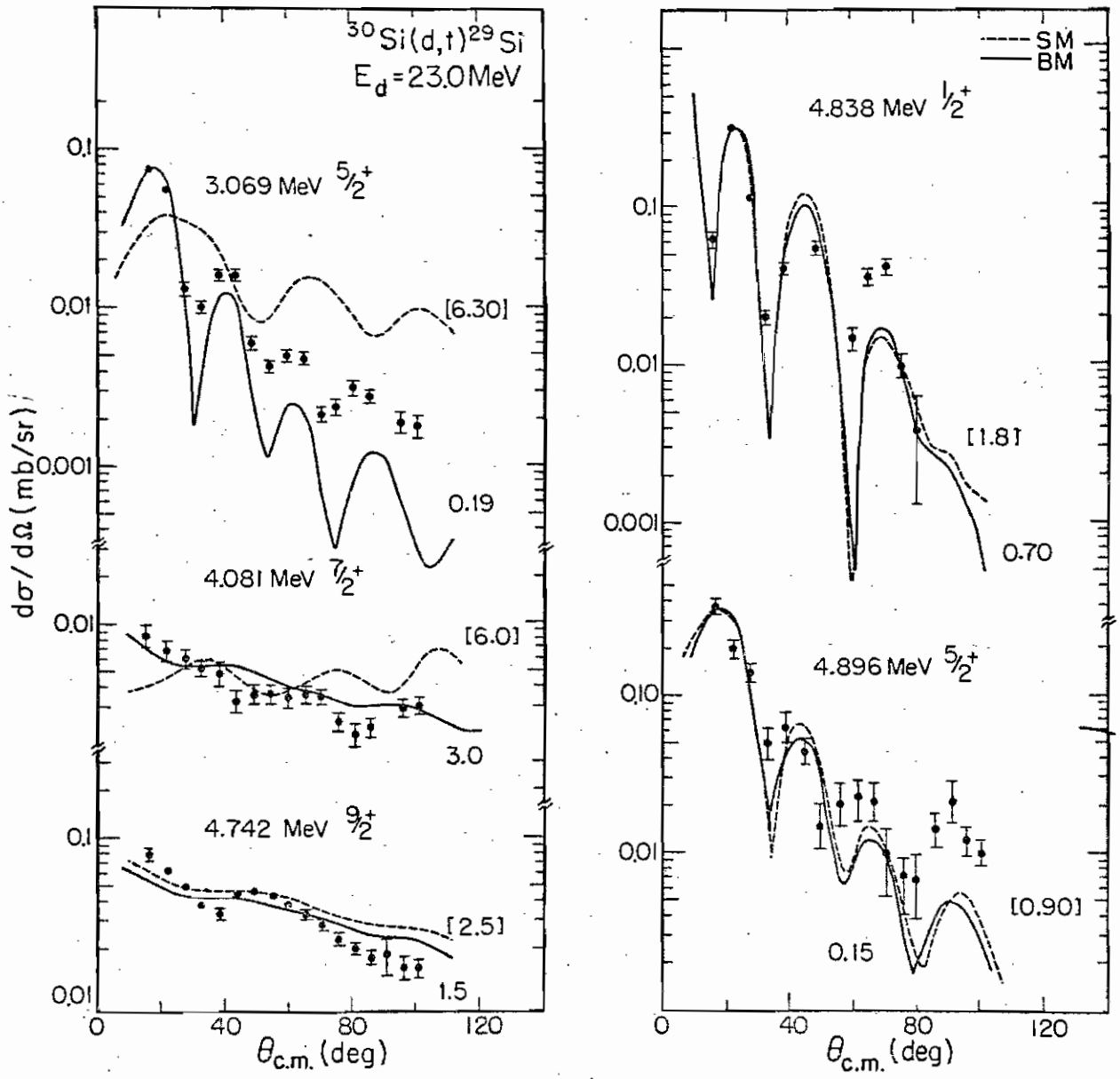
^{30}Si(d,t)^{29}Si
E_d=23.0MeV
3.069 MeV 5/2+
[6.30]
0.19
4.081 MeV 7/2+
[6.0]
3.0
4.742 MeV 9/2+
[2.5]
1.5
dσ/dΩ (mb/sr)
θc.m. (deg)
SM
BM
4.838 MeV 1/2+
[1.8]
0.70
4.896 MeV 5/2+
[0.90]
0.15

Figure 17. $^{30}Si(d,t)^{29}Si$ angular distributions for sum of 5.249 MeV and 3.279 MeV, 5.649 MeV, 5.809 MeV, 5.944 MeV, 6.104 MeV, and 8.34 MeV levels. Solid (dashed) curves are CCBA calculations for BM(SM) model with normalization N([N]). Normalization N([N]) for each case needs to be multiplied by 1.5.

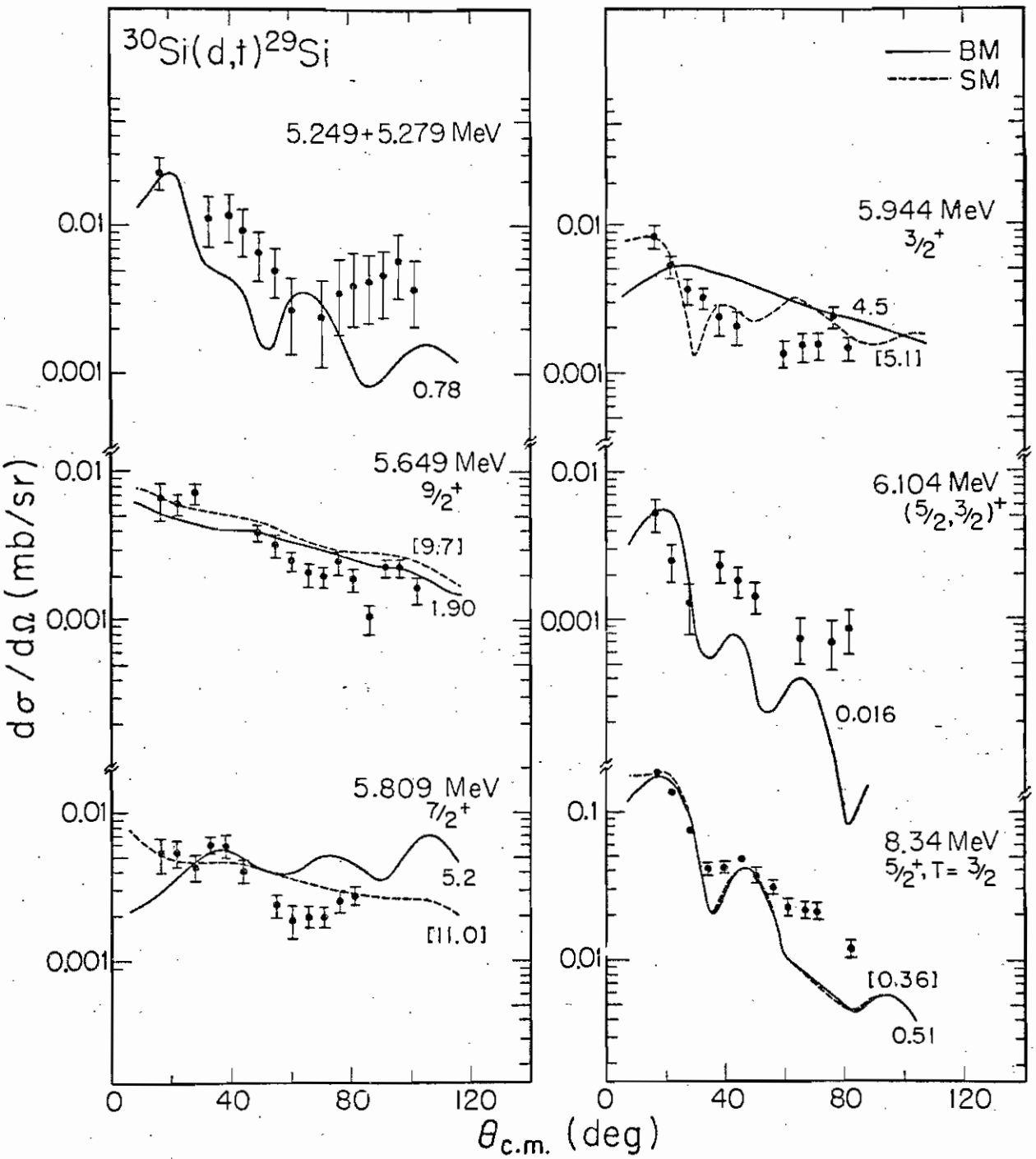
$^{30}Si(d,t)^{29}Si$
5.249+5.279 MeV
0.78
5.649 MeV
$9/2^+$
[9.7]
1.90
5.809 MeV
$7/2^+$
5.2
[11.0]
BM
SM
5.944 MeV
$3/2^+$
4.5
[5.1]
6.104 MeV
$(5/2,3/2)^+$
0.016
8.34 MeV
$5/2^+, T=3/2$
[0.36]
0.51
$d\sigma/d\Omega$ (mb/sr)
$\theta_{c.m.}$ (deg)

Figure 18. $^{30}Si(d,t)^{29}Si$ angular distributions for negative parity states at 3.623 MeV and 6.195 MeV excitation energy. BM model CCBA calculation presented for the 3.623 MeV $7/2^-$ level is the solid curve. The dashed curve is an adjusted fit.

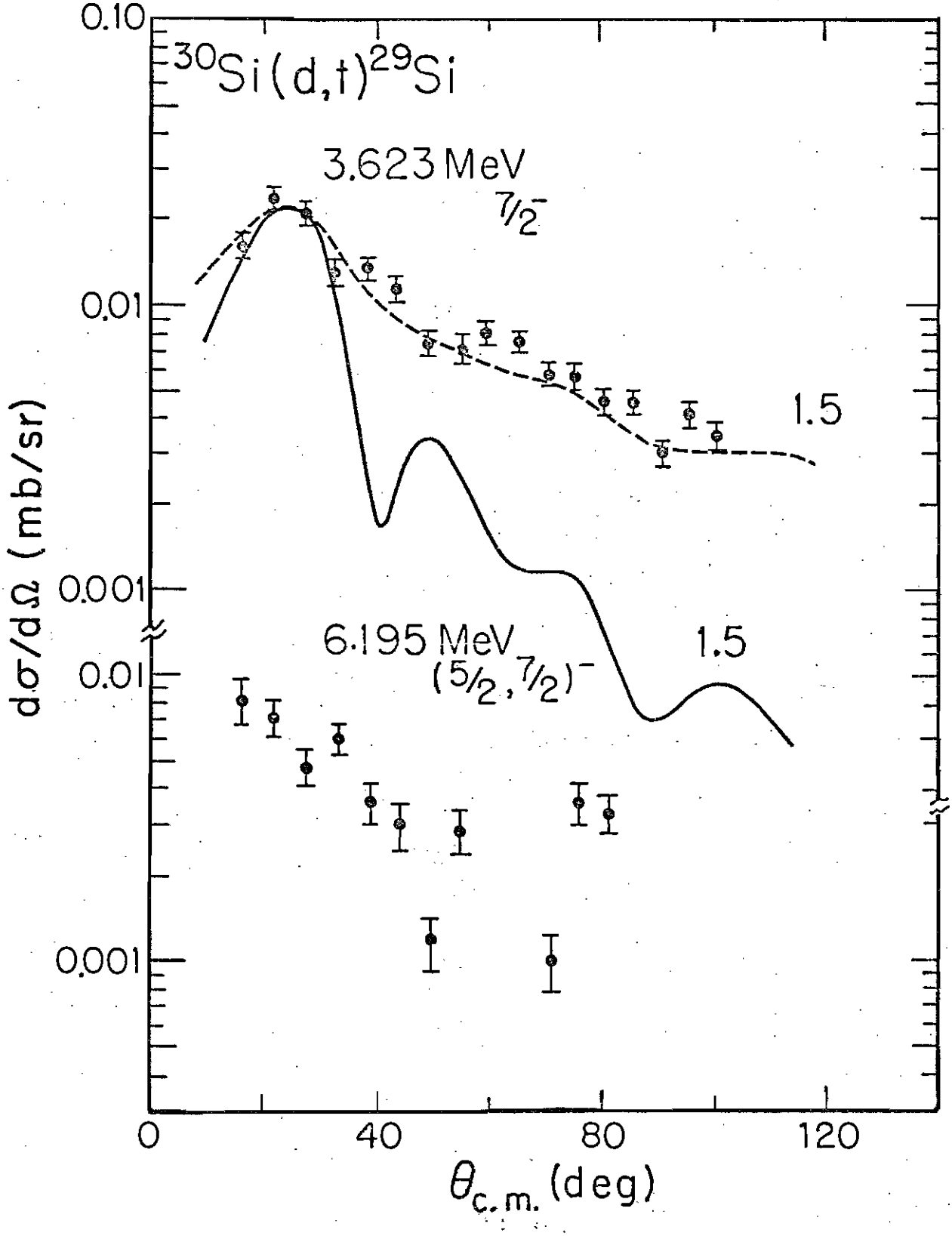
$^{30}Si(d,t)^{29}Si$
3.623 MeV
$7/2^-$
1.5
6.195 MeV
$(5/2, 7/2)^-$
1.5
0.10
0.01
0.001
0.01
0.001
$d\sigma/d\Omega$ (mb/sr)
0
40
80
120
$\theta_{c.m.}$ (deg)

Figure 19. $^{30}Si(d, {}^{3}He)^{29}Al$ angular distribution for first six levels in ^{29}Al and the 3.43 MeV $1/2^{+}$ state. Solid (dashed) curves are CCBA calculations for the BM(SM) model with normalization N([N]).

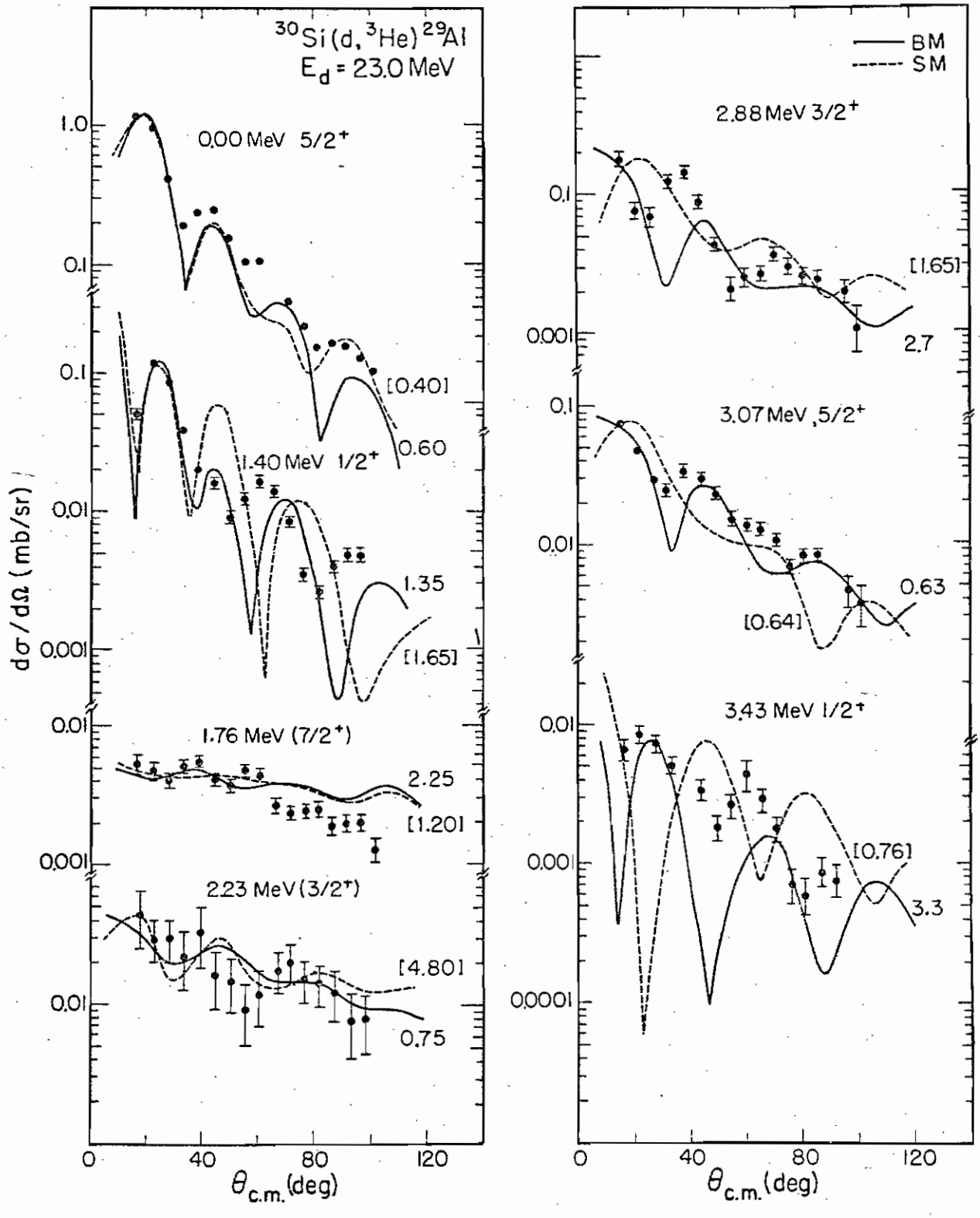
^{30}Si(d, ^{3}He)^{29}Al
E_d = 23.0 MeV
0.00 MeV 5/2+
[0.40]
0.60
1.40 MeV 1/2+
1.35
[1.65]
1.76 MeV (7/2+)
2.25
[1.20]
2.23 MeV (3/2+)
[4.80]
0.75
dσ/dΩ (mb/sr)
θc.m. (deg)
BM
SM
2.88 MeV 3/2+
[1.65]
2.7
3.07 MeV, 5/2+
0.63
[0.64]
3.43 MeV 1/2+
[0.76]
3.3
θc.m. (deg)

Figure 20. $^{30}Si(d, ^{3}He)^{29}Al$ angular distribution for 3.19 MeV state. Calculated curves all use BM model amplitudes with normalization N. The three curves represent three possible J^{π} assignments. The two solid curve for $9/2^{+}$ and $3/2^{-}$ and dashed curve for $3/2^{+}$.

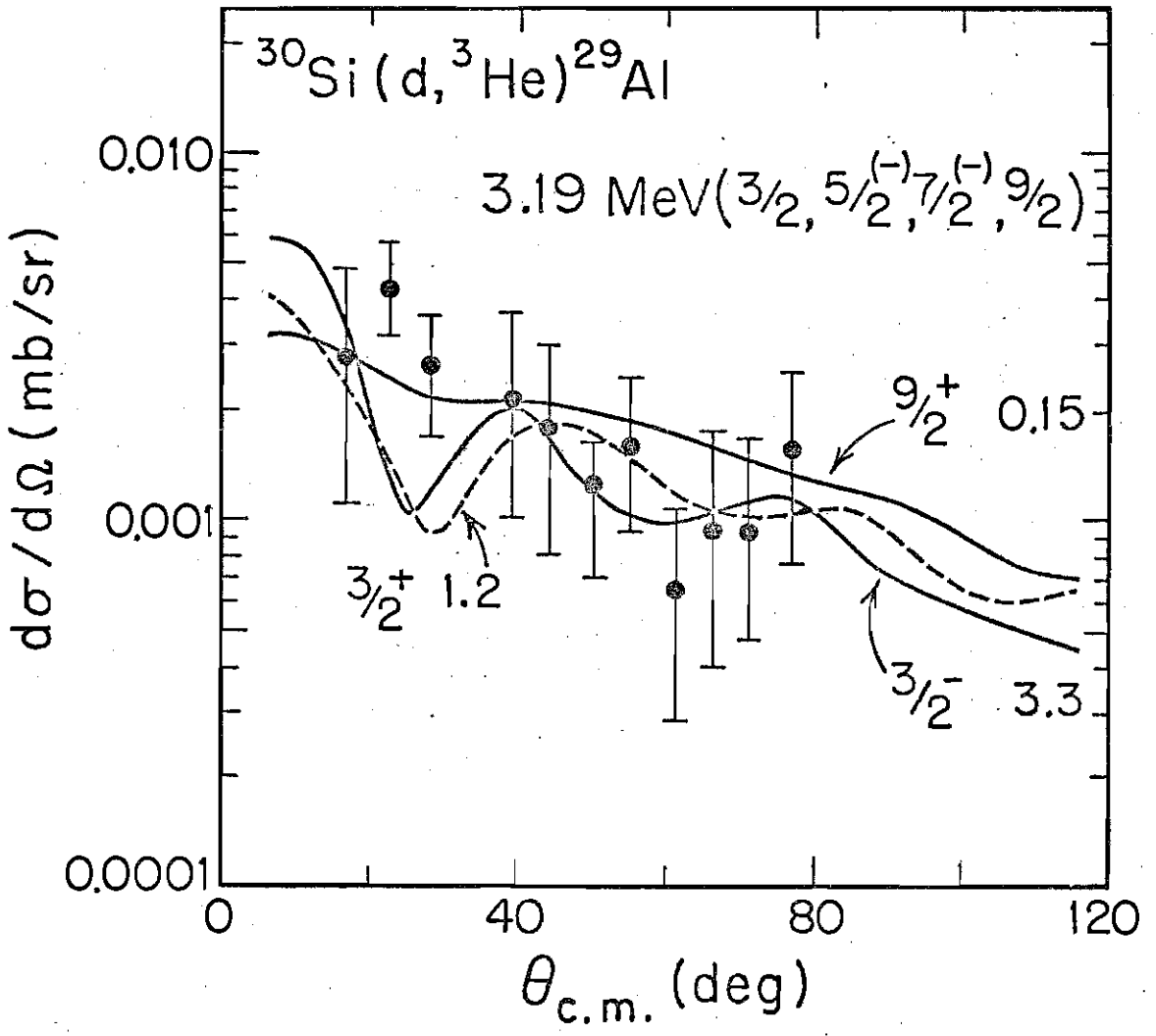
^{30}Si(d,^{3}He)^{29}Al
3.19 MeV(3/2, 5/2$^{(-)}$, 7/2$^{(-)}$, 9/2)
9/2^{+} 0.15
3/2^{+} 1.2
3/2^{-} 3.3
0.010
0.001
0.0001
0
40
80
120
dσ/dΩ (mb/sr)
θ$_{c.m.}$ (deg)

The absolute normalization of the angular distributions was determined from the solid angle, beam integration and target thickness measurements and is believed to be accurate within 10%. The angular distributions are grouped in order of excitation energy and parity in figs. 15-18 for ^{29}Si and in figs. 19 and 20 for ^{29}Al.

2. CCBA Analysis

As discussed in Ch. III, the CCBA method is more likely to provide a complete description of the transfer of a nucleon than a DWBA calculation whenever the nuclei exhibit strong collective behavior. By allowing scattering to excited states of the target and residual nucleus induced by the projectiles in the incident and the exit channels, multi-step processes can be treated that were ignored in DWBA. In an even-even collective nucleus the low-lying 2^+ excited state is the most important to consider since it usually takes a lot of strength out of the beam. The first excited 2^+ state is described within the coupled-channel framework discussed in Ch. III. The transferred nucleon in a pickup reaction therefore can be removed from the target nucleus in two ways, as in DWBA from the 0^+ ground state or from the 2^+ excited state. Besides the normal J^π transfer from the 0^+ state, other angular momentum transfers from the 2^+ state become possible. A $J^\pi = 5/2^+$ transfer can from the excited 2^+ state have transfers with d 5/2, d 3/2 or s 1/2 form factors. This excited 2^+ target allows lower angular momentum transfers to $7/2^+$ or $9/2^+$ states that are normally "j-forbidden" in the 2s - 1d shell. For example, a $9/2^+$ state can be populated by a d 5/2 transfer from the 2^+ state in the

target. This process is certainly more favored than a g 9/2 transfer from the 0^+ ground state. Since the direct and indirect amplitudes add coherently they are part of the input for a CCBA calculation. In this way the direct spectroscopic factors are tested along with the indirect terms. If the model wave functions are correct the normalization of the fit to the data should be unity.

The models tested are the rotational model with bandmixing (BM) and the shell-model (SM). The spectroscopic amplitudes used are listed in tables II and IV for BM, and tables VI and VII for SM.

One of the more noticeable features of an indirect transfer is that the results tend to be isotropic especially at the back angles. This is in part due to the fact that the 2^+ angular distribution is not as forward peaked as in the elastic scattering and that the summing of different j-transfers tends to produce isotropic angular distributions. Nearly isotropic angular distributions are seen for the $7/2^+$ and $9/2^+$ states and can be explained as having a weak direct strength in comparison to transfer from the excited 2^+ state. Besides these high spin states some states with $J^\pi = 1/2^+$, $3/2^+$ and $5/2^+$ with small direct terms become quite isotropic in the back angles. The CCBA method of including multi step effects help in some cases to understand these non-pickup (non-direct) angular distributions.

The form factors used for the CCBA calculation were computed in a real Woods-Saxon potential as defined in Ch. III (eq. 1) and with a radius $r = 1.25$ fm, diffuseness $a = 0.65$ fm, a spin-orbit term of the Thomas type with a strength $\lambda = 25.0$, and a well depth adjusted to give the correct

separation energy for the bound particle at the proper excitation energy of ^{29}Si or ^{29}Al. The separation energies for inelastic processes should be decreased by the inelastic excitation energy relative to that required by the competing direct transition. After tests proved the difference was small, the separation energy was set equal to direct value. The g 7/2 and g 9/2 form factors were determined this way even though the real well strength needed to bind them was larger than is realistic for this mass region.

A more serious problem is the use of spherical form factors for a deformed nucleus. Rost[40] has investigated this problem and has found that the difference is small when the more realistic deformed potential radial wave functions were employed.

The optical model parameters for the incident and exit channels were selected through an extensive analysis. The coupled-channel potentials produced incident and exit channel wave functions that would satisfactorily describe the transfer of a nucleon in a CCBA calculation and fit the incident and exit elastic and inelastic data. One of the most outstanding virtues of a CCBA analysis is its ability to use realistic potentials.

The spectroscopic amplitudes from the theoretical models do not have the needed isospin factor. A Clebsch-Gordon factor (C^2) is needed to normalize the whole CCBA calculation. This factor is dependent on the isospin quantum numbers of the initial nucleus, the nucleon and the residual nucleus. The isospin of the initial target nucleus is added to the "annihilated" nucleon to form the isospin of the residual nucleus. For a pickup reaction the nucleon is being "annihilated" from the target nucleus, therefore the isospin projection

of the nucleon is negated. Thus a neutron with $t = 1/2$, $t_3 = 1/2$ is changed to $t = 1/2$, $t_3 = -1/2$ when picked up by the incoming projectile, producing a more proton rich nucleus. Therefore in a (d, t) reaction on a $T = 0$ nucleus the C^2 is unity and on a $T = 1$, $T_3 = 1$ nucleus the C^2 is two thirds as is the case for ^{30}Si. For the ^{30}Si(d, ^{3}He) reaction the C^2 is unity. The suitable C^2 factors were used in the final normalizations.

A diagrammatical way of picturing the possible transitions in a CCBA calculation is illustrated in fig. 21. The initial target nucleus is described as a rotor with a 0^+ ground state and an excited 2^+ state coupled by a quadrupole term with strength β_2. Since scattering wave functions are needed these states are solved in a coupled-channel optical model described in Ch. III. The final residual nucleus is an odd-A rotor with a ground state band consisting of j_1, j_2 and j_3 members coupled with a β'_2. The scattering wave functions are again found in a suitable potential. The state j_1 marked as the final state is the ground state and in a normal scattering of the residual projectile has incoming and outgoing wave functions, but for a transfer reaction all the states from the final nucleus have only outgoing wave functions. The arrows joined with a kinky line between states represents the coupling that mixes the rotational wave functions. Now the simple direct (D) transfer is marked as line 1. The final state can also be populated by the incident (I) projectile exciting the target nucleus to the excited 2^+ state and the transfer goes as the line marked with 4. The incident transition (line 4) implies other angular momentum transfers than j_1 are possible and should be included. If the ground state were $1/2^+$ then transfers of d 3/2 and d 5/2 from the 2^+

Figure 21. Schematic representation of the transitions that can be considered for multistep processes. The initial and final nuclei can be coupled. A direct (D) transition is from the ground state of initial nucleus. An incident (I) transition is from the excited 2^+ state of the initial nucleus. The exit (E) transition is when final nucleus is coupled and these other levels contribute to the final state. The total(T) transition is the sum of the three effects. The various lines schematically show the various ways the final state can be populated.

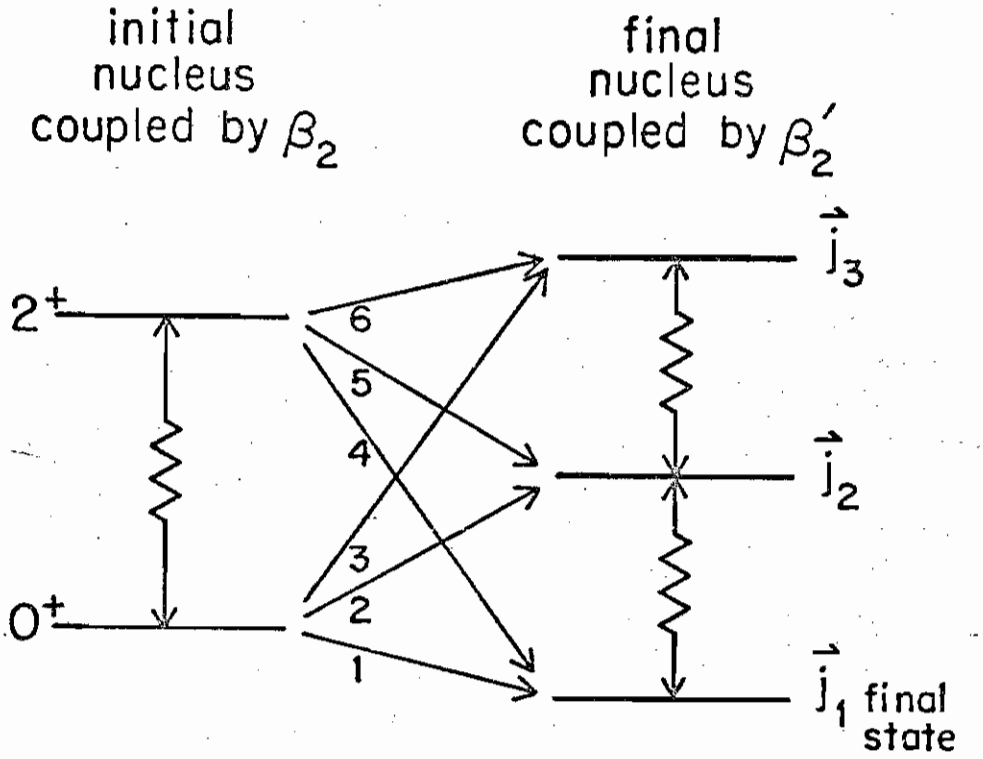

TRANSITION

Direct	D	1
Incident	I	4
Exit	E	2,3,5,6
Total	T	Σ all possible

state are possible. The exit (E) channel is defined as all the possible ways that the j_1 final state can be populated through the coupled residual rotational band. The final state is affected by the inclusion of these other levels that are populated by direct and indirect reactions themselves, but do not remain neutral due to the coupling. Splitting up each effect in this way reveals the strength of each component on the differential cross-section. Since a coherent sum of amplitudes is made for T, the total calculation is the most relevant since it tests everything including the wave functions for other states as well.

3. Multistep Processes in the Incident Channel Only.

From the investigation of the entrance and exit channels in sections A and B, the target nucleus has a strongly excited 2^+ state that should not be neglected. The calculations to follow are done with only this channel added. By not coupling the final residual nucleus only the direct (D) and incident (I) transitions of fig. 21 are tested. The curves shown in figs. 15-20 are CCBA calculations that are nuclear model dependent. The solid curves use the rotational model with bandmixing (BM) amplitudes listed in table II for ^{29}Si and table IV for ^{29}Al in figs. 15-17, 19. The CCBA calculations were normalized to the experimentally measured angular distributions, for the BM CCBA calculations the normalization, N, has no brackets. The dashed curves in figs. 15-17, 19 are CCBA calculations with the shell model (SM) amplitudes listed in table VI for ^{29}Si and table VII for ^{29}Al with normalizations in brackets [N].

The calculated results shown in fig. 15 agree in shape for most of the levels. The 2.426 MeV $3/2^+$ level is disturbing since both models have problems. The solid (BM) curve seems to have too much indirect amplitude as shown by too much differential cross section in the back angles. The dashed (SM) curve looks better but has a large normalization of 5.9. This level is the first in ^{29}Si to display a need for an indirect component to describe it. Often in a DWBA analysis such a state would be described as non-pickup (non-direct) and ignored. The other levels in this figure are of a direct nature.

Two high spin states of $7/2^+$ and $9/2^+$ are presented in fig. 16 as are the positive parity states below 5.0 MeV excitation in ^{29}Si. The typical unpronounced structure of these high spin states are shown for the 4.081 MeV $7/2^+$ and the 4.742 MeV $9/2^+$ levels, but the angular distributions seem to reflect the possible need of some direct contribution. The normalizations for these levels are above unity for each nuclear model implying a too small spectroscopic amplitude. The 3.069 MeV $5/2^+$ level shows where the SM amplitudes are obviously wrong, as well as the fact that the BM smplitudes for this level have too much direct strength as seen by the normalization of 0.29. Similarly the 4.896 MeV $5/2^+$ level has too much indirect strength for the BM curve. Both model results for the 4.838 MeV $1/2^+$ level are good but the normalization for the BM case of 1.05 is better.

Fig. 17 shows the angular distributions analyzed for ^{29}Si above 5.0 MeV excitation energy. The sum of the 5.249 MeV and 5.279 MeV states shows more structure than would be expected for high spin states. Since the 5.279 MeV level is either a $7/2^+$ or $3/2^+$ and the 5.249 MeV level is identified as a $9/2^-$, a CCBA calculation was attempted for $J = 3/2^+$ with a set of BM amplitudes for a level closeby in energy. The next three levels have CCBA calculations with spectroscopic amplitudes selected from levels of each nuclear model. The 6.104 MeV $(5/2, 3/2)^+$ level was assigned $J = 5/2^+$, but having a normalization of 0.024 the spectroscopic amplitudes are wrong as could be the spin parity assignment. The CCBA calculations for the 8.34 MeV $5/2^+$, $t = 3/2$ level are in very good agreement.

Fig. 19 presents the main work done for the $^{30}Si(d, ^{3}He)^{29}Al$ reaction. Generally the SM calculations are in poorer agreement to the BM results. An interesting example of how a CCBA calculation tests amplitudes is shown for the 3.07 MeV $5/2^+$ level. The normalizations for both curves are about the same but the solid curve is in better agreement with the data. The main difference is in the phase of the indirect $d_{5/2}$ transfer. The 2.88 MeV $3/2^+$ level shows the same problem but is not as simple as the previous case. The 3.43 MeV $1/2^+$ level is poor in shape for the SM dashed curve but has good normalization. The BM solid curve probably lacks direct and indirect strength. The 2.23 MeV state was assigned for this study as $3/2^+$ and has too high a normalization for the dashed SM curve.

Fig. 18 shows the negative parity states analyzed for the $^{30}Si(d, t)^{29}Si$ reaction. The CCBA calculations were done with the BM model. The solid curve was calculated with amplitudes assuming that the 3.623 MeV $7/2^+$ level is the $(303)\ K^{\pi} = 7/2^-$ bandhead. This fit does not have enough indirect amplitude. The dashed curve was done with the amplitudes changed to $0.77A_{7/2}$-(D) and $3.94A_{7/2}$-(I) to agree with the data. Possibly mixing other bands is needed to increase the indirect strength. No fit is presented for the 6.195 MeV level.

Fig. 20 shows the weakly populated 3.19 MeV level in ^{29}Al whose spin and parity are not well known. Goosman et. al.[8] have argued that this level has $J^{\pi} = 3/2^+$ or $5/2^+$ based on the β-decay of ^{29}Mg which had a large decay to this particular level. The rotational model with bandmixing (BM) calculations show a $9/2^+$ level closeby in energy. A single band calculation

with the $(330)K^{\pi} = 1/2^-$ orbit no. 14 with a reasonable bandhead has as its lowest energy member a $3/2^-$ level. The curves in fig. 20 are CCBA calculations for these three possibilities. The dashed curve uses the third $3/2^+$ state predicted in the BM model. The two solid curves are calculated with $9/2^+$ and $3/2^-$ amplitudes. Each curve does represent the data with the $3/2^+$ dashed curve being the best in normalization.

A simple way of comparing the two models can be done by ignoring the shape problems and investigating the normalizations. An average of the normalizations is made and then the root mean square is determined. For ^{29}Si the average was done over the first nine positive parity levels. The BM results yielded an average of 1.43 ± 1.22 and the SM results had 4.09 ± 3.13. The average for the BM model is closer to unity and has a smaller deviation from the average than the SM model.

For ^{29}Al the first six levels and the 3.43 MeV $1/2^+$ level were used in the averaging. The BM average was 1.65 ± 1.01 and the SM average was 1.59 ± 1.38. Both models have approximately the same average with deviation from the average slightly better for the BM model than the SM model.

As mentioned in the CCBA analysis section, the direct and indirect spectroscopic amplitudes add coherently. An estimate of the direct spectroscopic factor can be made, since the CCBA calculations were normalized to the forward angle data when possible. With the CCBA calculations model dependent, the BM model was chosen to be tabulated since it is overall a better description for the ^{29}Si and ^{29}Al nuclei. Tables IX and X for ^{29}Si and ^{29}Al

Table IX. Spectroscopic Results for the $^{30}Si(d,t)^{29}Si$ Reaction

Energy in ^{29}Si (MeV)	Spin and Parity I^{π}	CCBA C^2S_d (a)	CCBA C^2S_t (b)	CCBA ind/dir (c)	DWBA $C^2S(d,t)$ (d)	DWBA $C^2S(p,d)$ (e)	DWBA $C^2S(d,p)$ (f)
0.000	$1/2^+$	0.62	0.68	0.08	0.8	0.68	0.83
1.273	$3/2^+$	0.59	0.79	0.36	0.7	0.70	1.05
2.028	$5/2^+$	1.35	1.93	0.44	1.7	1.77	0.27
2.426	$3/2^+$	0.003	0.24	69.1	0.17	0.13	
3.069	$5/2^+$	0.010	0.014	0.40	0.10	0.08	0.11
3.623	$7/2^-$	0.010	0.015	0.50	0.08	0.17	0.68
4.838	$1/2^+$	1.023	2.00	0.95			0.04
4.896	$5/2^+$	0.49	0.55	0.14	1.0	1.19	
8.34	$5/2^+$ t=3/2	2.3	2.5	0.05	2.0	1.66	

[a] Present study. $S_d = NA_j^2$ where N is the additional normalization factor indicated for each curve in figs. 15-20. The A_j are direct BM amplitudes from Table II.

[b] Present study. $S_t = N\sum A_j^2$, sum of all amplitudes for a given level.

[c] Present study. The ind/dir is the ratio of indirect to direct spectroscopic factors.

[d] Ref. 11 (E_d = 21 MeV)

[e] Ref. 12 (E_p = 27.3 MeV)

[f] Ref. 14

Table X. Spectroscopic Results for the $^{30}Si(d, ^{3}He)^{29}Al$ Reaction

Energy in ^{29}Al (MeV)	Spin and Parity I^{π}	CCBA C^2S_d (a)	CCBA C^2S_t (b)	CCBA ind/dir (c)	DWBA $C^2S(t, ^{4}He)$ (d)	DWBA $C^2S(d, ^{3}He)$ (e)
0.00	$5/2^+$	2.59	2.72	0.05	3.26	5.6
1.40	$1/2^+$	0.30	0.31	0.04	0.81	0.8
2.23	$(3/2^+)$	0.014	0.57	42.00	0.05	
2.88	$3/2^+$	0.19	0.31	0.57	0.32	
3.07	$(5/2^+)$	0.64	1.12	0.75	1.32	
3.43	$1/2^+$	0.05	0.09	0.63	0.11	

a, b, c Present study, as defined in Table IX.

d Ref. 4

e Ref. 5

respectively, summarize the results of this study under CCBA, and under DWBA are previously measured spectroscopic factors. The C^2S_d is the direct (D) spectroscopic factor determined with $S_d = NA_j^2$ (D), where N is the appropriate normalization factor. Similarly the indirect amplitudes were squared and added to S_d to get the total, S_t. Finally an estimate of the indirect strength is given as the ratio of the sum of the squares of the indirect amplitudes to the direct amplitude squared. The J^π assignments in brackets are listed that were selected for levels to facilitate this study. In many cases where the indirect term is weak the same direct factor is extracted within reasonable agreement. From comparing these results for individual levels the amount of multistep strength is seen to affect the direct factor measured in a simple DWBA analysis. The 2.426 MeV $3/2^+$ level has a large ratio of indirect to direct strength, yet the total CCBA factor is comparable to that measured by the DWBA method. The DWBA analysis is not capable of estimating the indirect strength properly, therefore if a state does have a large indirect components they are just added into the DWBA spectroscopic factor. In a CCBA analysis the direct components are separated, therefore it is possible to extract better factors since the indirect components can be estimated.

The work of Ascuitto and Glendenning[63] on the (p,t) reactions has shown that multistep processes are important with the additional terms affecting the direct spectroscopic factor. In the ^{20}Ne(d, ^{3}He)^{19}F reaction studied by Ellis and Dudek[64], they concluded that multistep processes were important and possibly could alter the spectroscopic factors extracted even when normalizing to the forward angle data.

The application of the sum rules for the CCBA spectroscopic results for ^{29}Si from table IX yields for the positive parity states $C^2S_d = 6.4$ and $C^2S_t = 7.7$ where the shell model limit is $C^2S = 8$. A sum of the DWBA $C^2S(d,t) = 6.3$ from ref. 11, which is in good agreement with the CCBA sum of C^2S_d factors. The strong $t = 3/2$ 8.34 MeV $5/2^+$ level was included in these sums. For ^{29}Al table X was used to determine the sums with $C^2S_d = 3.8$ and $C^2S_t = 5.1$ where the shell model limit is $C^2S = 6$. The DWBA sum of ref. 4 was $C^2S(t, {}^4He) = 5.85$ which practically exhausts the shell model limit. The CCBA results suggested the need for more strength which could be in some unobserved higher excited states.

This analysis has not included the spin-orbit term in the deuteron optical model potential in order to simplify by using less parameters. The need for this term was not warranted in the coupled-channel description of the incident deuteron data. Compound nucleus formation was assumed to be small, with an excitation energy of the compound system at 36 MeV. Some of the weak transfer cross sections probably can be described as compound nuclear decay of a triton or ^{3}He. This statistical approach clouds the fact that a simple multistep process can explain the same thing as a slightly higher order direct process.

4. Multistep Processes in Incident and Exit Channels

The exit channel for the $^{30}Si(d,t)^{29}Si$ reaction did not display a great change in the imaginary strength of the optical model (see table VIII) for the inelastic ^{3}He scattering. Many more channels of similar strength are open, but coupling the exit channel should provide a better description. One severe restriction in the current codes is that only a ground state band can be calculated for an odd-A rotational nucleus.[53] This restricts the coupled exit channel in ^{29}Si to the ground state members which are the 0.000 MeV $1/2^+$ level, 2.028 MeV $5/2^+$ level, 2.426 MeV $3/2^+$ level and 4.742 MeV $9/2^+$ level. These levels after mixing in the BM calculation have a predominant part of their wave function from the $K=1/2^+(211)$ orbit. In the description of fig. 21 the exit channel is defined as all the possible ways the other coupled levels influence the level of interest.

The rotational model with bandmixing (BM) was selected as the better model to use since it is consistent with the rotational description of the coupled-channel wave functions and is a better fit to the ^{29}Si nucleus as seen in sect. 3. The phases of the model amplitudes obey equation 71 in Ch. IV otherwise different shapes can result.

Fig. 22 shows the results of coupling the exit (E) channel in a CCBA calculation. The curves were normalized to the total (T) solid line to agree with the forward angle data and shape. Differential cross section for each type of transition was calculated. The dot and long dashed lines have only the exit (E) transitions considered. The long dashes represent the incident (I) transition and the short dashed curves are simple direct (D) transitions

Figure 22. The $^{30}Si(d,t)^{29}Si$ angular distribution for ground state band of ^{29}Si coupled. The effects of the exit channel coupled are examined in the figure. The BM model amplitudes were used with the normalizations in rounded brackets need to be multiplied by 1.5. The four types of transition explained in fig. 21 are calculated with solid curve total transition, dot and long-dashed the exit transition, long-dashes the incident transition and short dashes the direct transition.

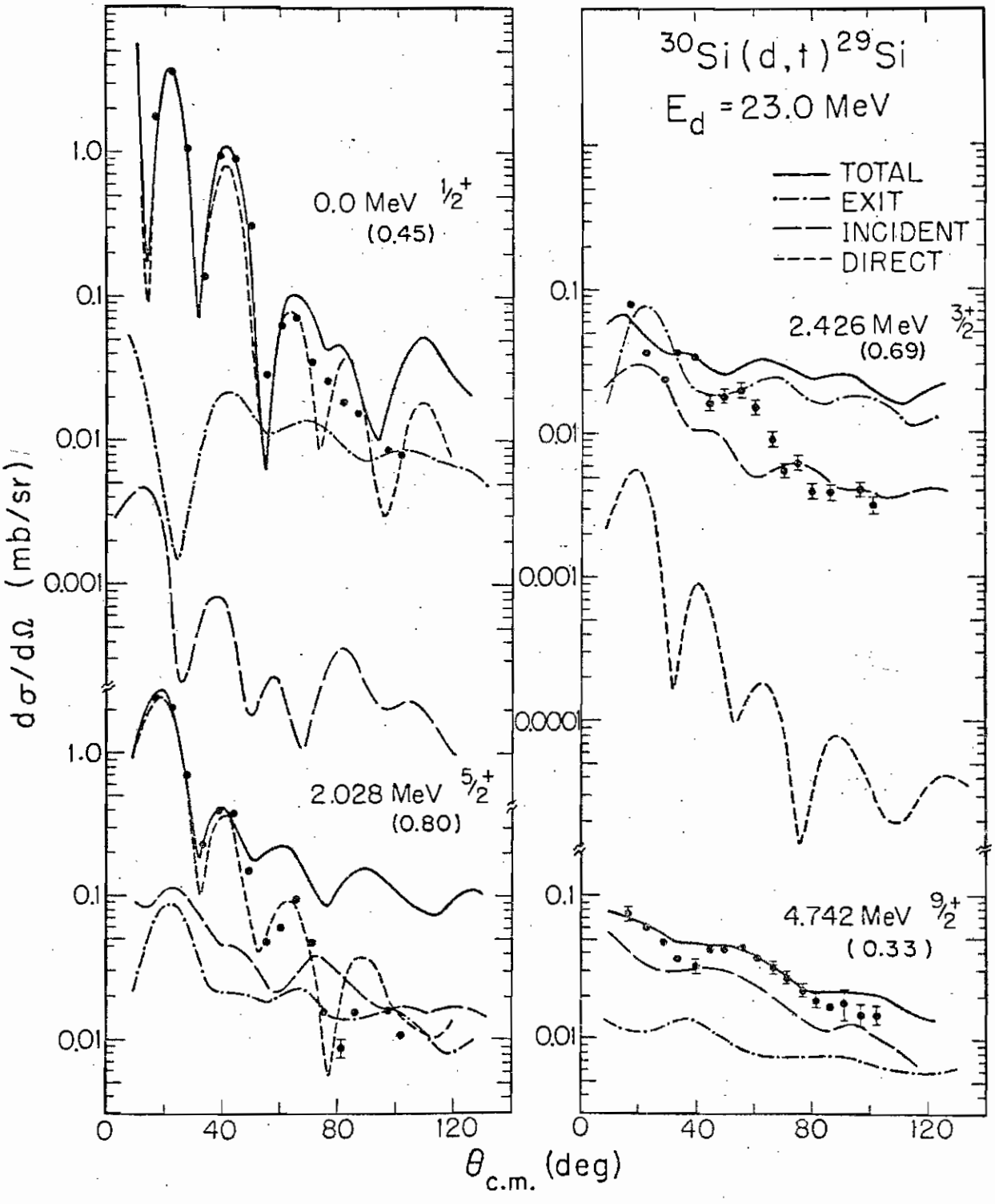
$^{30}Si(d,t)^{29}Si$
$E_d = 23.0$ MeV
TOTAL
EXIT
INCIDENT
DIRECT
0.0 MeV $1/2^+$
(0.45)
2.028 MeV $5/2^+$
(0.80)
2.426 MeV $3/2^+$
(0.69)
4.742 MeV $9/2^+$
(0.33)
$d\sigma/d\Omega$ (mb/sr)
$\theta_{c.m.}$ (deg)
1.0
0.1
0.01
0.001
0.0001
0
40
80
120

between coupled-channel optical model wave functions.

The first three levels were coupled first, as done in the ^{3}He inelastic scattering. The transition to the ground state is almost purely direct, but the inclusion of the exit transition improves the agreement with the data in the second peak and smooths the calculated T curve past 50° in the center of mass. Another predominantly direct level is the 2.028 MeV $5/2^{+}$ level as the direct (D) calculation agrees the best. The total calculation has too much indirect amplitudes as before in fig. 15. By changing the sign of all the exit transition amplitudes the I and E curves cancel out most of their influence. The 2.426 MeV $3/2^{+}$ level has a total calculation with again too much indirect amplitude. The I and E calculations each contribute a substantial portion of the predicted total calculation. An attempt was made to change the sign of the I or E transitions to find a better fit but with little success. The basic problem seems to be a lack of direct strength. From these curves it can be seen how the direct spectroscopic factor can have multistep amplitudes in it.

In calculating the 4.742 MeV $9/2^{+}$ level the ^{3}He inelastic scattering to this state was not measured, but an upper limit of $10\,\mu b/cm^{2}$ could be placed on the cross section. Sample coupled-channel calculations were done coupling the ground state, 2.028 MeV $5/2^{+}$ state and 4.742 MeV $9/2^{+}$ state to check that the calculated inelastic ^{3}He scattering was reasonable. The same parameters were used as before. The 2.426 MeV $3/2^{+}$ level was not coupled since it cannot directly couple to the 4.742 MeV $9/2^{+}$ level with only a quadrupole coupling. The CCBA calculations were done and the normalization dropped

by almost a factor of five to 0.50 from that on fig. 16. The other three states did not exhibit such a change in normalization. The simple optical model in this case is not a good approximation to the exit channel in comparison to having the exit channel coupled. For the other cases the coupling in the exit channel did not significantly alter the normalizations.

As done before an average can be computed of the normalizations used in fig 22 and the results are 0.84 ± 0.18. If the normalizations are taken from the previous section in fig. 15 and 16 the average is 1.32 ± 0.58 for these four levels. Coupling the exit channel does have a good effect with the average closer to unity with smaller deviation. These averages would lead to the conclusion that the model amplitudes are quite good but some reservations must be pointed out. The exit coupling is based on ^{3}He rather than triton scattering. Tritons are highly absorptive as deuterons and the effect of coupling might alter the change in the imaginary strength more drastically. The inability to include the rotational band starting with the 1.273 MeV $3/2^+$ level could change the results. It is highly mixed and the inelastic ^{3}He scattering from this level is of the same size as that measured from the 2.426 MeV $3/2^+$ level.

Chapter VI

CONCLUSIONS

The calculations of this present study done in order to understand the $^{30}Si(d,t)^{29}Si$ and $^{30}Si(d,\ ^{3}He)^{29}Al$ reactions have been enlightening. The rotational model with bandmixing (BM) has proved to be a simple method of understanding rotational nuclei. The results for the transfer reactions with only the incident channel coupled display good agreement with usually too much indirect amplitude for the indirect transfers to the $7/2^+$ or $9/2^+$ levels. The shell model results for the transfer reaction are not as good with a few levels having bad shapes and the normalizations are far from unity. A shell model calculation in this mass region is striving to create a collective nature by including many spherical configurations. In a CCBA calculation the various calculated amplitudes are tested. The use of shell model amplitudes has been criticized because the excited 2^+ state is described collectively and not as a shell model state. Once the transition is calculated it is a number to be tested and this is the way differences are found.

The calculations for the electromagnetic rates added more proof to how well the rotational model can describe these nuclei. The simplicity of the rotational model in describing a deformed state is a virtue and success. The main problem seems to be that the magnetic transitions are not calculated properly even though some of them agree with the experiment.

The inclusion of the exit channel could have complicated the results, but instead gave a boost to the rotational model. Even though the results were not

perfect a smaller deviation from average for the ground state band of ^{29}Si was measured. To calculate the exit channel properly the other rotational bands starting with the first excited state in ^{29}Si must be coupled. The coupling in the exit channel seems to be important for high spin states. This could be explained by the decay of a high spin state to a few levels which when coupled change the wave functions.

One of the more interesting features that needs more investigation is the extraction of the direct spectroscopic factor. From a combination of direct and indirect amplitudes a measured angular distribution can be fit. The number of indirect components could be restricted to the J^{π} of the direct transfer, but for example, a $J^{\pi} = 3/2^{+}$ state could be from a $K^{\pi} = 1/2^{+}$ orbit and have a large indirect s1/2 indirect amplitude with a small d3/2 indirect amplitude. Such a case yields different shapes. That model dependence is still needed for a CCBA calculation may be its greatest virtue.

APPENDICES

Appendix A

Silicon Target Fabrication

The fabrication of thick uniform enriched silicon targets from SiO_2 is difficult. From commercial grade silicon monoxide thick natural targets have been produced easily by vacuum evaporation. A closed boat with a small escape hole is used because the silicon monoxide pops as it is heated. Since the enriched isotope is obtained in the form of SiO_2 the problem is to convert SiO_2 to SiO. Mellor's Treatise on Inorganic Chemistry[65] indicates that this can be done by carbon reduction. The chemical reaction is $SiO_2 + C \xrightarrow{heat} SiO + CO$. This equation implies that for five parts of silica, one part of carbon is needed. The material must be crushed and mixed thoroughly in order that the reduction is complete.

A three cm seamless 10 mil wall 0.25" O.D. tempered tantalum tube was used. The ends were crimped closed and a hole was drilled in the middle with a no. 68 drill. Ordinary glass slides were cleaned and placed above the tube in an evaporator. One crystal of CsI was placed on the tube near the hole. It evaporated first since its melting temperature is lower than that needed to start the above chemical reaction. This layer is water soluble and allows the SiO target to be floated off the slide at a later time. The evaporation is usually started with a vacuum of about 10^{-5} mm of Hg. Voltage is applied to the tantalum tube until the CsI evaporates. Heating is continued for about seven minutes to reach 1450° C. The vacuum gauge should be watched carefully since the production of carbon monoxide, a gas, will cause

the pressure to increase dramatically. The reaction usually begins at about 1500° C and at that time the vacuum can drop to about 10^{-3} mm of Hg. A Leeds and Northrup optical pyrometer is used to measure these temperatures. Care must be taken at this stage because the material inside could be pushed out by the escaping gas. If the reaction is going too fast a sparking effect is seen with hot red crystals bombarding the slide. The pressure drops as the reaction completes itself. The slide meanwhile should first appear yellow and then an orange-brown as it thickens. The evaporation is continued for five to ten minutes at the same temperature in order to get as much enriched SiO out of the tube. Rapid cooling may produce extra strain on the film and the tube was cooled by ten ampere steps every five minutes until the tube became a dull red, then the current was reduced to zero. The temperatures quoted here are close to what was used but they are not exact, therefore in another evaporator higher or lower temperatures may be needed.

After the slides become cool enough the bell jar is opened. The lifting of the film off the slide is done in distilled water to minimize contaminants. In using so little release agent the floating procedure is very long and patience here is a virtue. If more CsI is used the floating of the film is faster but the crystalline structure subjects the film to cracking and produces pieces too small to mount on a target ring. Upon drying these foils will sometimes develop a curl and it was necessary to tack them down with a glue. In this case Dekophane diluted with alcohol was used to produce a thin non-stringy glue.

A guide for the amount of silicon dioxide needed for an approximate thickness was compiled in figure 23, for the case where the slide was at a distance

of six cm from the tantalum tube. For other distances a ratio of the squares will give a good estimate. The line can be considered a general guide of what can be expected for most evaporations. Sometimes the reduction is incomplete and in several cases was traced to the type of carbon used. The best carbon was separated isotope from Union Carbide, but graphite was also good. Activated charcoal should be avoided. It looks fine but will not combine readily to reduce the SiO_2. The reason is unknown. Fig. 24 shows a calculated curve of energy loss by an ^{241}Am alpha particle in silicon monoxide as a function of the thickness of the foil.

Figure 23. SiO Target Thickness. The dots represent the target thickness measured for amount of SiO_2 used. The solid line represents a general guide to what can be expected.

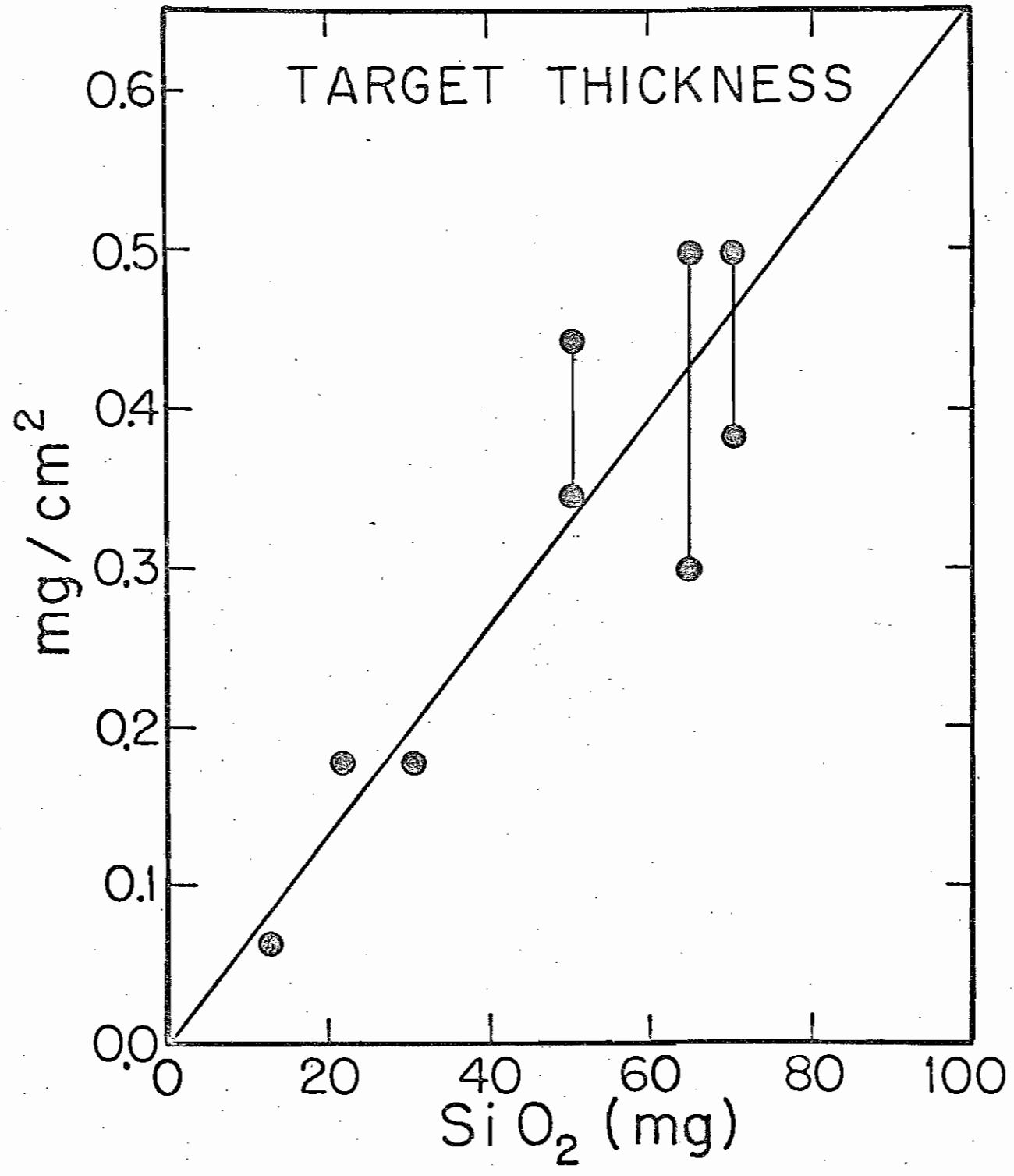
TARGET THICKNESS
0.6
0.5
0.4
0.3
0.2
0.1
0.0
mg / cm²
0
20
40
60
80
100
Si O₂ (mg)

Figure 24. Calculated energy loss curve for a 5.47 MeV α-particle through a SiO foil.

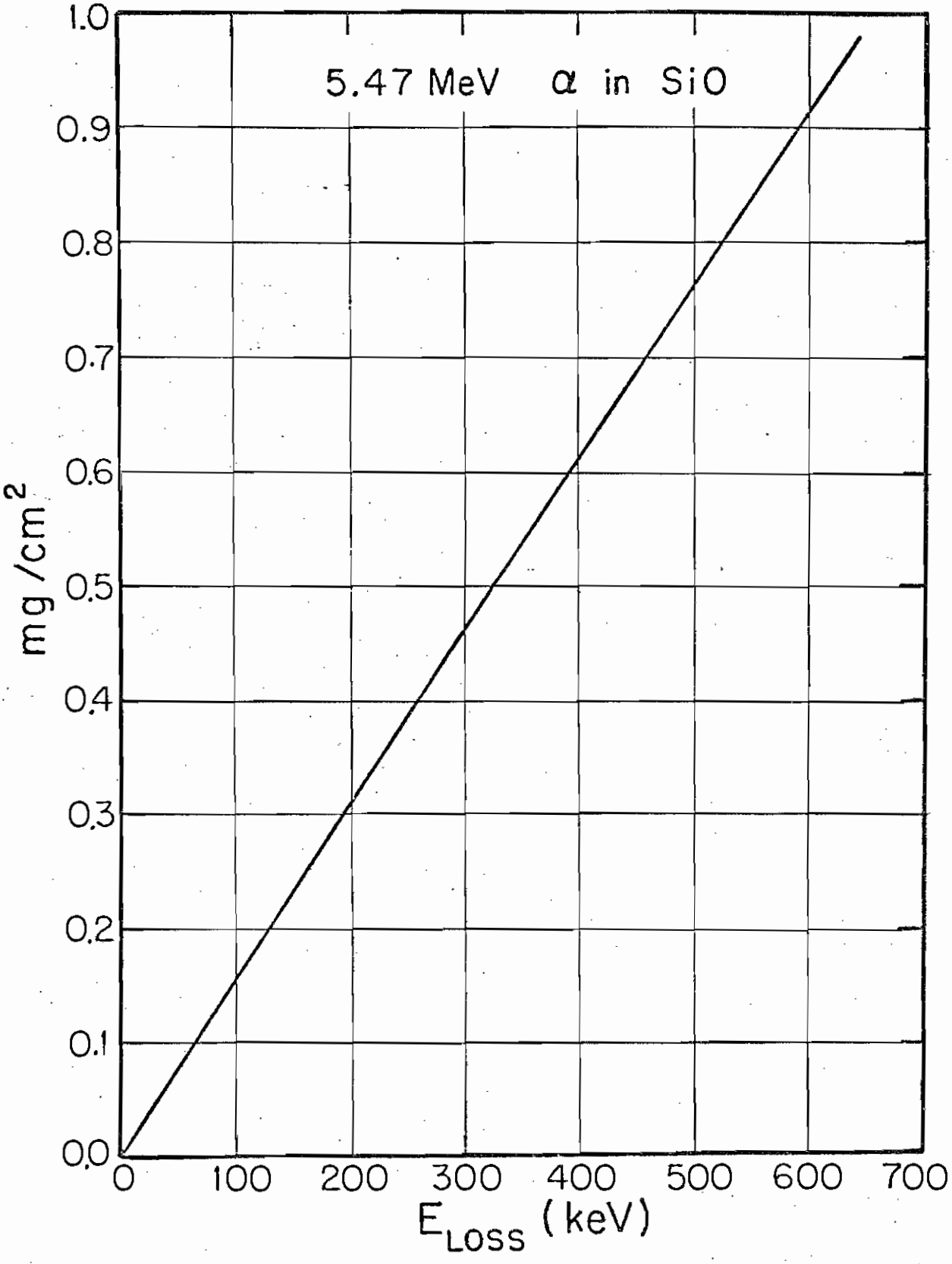
5.47 MeV α in SiO
mg/cm²
1.0
0.9
0.8
0.7
0.6
0.5
0.4
0.3
0.2
0.1
0.0
0
100
200
300
400
500
600
700
E_Loss (keV)

Appendix B

Single Particle Orbitals in a Deformed Woods-Saxon Well

The next order of approximation for the Nilsson rotational model would be instead of the somewhat unrealistic harmonic oscillator basis to use a potential form that might represent the average nuclear force. A potential form frequently used for spherical nuclei is the Woods-Saxon form-factor. The form factor $f(r, r_o, a_o)$ and potential V commonly used is given as

$$V = V_o f(r, r_o, a_o) + V_{so} \frac{1}{r} \frac{d}{dr} f(r, r_o, a_o) \vec{l} \cdot \vec{s}$$

$$+ (zZe^2/2R_c)[3-(r/R_c)^2] \text{ for } r \leq R_c \text{ and } (zZe^2/r) \text{ for } r \geq R_c$$

with

$$f(r, r_o, a_o) = (1 + \exp((r - r_o A^{1/3})/a_o))^{-1}$$

and

$r_o A^{1/3}$	=	nuclear size
a	=	diffuseness
z	=	charge of particle moving in well
Z	=	charge of nucleus A
$R_c A^{1/3}$	=	coulomb charge radius
r	=	position of particle in well
V_o	=	strength of well
V_{so}	=	strength of spin-orbit.

A simple method to deform this spherical well is to add to the radius parameter a quadrupole term given by

$$R = r_o A^{1/3} (1.0 + \beta_2 \; Y_{20} + \cdots).$$

The resultant form factor is stable in shape presenting an oblate or prolate density. In the Tamura code NEPTUNE[41] a Legendre expansion of the Woods-Saxon well is made to ease computation, for a nucleon bound in the well. It should be noted that only the $V_o \; f(r, r_o, a_o)$ is deformed in this code. With given strengths V_o and V_{so}, deformation β_2, and appropriate geometrical parameters the binding energy of a nucleon in a nuclear system can be evaluated for a specific value of K (as in the Nilsson model), where K is the projection of the total angular momentum on the body fixed axis.

The code NEPTUNE uses the Condon-Shortly phase convention[47] which specifies certain conditions on the coefficients in the following equation

$$\Psi_{jm} = \sum_m (\ell s m_\ell m_s | j m) \; R(r) \; Y_{\ell m_\ell} X_{s m_s} .$$

Where $R(r)$, $Y_{\ell m_\ell}$, and $X_{s m_s}$ are radial, angular and spin wave functions. This is the simplest convention to use for bound states.

This convention on the spherical harmonics provides a nice feature in that matrix elements of Hermitean operators are all real. The time reversal phase convention has the angular wave function multiplied by an i^ℓ. For Ψ_{jm} the decomposition is

$$\Psi_{jm} = \sum_m (\ell s \; m_\ell m_s | j m) \; R(r) \; i^\ell \; Y_{\ell m_\ell} X_{s m_s} .$$

This convention is used in scattering with a central force and in pairing of

two Fermions with a two-body force. For negative parity operators between parity states the matrix elements can be imaginary in this phase convention. The main virtue of this convention is that it takes care of time reverse invariance.

As an example of the problem, let us look at the particle occupation amplitudes[32] V_ν that are used in paring theory. The occupation probability V_ν of the time reversed state in first phase convention differs by $(-1)^{\ell_\nu}$. Occupation numbers in the second phase convention do not change sign.[32] This may not seem important, but when evaluating direct spectroscopic amplitude S_{jk} for a nucleon transfer the occupation probability enters linearly[44] as

$$S_{jk} \propto V_j \, (\Psi_f \mid \Psi_i).$$

The implications are even greater if many orbits are mixed as in a band-mixing calculation. It is imperative to know the phase convention of all the codes used in determining the angular distributions.

For this work Erskine's code BANDMIX[48] was employed which used a form of the second phase convention. While all the results could be off an overall factor, the relative phases were correct. The particle occupation numbers were calculated and used as positive numbers. One other note is that the predicted energy spectrum is not affected by either phase convention, just the phases of the spectroscopic amplitudes. In the Tamura code MARS[27] the coupled-channel incident and exit wave functions are calculated using time reversed wave functions[66,67]. Phase conventions should not be mixed to

calculate the proper results. Therefore the results from calculating deformed states with NEPTUNE need to be changed. A deformed orbital with quantum number K can be written as $|K\rangle$ and is decomposed into a spherical basis as

$$|K\rangle = \sum_j C_{jk} |j\ell K\rangle \quad .$$

The expansion coefficient C_{jk} can be modified to have the correct phase convention. The results from NEPTUNE are changed from the first to the second phase convention by multiplying the C_{jk} by i^{ℓ}. A property of $|K\rangle$ that is of interest to this work is that they are orthogonal to orbits with same K.

Figure 7 shows the orbits possible for the split 2s1/2, 1d5/2, 1d3/2 and 2p3/2, single particle states when a quadrupole term is introduced. The orbits are labeled by the Nilsson asymtotic quantum number (N, n_z, Λ), K^{π}, and orbit number. The energy scale records the binding energy as a positive number, starting with zero at the top. The potential used is of the form described for a Woods-Saxon well whose radius is expanded with a quadrupole term. The parameters are for the nucleus ^{29}Si and are

$$V_o = 54.2 \text{ MeV}$$

$$V_{so} = 7.5 \text{ MeV}$$

$$r_o = 1.25 \text{ fm}$$

$$a_o = 0.65 \text{ fm}$$

$$R_c = 1.25 \text{ fm}$$

In the tables that follow of the coefficients of expansion, the energy

E (MeV) is the binding energy of that $|K\rangle$ in the deformed potential. The decoupling parameter a for the $K=1/2$ orbits is defined as

$$a = \sum_j (-1)^{j-1/2}(j+1/2)\left|C_{j\,1/2}\right|^2 .$$

The tables to follow are for the specific system of mass 29, but after many calculations in the 2s-1d shell it was found that the coefficients do not drastically change. For nuclei with higher mass number more f-p orbitals become bound.

Table XI. Orbits bound in a Deformed Woods-Saxon potential. This table lists the energy eigenvalues with the normalized eigenvector components $C_{j\Omega}$ for each orbit. They are listed as a function of deformation β_2. The orbits are labeled by the Nilsson orbit no. and quantum numbers $(Nn_z\Lambda)$. Fig. 7 accompanies these tables displaying the tabulated results for the 2s-1d orbits and the bound 2p-1f orbits. For the negative parity orbits the components need to be multiplied by $i = \sqrt{-1}$. The decoupling parameter, a, is calculated for the K = 1/2 orbits. See appendix B and Ch. IV for more details.

β_2 =	-0.4	-0.3	-0.2	-0.1	0.0	0.1	0.2	0.3	0.4
K = 1/2$^+$ (000) Orbit No. 1									
E	38.01	38.14	38.25	38.31	38.33	38.32	38.25	38.14	38.00
a	1.008	1.005	1.003	1.001	1.000	1.001	1.002	1.007	1.010
L J									
0 1/2	0.991	0.995	0.998	0.999	1.000	0.999	0.997	0.994	0.988
2 3/2	-0.074	-0.057	-0.039	-0.020		0.020	0.041	0.061	0.082
4 5/2	0.111	0.086	0.059	0.030		-0.031	-0.063	-0.095	-0.127
K = 3/2$^-$ (101) Orbit No. 2									
E	28.36	28.02	27.62	27.18	26.69	26.14	25.55	24.92	24.25
L J									
1 3/2	0.993	0.996	0.998	0.999	1.000	0.999	0.997	0.993	0.987
3 5/2	-0.053	-0.040	-0.027	-0.014		0.015	0.032	0.049	0.067
3 7/2	0.106	0.083	0.058	0.030		-0.033	-0.068	-0.106	-0.145
K = 1/2$^-$ (110) Orbit No. 3									
E	26.67	26.47	26.31	26.33		27.32	28.06	28.81	29.51
a	-0.792	-1.006	-1.360	-1.796		-1.885	-1.741	-1.624	-1.544
L J									
1 1/2	0.638	0.579	0.465	0.264		0.197	0.297	0.361	0.397
1 3/2	0.760	0.809	0.882	0.964		-0.979	-0.951	-0.924	-0.904
3 5/2	0.052	0.035	0.016	0.002		-0.012	-0.028	-0.047	-0.064
3 7/2	0.113	0.095	0.072	0.040		0.041	0.079	0.113	0.143
K = 1/2$^-$ (101) Orbit No. 4									
E	20.72	21.80	22.75	23.42	23.67	23.48	23.07	22.54	21.94
a	-0.233	0.002	0.354	0.798	1.000	0.965	0.736	0.617	0.526
L J									
1 1/2	0.760	0.811	0.883	0.965	1.000	0.981	0.952	0.928	0.908
1 3/2	-0.630	-0.573	-0.464	-0.260		0.191	0.299	0.358	0.393
3 5/2	0.113	0.088	0.062	0.032		-0.031	-0.060	-0.088	-0.117
3 7/2	-0.117	-0.080	-0.043	-0.012		-0.010	-0.031	-0.058	-0.088
K = 5/2$^+$ (202) Orbit No. 5									
E	17.74	17.05	16.29	15.44	14.55	13.57	12.54	11.48	10.40
L J									
2 5/2	-0.992	-0.995	-0.998	-0.999	-1.000	-0.999	-0.998	-0.994	-0.989
4 7/2	0.037	0.029	0.020	0.010		-0.011	-0.023	-0.037	-0.050
4 9/2	-0.095	-0.074	-0.052	-0.027		0.030	0.063	0.099	0.137

Table XI. Continued

β_2 =	-0.4	-0.3	-0.2	-0.1	0.0	0.1	0.2	0.3	0.4
K = 3/2⁺ (211) Orbit No. 7									
E	14.73	14.51	14.39	14.40		14.76	15.04	15.33	15.62
L J									
2 3/2	-0.473	-0.367	-0.240	-0.106		-0.088	-0.149	-0.193	-0.225
2 5/2	-0.872	-0.924	-0.968	-0.994		0.995	0.985	0.972	0.959
4 7/2	-0.020	-0.006	0.003	0.005		0.011	0.025	0.040	0.056
4 9/2	-0.128	-0.106	-0.077	-0.041		-0.043	-0.085	-0.125	-0.163
K = 1/2⁺ (220) Orbit No. 6									
E	14.58	14.25	14.00	14.03		15.46	16.58	17.74	18.85
a	1.864	2.088	2.431	2.832		2.892	2.700	2.522	2.364
L J									
0 1/2	0.728	0.662	0.533	0.293		0.217	0.345	0.423	0.476
2 3/2	-0.138	-0.100	-0.047	-0.006		0.058	0.123	0.173	0.210
2 5/2	0.661	0.735	0.841	0.955		-0.973	-0.926	-0.881	-0.840
4 7/2	-0.025	-0.020	-0.009	-0.003		-0.005	-0.015	-0.025	-0.039
4 9/2	0.116	0.102	0.079	0.046		0.047	0.089	0.123	0.152
K = 1/2⁺ (211) Orbit No. 9									
E	9.58	10.13	10.62	10.97	11.09	11.11	11.43	11.85	12.25
a	0.857	0.926	0.951	0.946	1.000	0.682	0.046	-0.273	-0.540
L J									
0 1/2	0.493	0.602	0.756	0.923	1.000	0.902	0.701	0.553	0.459
2 3/2	-0.573	-0.519	-0.425	-0.265		0.371	0.626	0.724	0.761
2 5/2	-0.639	-0.598	-0.495	-0.279		0.219	0.337	0.399	0.435
4 7/2	-0.076	-0.052	-0.030	-0.009		-0.014	-0.046	-0.081	-0.114
4 9/2	-0.119	-0.087	-0.049	-0.014		-0.012	-0.037	-0.064	-0.091
K = 3/2⁺ (202) Orbit No. 8									
E	9.78	9.85	9.72	9.38	8.90	8.11	7.27	6.35	5.37
L J									
2 3/2	-0.875	-0.927	-0.970	-0.994	-1.000	-0.996	-0.987	-0.977	-0.965
2 5/2	0.467	0.362	0.236	0.110		-0.085	-0.147	-0.192	-0.222
4 7/2	-0.106	-0.084	-0.058	-0.030		0.030	0.060	0.091	0.122
4 9/2	0.077	0.047	0.022	0.005		0.005	0.017	0.036	0.059

Table XI. Continued

β_2 =	-0.4	-0.3	-0.2	-0.1	0.0	0.1	0.2	0.3	0.4
K = 1/2$^+$ (200) Orbit No. 11									
E	3.81	5.29	6.71	7.94		9.14	8.82	8.16	7.37
a	-0.698	-1.004	-1.385	-1.776		-1.572	-0.749	-0.238	0.042
L J									
0 1/2	0.499	0.458	0.387	0.255		0.376	0.627	0.723	0.759
2 3/2	0.787	0.838	0.900	0.963		-0.925	-0.766	-0.655	-0.590
2 5/2	-0.332	-0.274	-0.188	-0.081		0.027	0.125	0.201	0.248
4 7/2	0.127	0.101	0.073	0.039		0.037	0.064	0.084	0.104
4 9/2	-0.076	-0.047	-0.022	-0.005		-0.001	-0.015	-0.037	-0.064
K = 7/2$^-$ (303) Orbit No. 10									
E	6.53	5.61	4.61	3.55	2.37	1.25			
L J									
3 7/2	-0.996	-0.998	-0.999	-0.999	-1.000	-0.999			
5 9/2	0.027	0.021	0.015	0.008		-0.008			
5 11/2	-0.082	-0.064	-0.045	-0.023		0.025			
K = 5/2$^-$ (312) Orbit No. 12									
E	3.31	3.04	2.80	2.60		2.27	2.14	2.02	1.92
L J									
3 5/2	-0.277	-0.199	-0.123	-0.058		-0.048	-0.087	-0.118	-0.142
3 7/2	-0.953	-0.975	-0.990	-0.998		0.998	0.993	0.986	0.977
5 9/2	-0.003	0.007	0.008	0.006		0.009	0.019	0.031	0.044
5 11/2	-0.122	-0.098	-0.069	-0.036		-0.038	-0.076	-0.114	-0.151
K = 3/2$^-$ (321) Orbit No. 13									
E	3.70	3.16	2.64	2.24		3.03	3.73	4.42	5.05
L J									
1 3/2	0.865	0.839	0.775	0.530		0.217	0.300	0.348	0.384
3 5/2	-0.060	-0.042	-0.020	0.012		0.046	0.088	0.122	0.147
3 7/2	0.492	0.538	0.629	0.847		-0.974	-0.946	-0.921	-0.896
5 9/2	-0.016	-0.011	-0.007	-0.004		-0.007	-0.016	-0.027	-0.040
5 11/2	0.078	0.066	0.054	0.038		0.045	0.087	0.126	0.163

Table XI. Continued

β_2 =	-0.4	-0.3	-0.2	-0.1	0.0	0.1	0.2	0.3	0.4
K = 1/2⁻ (330) Orbit No. 14									
E	2.70	2.33	2.04	1.96		3.49	4.80	6.19	7.58
a	-1.610	-2.051	-2.662	-3.471		-3.758	-3.450	-3.316	-2.958
L J									
1 1/2	0.517	0.429	0.293	0.107		0.054	0.119	0.173	0.216
1 3/2	0.694	0.703	0.673	0.489		-0.340	-0.481	-0.554	-0.599
3 5/2	0.121	0.085	0.045	0.014		-0.024	-0.060	-0.098	-0.135
3 7/2	0.479	0.555	0.675	0.865		0.938	0.862	0.799	0.745
5 9/2	0.014	0.007	0.001	-0.001		0.003	0.008	0.016	0.028
5 11/2	0.084	0.076	0.063	0.042		-0.047	-0.085	-0.118	-0.145
K = 3/2⁻ (301) Orbit No. 16									
E		0.31	0.78	1.19	1.05	0.67	0.22		
L J									
1 3/2		0.557	0.636	0.849	1.000	0.977	0.958		
3 5/2		-0.197	-0.135	-0.067		0.044	0.081		
3 7/2		-0.800	-0.757	-0.524		0.208	0.275		
5 9/2		-0.008	-0.002	0.000		-0.001	-0.003		
5 11/2		-0.100	-0.066	-0.023		-0.010	-0.026		
K = 1/2⁻ (321) Orbit No. 17									
E				0.61		1.39	1.69	2.11	2.61
a				-2.054		-2.003	-1.793	-1.446	-1.089
L J									
1 1/2				0.372		0.263	0.433	0.534	0.582
1 3/2				0.793		-0.904	-0.757	-0.610	-0.480
3 5/2				0.013		-0.047	-0.135	-0.239	-0.330
3 7/2				-0.482		-0.333	-0.468	-0.528	-0.555
5 9/2				0.001		0.001	0.010	0.027	0.050
5 11/2				-0.024		0.017	0.048	0.081	0.113

Appendix C

Electric and Magnetic Transitions within the Rotational Model

A. Electric Transitions

Within the rotational model the general expression for the reduced transition is

$$B(\lambda : I_i K_i \; I_f K_f) = \left| C(I_i \lambda I_f : K_i,\ K_f - K_i,\ K_f) \left\langle K_f \right| T^B_{\lambda, K_f - K_i} \left| K_i \right\rangle \right.$$

$$\left. + (-1)^{I_i + \ell_i + 1/2} C(I_i \lambda I_f ; -K_i,\ K_i + K_f,\ K_f) \left\langle K_f \right| T^B_{\lambda, K_f + K_i} \left| -K_i \right\rangle \right|^2 \tag{C1}$$

as given by Nilsson[2]. The $C(ABC:abc)$ is a Clebsch-Gordon coefficient. Now for an odd-A nucleus the orbits are expanded as $|K\rangle = \sum_j C_{j\kappa} |N \ell j\kappa\rangle$. The states $|N \ell j\kappa\rangle$ are the spherical basis for the deformed orbit $|K\rangle$. The first case is an electric transition. The operator $T^B_{\lambda\mu}$ is $T^B_{\lambda\mu} = \sum_p e_p r_p^\lambda \; Y_{\lambda\mu}(\theta_p \phi_p)$ where the sum is over the nucleons taking part in the transition. In this discussion the odd nucleon is separated from the core so that the operator is just

$$T^B_{\lambda\mu} = e r^\lambda \, Y_{\lambda\mu}(\theta \phi). \tag{C2}$$

The matrix element is written generally as $\left\langle K_f \right| T^B_{\lambda\mu} \left| K_i \right\rangle$. The expansion of $|K\rangle$ is used and the matrix element is

$$= \sum_{j_f j_i} C^*_{j_f K_f} \; C_{j_i K_i} \; e \left\langle N_f \ell_f j_f K_f \right| r^\lambda \, Y_{\lambda\mu} \left| N_i \ell_i j_i K_i \right\rangle \tag{C3}$$

note: $\mu = K_f - K_i$, for the first element or $K_f + K_i$ for the second element. Now the reduction of the matrix element to one that is independent of K_f or K_i, is done with the Wigner Eckart Theorem, which is from DeShalit & Talmi[68] (D and T)

$$\langle JM | T_{\lambda\mu} | J'M' \rangle = (-1)^{J-M} \begin{pmatrix} J & \lambda & J' \\ -m & \mu & m' \end{pmatrix} \langle J \| T_\lambda \| J' \rangle$$

$$= \frac{(-1)^{2\lambda}}{2J+1} C(J'\lambda\, J \mid m'\mu m) \langle J \| T_\lambda \| J' \rangle \qquad (C4)$$

Therefore the matrix element is

$$\langle N_f \ell_f j_f K_f | \; r^\lambda Y_{\lambda\mu} | N_i \ell_i j_i K_i \rangle =$$

$$\frac{(-1)^{2\lambda}}{2j_f+1} C(j_i \lambda j_f ; K_i \mu K_f) \langle N_f \ell_f j_f \| r^\lambda Y_\lambda | N_i \ell_i j_i \rangle \qquad (C5)$$

The next step in the reduction is that the operator $r^\lambda Y_\lambda$ does not operate on the spin co-ordinates of the odd nucleon, only on its orbital angular momentum. Therefore the matrix element is reduced again to a dependence on ℓ. Note that $\vec{j} = \vec{\ell} + \vec{1/2}$ and with the decoupling equation (15.26 in D and T) the element is decomposed as

$$(j_1 j_2 J \| T^\lambda(1) \| j_1' j_2' j') = (-1)^{j_1 + j_2 + J' + \lambda} \sqrt{(2J+1)(2J'+1)}$$

$$\times \begin{Bmatrix} j_1 & j_1' & \lambda \\ J' & J & j_2 \end{Bmatrix} (j_1 \| T^\lambda(1) \| j_1') \delta_{j_2 j_2'} \qquad (C6)$$

Now the association $\vec{j}_2 = \vec{j}_2' = \vec{1/2}$, $\vec{j}_1 = \vec{\ell}_f$, $\vec{j}_1' = \vec{\ell}_i$, $\vec{J} = \vec{j}_f$, and $\vec{J}' = \vec{j}_i$ is made. The Wigner 6-j symbol can be rewritten as

$$\left\{ \begin{matrix} \ell_f \ell_i & \lambda \\ j_i \; j_f & 1/2 \end{matrix} \right\} = (-1)^{\ell_f + \ell_i + j_i + j_f} W(\ell_i j_i \ell_f j_f ; 1/2 \; \lambda) \tag{C7}$$

through its symmetry properties and definition p. 517 in D and T. The reduced matrix element of $r^\lambda Y_\lambda$ is then

$$\langle N_f \ell_f j_f \| r^\lambda Y_\lambda \| N_i \ell_i j_i \rangle = (-1)^{\ell_f + 1/2 + j_i + \lambda} (-1)^{\ell_f + \ell_i + j_i + j_f + j_f - j_f}$$

$$\sqrt{(2j_f + 1)(2j_i + 1)} \; W(\ell_i j_i \ell_f j_f : 1/2 \lambda) \langle \ell_f \| r^\lambda Y_\lambda \| \ell_i \rangle$$

$$= (-1)^{\ell_i - j_f + 1/2 + \lambda} \sqrt{(2j_f + 1)(2j_i + 1)} \; W(\ell_i j_i \ell_f j_f ; 1/2 \lambda) \langle \ell_f \| r^\lambda Y_\lambda \| \ell_i \rangle \tag{C8}$$

At this point the radial dependence is factored as a number with

$$\langle \ell_f \| r^\lambda Y_\lambda \| \ell_i \rangle = (\ell_f \| r^\lambda \| \ell_i) \langle \ell_f \| Y_\lambda \| \ell_i \rangle \, . \tag{C9}$$

Equation 17.14 of D and T is

$$\langle \ell_f \| Y_\lambda \| \ell_i \rangle = (-1)^{\ell_f} \sqrt{\frac{(2\lambda + 1)(2\ell_f + 1)(2\ell_i + 1)}{4\pi}} \begin{pmatrix} \ell_f & \lambda & \ell_i \\ 0 & 0 & 0 \end{pmatrix} \tag{C10}$$

$$= (-1)^{\ell_f} \sqrt{\frac{(2\lambda + 1)(2\ell_f + 1)(2\ell_i + 1)}{4\pi}} \begin{pmatrix} \lambda & \ell_i & \ell_f \\ 0 & 0 & 0 \end{pmatrix}$$

$$= (-1)^{\ell_f} \sqrt{\frac{(2\lambda + 1)(2\ell_f + 1)(2\ell_i + 1)}{4\pi}} \frac{(-1)^{\lambda - \ell_i}}{2\ell_f + 1} C(\lambda \ell_i \ell_f ; 000)$$

$$= (-1)^{\ell_f} \sqrt{\frac{(2\lambda + 1)(2\ell_i + 1)}{4\pi}} (-1)^{\lambda - \ell_i + \lambda + \ell_i - \ell_f} C(\ell_i \lambda \ell_f ; 000)$$

$$= \sqrt{\frac{(2\lambda + 1)(2\ell_i + 1)}{4\pi}} C(\ell_i \lambda \ell_f ; 000) \tag{C11}$$

where λ is an integer.

Now terms are collected with

$$\left\langle N_f \ell_f j_f K_f \left| r^\lambda Y_\lambda \right| N_i \ell_i j_i K_i \right\rangle = \frac{1}{\sqrt{2j_f+1}} C(j_i \lambda j_f; K_i \mu K_f)(\ell_f \| r^\lambda \| \ell_i)$$

$$(-1)^\lambda (-1)^{\ell_i - j_f + 1/2} \sqrt{(2j_f+1)(2j_i+1)}\, W(\ell_i j_i \ell_f j_f, 1/2\lambda)$$

$$\times \sqrt{\frac{(2\lambda+1)(2\ell_i+1)}{4\pi}}\, C(\ell_i \lambda \ell_f; 000)$$

$$= (-1)^\lambda (-1)^{\ell_i - j_f + 1/2} \sqrt{\frac{(2j_i+1)(2\ell_i+1)(2\lambda+1)}{4\pi}}\, C(j_i \lambda j_f; K_i \mu K_f)$$

$$\times C(\ell_i \lambda \ell_f; 000)\, W(\ell_i j_i \ell_f j_f; 1/2\, \lambda)\, (\ell_f | r^\lambda | \ell_i). \qquad (C12)$$

Note the phase factor $(-1)^{2j_f - 1}$ is always even so that

$$(-1)^{\ell_i - j_f + 1/2 + 2j_f - 1} = (-1)^{\ell_i + j_f - 1/2} \qquad (C13)$$

The $C(j_i \lambda j_f; K_i \mu K_f)$ is factored as

$$\left\langle N_f \ell_f j_f K_f \left| r^\lambda Y_{\lambda\mu} \right| N_i \ell_i j_i K_i \right\rangle =$$

$$C(j_i \lambda j_f; K_i \mu K_f)\, M(\lambda, j_i, \ell_i, j_f, \ell_f)$$

where

$$M(\lambda, j_i \ell_i, j_f \ell_f) = (-1)^\lambda (-1)^{\ell_i + j_f - 1/2} \sqrt{\frac{(2j_i+1)(2\ell_i+1)(2\lambda+1)}{4\pi}}$$

$$C(\ell_i \lambda \ell_f; 000)\, W(\ell_i j_i \ell_f j_f; 1/2\lambda)\, (\ell_f | r^\lambda | \ell_i) \qquad (C14)$$

with this

$$B(\lambda:\ I_i K_i\ \ I_f K_f) = \Big| C(I_i \lambda I_f : K_i, K_f - K_i, K_f) \sum_{j_f j_i} eC^{*}_{j_f K_f} C_{j_i K_i}$$

$$C(j_i \lambda j_f : K_i, K_f - K_i, K_f)\, M(\lambda, j_i \ell_i, j_f, \ell_f) + (-1)^{I_i + \ell_i + 1/2}$$

$$C(I_i \lambda I_f ; -K_i, K_f + K_i, K_f) \sum_{j_f j_i} eC^{*}_{j_f K_f} C_{j_i - K_i}\ C(j_i \lambda j_f ; -K_i, K_f + K_i, K_f)$$

$$M(\lambda, j_i \ell_i, j_f \ell_f) \Big|^2 \qquad \text{(C15)}$$

now the relation $C_{j-K} = (-1)^{\ell + j - 1/2} C_{jK}$ is used and only one sum is needed as

$$B(\lambda : I_i K_i\ \ I_f K_f) = \Big| e \sum_{j_f j_i} C^{*}_{j_f K_f} C_{j_i K_i} M(\lambda, j_i \ell_i, j_f \ell_f)$$

$$C(I_i \lambda I_f ; K_i, K_f - K_i, K_f)\, C(j_i \lambda j_f ; K_i, K_f - K_i, K_f) +$$

$$(-1)^{I_i + \ell_i + 1/2 + \ell_i + j_i - 1/2} C(I_i \lambda I_f ; -K_i, K_f + K_i, K_f)$$

$$C(j_i \lambda j_f ; -K_i, K_f + K_i, K_f) \Big|^2 \qquad \text{(C16)}$$

$$= \Big| e(-1)^{\lambda} \sum_{j_f j_i} (-1)^{\ell_i + j_f - 1/2} C^{*}_{j_f K_f} C_{j_i K_i}$$

$$\sqrt{\frac{(2j_i + 1)(2\ell_i + 1)(2\lambda + 1)}{4\pi}}\ C(\ell_i \lambda \ell_f : 000)\ W(\ell_i j_i \ell_f j_f ; 1/2\, \lambda)$$

$$(\ell_f | r^{\lambda} | \ell_i)\ C(I_i \lambda I_f ; K_i, K_f - K_i K_f)\, C(j_i \lambda j_f : K_i, K_f - K_i, K_f)$$

$$+ (-1)^{I_i + j_i} C(I_i \lambda I_f ; -K_i, K_f + K_i, K_f)\, C(j_i \lambda j_f ; -K_i, K_f + K_i, K_f) \Big|^2 \qquad \text{(C17)}$$

This expression is not the same in Davidson's book[38] (p. 113) the phase is different and a $(2j_i + 1)$ is used instead of a $(2j_f + 1)$.

The next step is to see what the operator for the core will yield. The operator is written as

$$T^{Core}_{\lambda\mu} = \frac{3/4}{\pi} Z_c e R_o^2 \qquad (C18)$$

which is added to the particle contribution coherently therefore interferences can occur. The operator $\alpha^*_{\lambda\mu}$ is a phonon operator connecting states only within an unmixed orbit that a quadrupole interaction couples such that

$$\langle K1 | \alpha^*_{\lambda\mu} | K'0 \rangle = \delta_{KK'} \langle 1 | \alpha^*_{\lambda\mu} | 0 \rangle \ . \qquad (C19)$$

The operator $\alpha^*_{\lambda\mu}$ on a deformed rotational state $|K\rangle$ has the expectation value simply of β_2 the deformation strength.

From the general expression for a reduced electromagnetic transition between states it is obvious that $|K\rangle$ need not be expanded into a spherical basis. Due to the delta function on K_i and K_f, the term to evaluate will be the first which is

$$C(I_i \lambda I_f ; K_i, 0, K_f) \delta(K_i, K_f) \langle K_f | \frac{3/4}{\pi} Z_c e R_o^2 | K_i \rangle =$$

$$C(I_i \lambda I_f ; K_i, 0, K_i) \frac{3/4}{\pi} Z_c e R_o^2 \beta_2 \langle K_i | K_i \rangle \qquad (C20)$$

This is a simple expression to evaluate and is needed to explain the strong intra-band transitions that are observed in deformed nuclei.

Now these matrix elements are recombined to give a complete description for the general expression of a reduced transition with the electric operator

$$T^{el}_{\lambda\mu} = e_p r_p^{\lambda} Y_{\lambda\mu}(\theta_p, \phi_p) + \frac{3/4}{\pi} Z_c e R_o^2 \alpha^*_{\lambda\mu} \qquad (C21)$$

where $Z_c e$ is the charge of the core that the nucleon observes, R_o is the radius of that core as $R_o = 1.2\text{fm}\ A^{1/3}$, e_p is the effective charge of the nucleon and has to be treated as

$$e_p = (Z_p + \frac{Z_c}{A}) e , \qquad (C22)$$

and Z_p is the charge of the nucleon. This type of effective charge has been used extensively and seems to produce the desired observed effects in mirror nuclei.

With this $B(\lambda: I_i K_i - I_f K_f)$ is explicitly for an electric transition

$$\Big| C(I_i \lambda I_f; K_i, 0, K_f)\ \delta(K_i, K_f)\ \frac{3/4}{\pi}\ Z_c e R_o^2 \beta_2 +$$

$$e_p (-1)^{\lambda} \sum_{j_f j_i} (-1)^{\ell_i + j_f - 1/2} C^*_{j_f K_f} C_{j_i K_i} \sqrt{\frac{(2j_i + 1)(2\ell_i + 1)(2\lambda + 1)}{4\pi}}$$

$$C(\ell_i \lambda \ell_f; 000)\ W(\ell_i j_i \ell_f j_f; 1/2\lambda)\ (\ell_f | r^{\lambda} | \ell_i) \Big\{ C(I_i \lambda I_f; K_i, K_f - K_i, K_f)$$

$$C(j_i \lambda j_f; K_i, K_f - K_i, K_f)\ (-1)^{I_i + j_i}\ C(I_i \lambda I_f; -K_i, K_f + K_i, K_f)$$

$$C(j_i \lambda j_f; -K_i, K_f + K_i, K_f) \Big\} \Big|^2 . \qquad (C23)$$

The next step is to calculate this properly with a state that is a mixture of unmixed orbits or deformed states. In this framework K is no longer a good quantum number for the complete wave function but is still good for each of its components such that

$$\psi^{I}_{\text{mixed}} = \psi^{I}_{M} = \sum_{\substack{n \\ \text{orbits}}} a_n \, | IK_n \rangle \ . \qquad \text{(C24)}$$

Often such a stats is labeled with a K which is the largest component of the wave function, but this is only a guide to try to preserve some sense of bond structure in interpreting level systematics.

The reduced transition probability for such a state can actually be written down simply by putting a label on K of which orbit n it came from, thus

$$B(\lambda; I_i^{\text{mixed}} \rightarrow I_f^{\text{mixed}}) = \Bigg| \sum_{n_f n_i} a^{*}_{n_f} a_{n_i} \left(Z_c \, eR_o^2 \, \beta_2 \right.$$

$$C(I_i \lambda I_f; K_{in_i}, 0, K_{fn_f}) \times \delta(K_{in_i}, K_{fn_f}) +$$

$$e_p (-1)^{\lambda} \sum_{j_f j_i} (-1)^{\ell_i + j_f - 1/2} C^{*}_{j_f K_f}(n_f) C_{j_i K_i}(n_i)$$

$$\sqrt{\frac{(2j_i+1)(2\ell_i+1)(2\lambda+1)}{4\pi}} (\ell_f n_f | r^{\lambda} | \ell_i n_i) \Big\{ C(I_i \lambda I_f; K_{in_f},$$

$$K_{fn_f} - K_{in_i}, K_{fn_f}) C(j_i \lambda j_f; K_{in_i}, K_{in_f} - K_{in_i}, K_{fn_f}) +$$

$$(-1)^{I_i + j_i} C(I_i \lambda I_f; -K_{in_f}, K_{fn_f} + K_{in_i}, K_{fn_f})$$

$$\left. \times C(j_i \lambda j_f; -K_{in_i}, K_{fn_f} - K_{in_i}, K_{fn_f}) \Big\} \right) \Bigg|^2 \qquad \text{(C25)}$$

B. Magnetic Transitions

The magnetic operator is

$$M_m(\lambda,\mu) = \frac{e\hbar}{2m_p c} \sum_p \left(g_s \vec{s} + g_\ell \frac{2}{\lambda+1} \vec{\ell} \right) \cdot \nabla_p [r_p^\lambda Y_{\lambda\mu}]$$

$$+ \frac{e\hbar}{m_p c} \frac{1}{2\lambda+1} g_R \int \vec{R}(\vec{r}) \cdot \nabla [r^\lambda Y_{\lambda\mu}] \, d\tau \, . \qquad (C26)$$

The only case considered here will be for the magnetic dipole with $\lambda = 1$. Nilsson[2] has shown that the second term in eq. C26 can be added to the first by the replacement,

$$g_s \longrightarrow g_s - g_R$$

and

$$g_\ell \longrightarrow g_\ell - g_R \, .$$

The operator becomes

$$M_m(1,\mu) = \frac{e\hbar}{2m_p c} \left((g_s - g_R) \vec{s} + (g_\ell - g_R) \vec{\ell} \right) \cdot \nabla_p [r_p^\lambda Y_{1\mu}] \qquad (C27)$$

where the sum has been dropped since only one particle outside the core is calculated. This replacement is a first order approximation to the integral of the angular momentum density $\vec{R}(\vec{r})$ which is hard to determine. The sum of $\vec{\ell}$ and $\vec{s}$ is $\vec{j}$ and again the magnetic operator is rewritten as

$$M_m(1,\mu) = \mu_0 \left[(g_s - g_\ell) \vec{s} + (g_\ell - g_R) \vec{j} \right] \cdot \nabla [r Y_{1\mu}]$$

where

$$\mu_0 = \frac{e\hbar}{2m_p c} \, . \qquad (C28)$$

Within the rotational model the general expression for the reduced transition probability (eq. C1) is used and the states are expanded. This leaves the matrix element as

$$\left\langle K_f \left| M_m(1,\mu) \right| K_i \right\rangle = \sum_{j_f j_i} C^{*}_{j_f K_f} \; C_{j_i K_i} \left\langle N_f \ell_f j_f K_f \left| M_m(1,\mu) \right| N_i \ell_i j_i K_i \right\rangle$$

$$= \sum_{j_f j_i} C^{*}_{j_f K_f} \; C_{j_i K_i} \; \frac{C(j_i \, j_f ; K_i \mu K_f)}{\sqrt{2 j_f + 1}} \left\langle N_f \ell_f j_f \left\| M_m(1,\mu) \right\| N_i \ell_i j_i \right\rangle \tag{C29}$$

where the Wigner-Eckart theorem eq. C5 was used. Another matrix element now needs to be reduced, but first separate ths $\vec{j}$ and $\vec{s}$ parts of the operator as

$$\left\langle N_f \ell_f j_f \left\| M_m(1,\mu) \right\| N_i \ell_i j_i \right\rangle = \mu_o (g - g_R) \left\langle N_f \ell_f j_f \left\| \nabla (r Y_{1\mu}) \cdot \vec{J} \right\| N_i \ell_i j_i \right\rangle$$

$$+ \mu_o (g - g) \left\langle N_f \ell_f j_f \left\| \nabla (r Y_{1\mu}) \cdot \vec{s} \right\| N_i \ell_i j_i \right\rangle \tag{C30}$$

Now using eq. 17.21 from DeShalit and Talmi (D and T)

$$= \mu_o (g_\ell - g_R) \sqrt{3} \left\langle N_f \ell_f j_f \left| r^o \cdot (\vec{Y}_o \times \vec{j})^{(1)} \right| N_i \ell_i j_i \right\rangle$$
$$+ \mu_o (g_s - g_\ell) \sqrt{3} \left\langle N_f \ell_f j_f \left| r^o \cdot (\vec{Y}_o \times \vec{s})^{(1)} \right| N_i \ell_i j_i \right\rangle \tag{C31}$$

Note that $\mu = 0$ always once this is done and therefore $K_i = K_f$ eliminating the second term of eq. C1. Eq. C31 is split into two parts the $\vec{j}$ term and the $\vec{s}$ term. With eqs. 17.22 and 17.23 of D and T the $\vec{j}$ and $\vec{s}$ terms of eq. C31 become

$$= \sqrt{3} \mu_0 (g - g_R) (\ell_f j_f \| Y_0 \| \ell_i j_i) (\ell_f j_f \| \vec{j} \| \ell_i j_i) \; 3 \; (-1)^{j_f + j_i + 1} \begin{Bmatrix} j_f & 1 & j_i \\ 1 & j_i & 0 \end{Bmatrix}$$

$$+\sqrt{3}\,\mu_0\,(g_s - g_R)\,(\ell_i \| Y_0 \| \ell_i)(s_f \| s \| s_i)\sqrt{(2j_f+1)(3)(2j_i+1)}\begin{Bmatrix} \ell_f & 1/2 & j_f \\ \ell_i & 1/2 & j_i \\ 0 & 1 & 1 \end{Bmatrix} \quad (C32)$$

with $\langle r^0 \rangle = 1$. Now it is noted that

$$(\ell_f\, j_f \| Y_0 \| \ell_i\, j_i) = (-1)^{\ell_f + j_i + 1/2}\,(\ell_f \| Y_0 \| \ell_i)\sqrt{(2j_i+1)(2j_f+1)}\begin{Bmatrix} \ell_f & j_f & 1/2 \\ j_i & \ell_i & 0 \end{Bmatrix} \quad (C33)$$

with

$$(\ell_f \| Y_0 \| \ell_i) = \sqrt{\frac{1}{4\pi}}\,(-1)^{\ell_f}\sqrt{(2\ell_f+1)(2\ell_i+1)}\begin{pmatrix} \ell_f & 0 & \ell_i \\ 0 & 0 & 0 \end{pmatrix}$$

$$= \sqrt{\frac{1}{4\pi}}\,(-1)^{\ell_i + \ell_f}\sqrt{2\ell_f + 1}\;\delta(\ell_i, \ell_f). \quad (C34)$$

Then with

$$\begin{Bmatrix} \ell_f & j_f & 1/2 \\ j_i & \ell_i & 0 \end{Bmatrix} = \begin{Bmatrix} \ell_f & \ell_i & 0 \\ j_i & j_f & 1/2 \end{Bmatrix} = \frac{(-1)^{\ell_f + j_i + 1/2}}{\sqrt{(2\ell_f+1)(2j_i+1)}}\,\delta(\ell_f, \ell_i)\,\delta(j_i, j_f) \quad (C35)$$

eq. C33 becomes

$$(\ell_f j_f \| Y_0 \| \ell_i j_i) = \frac{(-1)^{\ell_i + \ell_f}}{\sqrt{4\pi}}\;\sqrt{2j_f + 1}\;\delta(\ell_f, \ell_i)\,\delta(j_i j_f). \quad (C36)$$

In the first term

$$(\ell_f j_f \| \vec{j} \| \ell_i\, j_i) = \sqrt{(2j_i + 1)(j_i)(j_i + 1)}\;\;\delta(j_i\, j_f) \quad (C37)$$

and in the second term

$$(s_f \| \vec{s} \| s_i) = \sqrt{3/2}\;\delta(s_f, s_i). \quad (C38)$$

In the first term the 6-j symbol can be simplified as

$$\begin{Bmatrix} j_f & 1 & j_i \\ 1 & j_i & 0 \end{Bmatrix} = \begin{Bmatrix} j_f & j_i & 0 \\ 1 & 1 & j_i \end{Bmatrix} = \frac{(-1)^{j_f + j_i + 1}}{\sqrt{3(2j_f+1)}} \quad \delta(j_f, j_i). \tag{C38}$$

In the second term the 9-j symbol can be simplified to a 6-j symbol by noting from eq. C34 that $\ell_i = \ell_f$ then

$$\begin{Bmatrix} \ell_i & 1/2 & j_f \\ \ell_i & 1/2 & j_i \\ 0 & 1 & 1 \end{Bmatrix} = \begin{Bmatrix} \ell_i & \ell_i & 0 \\ 1/2 & 1/2 & 1 \\ j_f & j_i & 1 \end{Bmatrix} = \begin{Bmatrix} 1/2 & 1/2 & 1 \\ j_f & j_i & 1 \\ \ell_i & \ell_i & 0 \end{Bmatrix}$$

$$= \frac{(-1)^{3/2 + j_f + \ell_i}}{3(2\ell_i + 1)} \begin{Bmatrix} 1/2 & 1/2 & 1 \\ j_i & j_f & \ell_i \end{Bmatrix}$$

$$= \frac{(-1)^{j_i + \ell_i - 1}}{3(2\ell_i + 1)} \; W(j_i\, j_f\, 1/2\; 1/2;\, 1\, \ell_i) \tag{C39}$$

where eq. C7 used to change 6-j symbol to Racah coefficient. All the immediate simplification are done therefore eq. C32 becomes

$$= \mu_o (g_s - g_\ell)\sqrt{\frac{3}{4\pi}}\,(-1)^{\ell_i + \ell_f}\sqrt{j_i(2j_i+1)(j_i+1)}\;\delta(\ell_f, \ell_i)\,\delta(j_i\, j_f)$$

$$+ \mu_o (g_\ell - g_R)\sqrt{\frac{3}{4\pi}}\,(-1)^{j_i + \ell_f - 1/2}\sqrt{\frac{1}{2}}\sqrt{(2j_f+1)(2j_i+1)}\; W(j_i j_f\, 1/2\; 1/2;\, 1\, \ell_i) \tag{C40}$$

Therefore the matrix element becomes

$$\langle N_f\, \ell_f\, j_i \| M_m^{(l,\mu)} \| N_i\, \ell_i\, j_i \rangle = \mu_o \sqrt{\frac{3}{4\pi}}\,\delta(\ell_i \ell_f)\sqrt{2j_i + 1}$$

$$\times \left\{ (g_\ell - g_R)(-1)^{\ell_i + \ell_f}\sqrt{j_i(j_i+1)}\;\delta(j_i, j_f) + (g_s - g_\ell)(-1)^{j_i + \ell_f - 1/2} \right.$$

$$x\sqrt{\frac{3}{2}(2j_f+1)}\quad W(j_i\, j_f\, 1/2\;\; 1/2\;;|\ell_i)\quad .$$

It is noted that $\mu = 0$ implying $\Delta K = 0$ or $\sum K = 0$ always from eq. C31. The reduced transition probability for one unmixed orbit to another for a M1 multipole is

$$B(M1) = \frac{3}{4\pi}\mu_0^2 \Big| \sum_{j_i\, j_f} C^{*}_{j_f K_f}\; C_{j_i K_i}\; \delta(\ell_i \ell_f)\sqrt{\frac{2j_i+1}{2j_f+1}}$$

$$\Big[x\quad (g_\ell - g_R)(-1)^{\ell_i+\ell_f}\sqrt{j_i(j_i+1)}\;\delta(j_i\, j_f) + (g_s - g_\ell)(-1)^{j_i+\ell_f-1/2}$$

$$x\sqrt{\frac{3}{2}(2j_f+1)}\;\; W(j_i\, j_f\, 1/2\;\; 1/2\;;|\ell_i)\Big]\, x\, \Big[C(I_i|\, I_f;\, K_i,\; K_f - K_i, K_f)$$

$$x\; C(j_i|\, j_f;\, K_i,\; K_f - K_i, K_f)\;\delta(K_f - K_i, 0) + (-1)^{I_i + j_i}$$

$$x\;\; C(I_i|\, I_f;\, -K_i,\; K_f + K_i,\; K_f)\;\; C(j_i|\, j_f;\, -K_i,\; K_f + K_i,\; K_f)\,\delta(K_f + K_i, 0)\Big]\Big|^2$$

(C41)

When using mixed wave functions, the procedure is the same as for the electric case. The delta functions on the K of the orbits allows only the proper combinations to contribute.

LIST OF REFERENCES

LIST OF REFERENCES

1. A. Bohr and B. R. Mottleson, Det. Kgl. Danske Videnskab. Selskab Mat. -Fys. Medd. 27 (1953) no. 16.

2. S. G. Nilsson, Det. Kgl. Danske Videnskab. Selskab, Mat. -Fys. Medd. 29 (1955) no. 16.

3. A. D. W. Jones, J. A. Becker, and R. E. McDonald, Phys. Rev. C3 no. 2 (Feb, 1971) 724

4. A. D. W. Jones, J. A. Becker, and R. E. McDonald, Phys. Rev. 187 no. 4 (Nov., 1969) 1388

5. R. C. Bearse, D. H. Youngblood, and J. L. Yntema, Phys. Rev. 167 no. 4 (March, 1968) 1043

6. R. G. Hirko, R. A. Lindgren, A. J. Howard, J. G. Pronko, M. W. Sachs, and D. A. Bromley, Part. Nucl. 1 (1971) 372

7. D. C. Kean, K. W. Carter, C. J. Pilusi, and R. H. Spear, Nucl. Phys. A132 (1969) 241

8. D. R. Goosman, C. N. Davids, and D. E. Alburger, Phys, Rev. C 8 no. 4 (Oct., 1973) 1331

9. J. R. Williams, D. R. Tilley, C. R. Gould, R. O. Nelson, and N. R. Roberson (to be published)

10. F. A. Beck, T. Byrski, G. Costa, and P. Engelstein, Nucl. Phys. A128 (1974) 213

11. D. Dehnard and J. L. Yntema, Phys. Rev. 163 no. 4 (Nov., 1970) 1198

12. F. Pellegrini, F. Gentilin, P. Guazzoni, S. Micheletti, and M. Pignanelli, Phys. Rev. C 2 no. 4 (Oct., 1970) 1440

13. A. H. Pilt, R. H. Spear, R. V. Elliott, and J. A. Kuehner, Can. Journal of Physics 49 (1971) 1263

14. A. El-Naiem and R. Reif, Nucl. Phys. A189 (1972) 305

15. T. T. Bardin, J. A. Becker, T. R. Fisher, and A. D. W. Jones, Phys. Rev. C 4 no. 5 (Nov., 1971) 1625

16. M. C. Mermaz, C. A. Whitten Jr., J. W. Champlin, A. J. Howard, and D. A. Bromley, Phys. Rev. C 4 No. 5 (Nov., 1971) 1778

17. I. Ragnarsson and S. G. Nilsson, Nucl. Phys. A158 (1970) 155

18. G. R. Bishop, Nucl. Phys. 14 (1959/1960) 376

19. B. Castel, K. W. C. Stewart, and M. Harvey, Can. Journal of Physics 48 (1970) 1490

20. M. J. A. DeVoigt, P. W. M. Glaudemans, J. DeBoer, and B. H. Wildenthal, Nucl. Phys. A186 (1972) 365

21. B. H. Wildenthal and J. B. McGrory, Phys. Rev. C 7 no. 2 (Feb., 1973) 714

22. H. C. Lee and R. Y. Cusson, Annals of Physics 72 no. 2 (Aug., 1972) 353

23. R. O. Nelson, unpublished Ph.D. thesis, Duke University (1972)

24. R. J. Ascuitto and N. K. Glendenning, Phys. Rev. C 2 no. 2 (Aug., 1970) 415

25. R. J. Ascuitto and N. K. Glendenning, Phys. Rev. 181 no. 4 (May, 1969) 1396

26. S. K. Penny and G. R. Satchler, Nucl. Phys. 53 (1964) 145

27. T. Tamura, code MARS private communication (1971)

28. W. S. McEver, unpublished Ph.D. Thesis, Univ. of North Carolina at Chapel Hill, (1970)

29. J. M. Joyce, W. S. McEver, R. O. Nelson, R. V. Poore, and N. R. Roberson, Bull. Am. Phys. Soc. 15 (1970) 598

30. D. D. Armstrong, J. G. Berry, E. R. Flynn, W. S. Hall, P. W. Keaton Jr., and M. P. Kellog, Nucl. Intr. and Meth. 70 (1969) 69

31. R. O. Nelson, private communication (1973)

32. D. J. Rowe, Nuclear Collective Motion, Models and Theory, (Methuen and Co., London, 1970)

33. T. Tamura, Rev. of Mod. Phys. 37 no. 4 (Oct., 1965) 679

34. T. Tamura, Annual Reviews of Nuclear Science (1969) 99

35. T. Tamura, D. R. Bes, R. A. Broglia, and S. Landowne, Phys. Rev. Letters 25 no. 21 (Nov., 1970) 1507

36. N. K. Glendenning and R. S. Mackintosh, Nucl. Phys. A168 (1971) 575

37. T. Y. Wu and T. Ohmura, Quantum Theory of Scattering (Prentice-Hall, New York, 1962)

38. J. P. Davidson, Collective Models of the Nucleus (Academic Press, New York, 1968)

39. V. H. Webb, unpublished Ph.D. thesis, Duke University (1968)

40. E. Rost, Phys. Rev. 154 (1966) 994

41. T. Tamura code NEPTUNE, from A. W. Obst, private communication (1973)

42. J. P. Davidson, Rev. of Mod. Phys. 37 no. 1 (Jan., 1965) 105

43. S. T. Belyaev, Det. Kgl. Danske Videnskab, Selskab, Mat.-Fys. Medd. 31 (1959) no.11

44. S. Yoshida, Phys. Rev. 123 (1961) 2122

45. B. L. Cohen, Concepts of Nuclear Force (McGraw-Hill Co., New York, 1971)

46. G. R. Satchler, Annals of Physics 3 (1958) 275

47. T. Udagawa, private communication (1973)

48. J. R. Erskine, code BANDMIX, unpublished

49. S. J. Skorka, J. Hertel and T. W. Retz-Schmidt, Nucl. Data A2 (1966) 347

50. P. M. Endt and C. Van der Leun, Nucl. Phys. A214 (1973) 1

51. S. Maripuu, private communication (1973)

52. G. W. Schweiner and H. Rebel, des Zyklotron-Laboratoriums, unpublished (1970)

53. T. Tamura, ORNL report no. 4152 (1967)

54. D. Kolb, private communication (1973)

55. R. Y. Cusson, private communication (1973)

56. M. Berg, A. Hofmann, K. Thomas, H. Rebel, and G. W. Schweimer, Phys. Lett. 42B no. 2 (1972) 211

57. W. J. Thompson, private communication (1971)

58. F. G. Perey, code J1B3, unpublished

59. R. J. Eastgate, W. J. Thompson, and R. A. Hardekopf, code OPTICS

60. R. W. Zurmuhle and C. M. Fou, Nucl. Phys. A129 (1969) 502

61. E. J. Ludwig, T. C. Clegg, and R. L. Walter, Nucl. Phys. A211 (1973) 559

62. I. E. McCarthy, Introduction to Nuclear Theory (John Wiley and Sons, Inc., New York, 1968) 395

63. R. J. Ascuitto and N. K. Glendenning, Phys. Rev. C 2, no. 4 (Oct., 1970) 1260

64. P. J. Ellis and A. Dudek, Part. Nucl. 5 no. 5 (Jan., 1973) 1

65. J. W. Mellor, A Comprehensive Treatise on Inorganic and Theoretical Chemistry Vol. VI, (Longmans, Green and Co., New York, 1947)

66. A. N. Obst, private communication (1973)

67. T. Udagawa, private communication (1973)

68. A. de-Shalit and I. Talmi, Nuclear Shell Theory (Academic Press, New York, 1963)

BIOGRAPHY

Robert A. Hilko

Personal: Born January 5, 1945, Hamtramck, Michigan

Single

Education: B. A. in Physics
Oakland University (1967)

Positions: Research Assistant, Duke University 1967
Teaching Assistant, Duke University 1967-1968
Research Assistant, Duke University 1968-1974

Membership: American Physical Society

Publications:

1. Study of ^{18}O through $^{14}C + \alpha$ Reaction, G. L. Morgan, D. R. Tilley, G. E. Mitchell, R. A. Hilko and N. R. Roberson, Nuclear Physics A148 (1970) 480.

2. States in ^{18}O Excited by the $^{14}C(^{7}Li, t)$ Reaction, G. L. Morgan, D. R. Tilley, G. E. Mitchell, R. A. Hilko and N. R. Roberson, Physics Letters Vol. 32B no. 5 (Aug. 1970) 353.

Abstracts:

1. The $^{14}C(\alpha, \alpha)^{14}C$ Reaction from 4 to 8 MeV, G. L. Morgan, G. E. Mitchell, D. R. Tilley, R. A. Hilko and N. R. Roberson, Bull. Am. Phys. Soc. 14 no. 4 (1969) 508.

2. Elastic Scattering of Alpha Particles on ^{14}C from 3.5 to 16.5 MeV, G. L. Morgan, G. E. Mitchell, D. R. Tilley, R. A. Hilko and N. R. Roberson, Bull. Am. Phys. Soc. 14 no. 12 (1969) 1221.

3. Measurement of Spectroscopic Factors in the

$^{24}Mg(d,t)^{23}Mg$ and $^{24}Mg(d,{}^{3}He)^{23}Na$ Reaction, R. O. Nelson, N. R. Roberson and R. A. Hilko, Bull. Am. Phys. Soc. 16 no. 4 (1971) 621.

4. Mass Identification of Charged Particles by Time of Flight, R. A. Hilko, R. O. Nelson, T. G. Dzubay, and N. R. Roberson, Bul. Am. Phys. Soc. 17 no. 4 (1972) 461.

5. Inelastic Effects in the study of ^{23}Na and ^{23}Mg, R. O. Nelson, N. R. Roberson and R. A. Hilko, Bull. Am. Phys. Soc. 17 no. 4 (1972) 532.

6. Inelastic Effects in the Study of ^{29}Al and ^{29}Si, R. A. Hilko, N. R. Roberson, R. O. Nelson and C. R. Gould, Bull. Am. Phys. Soc. 18 no. 4 (1973) 604.